

**Satellite AVHRR Observations of the Intensification of the Shelf
Break Current during an Upwelling Event off Vancouver Island**

by

Gordon Clifford Staples

B.Sc., University of British Columbia, 1985

A THESIS SUBMITTED IN PARTIAL FULFILMENT OF
THE REQUIREMENTS FOR THE DEGREE OF
MASTER OF SCIENCE

in

THE FACULTY OF GRADUATE STUDIES

Department of Oceanography

We accept this thesis as conforming
to the required standard

THE UNIVERSITY OF BRITISH COLUMBIA

April, 1993

© Gordon Clifford Staples, 1993

In presenting this thesis in partial fulfilment of the requirements for an advanced degree at The University of British Columbia, I agree that the Library shall make it freely available for reference and study. I further agree that permission for extensive copying of this thesis for scholarly purposes may be granted by the Head of my Department or by his or her representatives. It is understood that copying or publication of this thesis for financial gain shall not be allowed without my written permission.



Department of Oceanography

The University of British Columbia
2075 Wesbrook Place
Vancouver, Canada
V6T 1W5

Date: April 28, 1993

Abstract

AVHRR satellite imagery during July 1984 was used to investigate the spatial and temporal variability of the shelf break current during an upwelling event off Vancouver Island. The onset of the order 10-day upwelling event initially appears as a plume of cold water at the tip of Brooks Peninsula. As the winds increase in strength, the plume of cold water migrates equatorward and takes on a jet-like structure that remains centred just seaward along the shelf break. As the winds dramatically weaken near the end of the upwelling event, there is intense warming of the surface waters along the shelf, but a band of cold water persists along the shelf break. Horizontal scales calculated from thermal fronts in the AVHRR imagery show that along the shelf break, the cross-shore scale is about 20 km, which is consistent with the internal Rossby radius. Approximately 70 km offshore, another thermal front is present, and this front is thought to represent the offshore extent of the shelf break current.

AVHRR measurements of the SST were correlated with *in situ* temperature measurements, and a r^2 value of around 0.85 was obtained for the upper 3 m of the water column. The temporal variations in the AVHRR SST structure were related to the temporal variations of the coastal wind field, and to temporal variations in temperature measurements obtained from coastal lightstations and subsurface moorings. The long-shore velocity was estimated from the AVHRR imagery, and speeds that were calculated to be from 10 and 80 cm/s, were in agreement with long-shore speeds of 20 to 30 cm/s measured by a subsurface current mooring, and long-shore speeds between 10 and 100 cm/s calculated using a time-independent barotropic model.

Results indicate that wind and topography play important roles in the upwelling response, and under the right conditions, AVHRR observations of SST are representative of dynamical processes within the ocean. The band of cold water along the shelf break is thought to be due to the combined processes of advection and shelf break upwelling.

Table of Contents

Abstract.....	ii
List of Tables.....	v
List of Figures.....	vi
Acknowledgments.....	vii
Chapter 1	
Introduction.....	1
1.1 Coastal Processes	1
1.2 The Study Area	8
1.3 Thesis Objectives and Overview.....	10
Chapter 2	
The Oceanographic Setting	12
2.1 Vancouver Island Oceanography.....	12
2.1.1 Bathymetry	12
2.1.2 Winds and Currents	15
2.2 Vancouver Island Upwelling	20
2.2.1 Overview	20
2.2.2 Observations	21
2.3 Summary	24
Chapter 3	
Data Collection and Processing	25
3.1 Advanced Very High Resolution Radiometer	25
3.1.1 Background	25
3.1.2 Sea Surface Temperature	27
3.2 AVHRR Data Processing	29
3.2.1 The Data Set.....	29
3.2.2 Navigation, Calibration, and SST Retrieval.....	32
3.3 Image Analysis.....	37
3.3.1 Feature Identification.....	37
3.3.2 Sea Surface Temperature Transects	41
3.4 Hydrographic, Wind, and Bakun Index Data	42
3.5 Summary	44
Chapter 4	
Upwelling Theory	46
4.1 Basic Two-layer Theory	46
4.1.1 Coastal Transport.....	46
4.1.2 Two-layer Flow.....	48
4.2 Shelf Break Effects.....	55
4.2.1 Observations	55
4.2.2 Upwelling and Jets.....	56
Chapter 5	
Upwelling Event: Observations and Analysis	60
5.1 Wind and Coastal Temperatures	60
5.2 AVHRR Observations	67
5.2.1 Stage 1: July 13-15.....	68

	5.2.2 Stage 2: July 16-17.....	74
	5.2.3 Stage 3: July 18-20.....	78
	5.2.4 Stage 4: July 23-24.....	82
	5.2.5 Long-shore Sea Surface Temperature.....	86
	5.3 Hydrographic Structure.....	88
	5.4 Dynamical Interpretation.....	92
	5.4.1 Cross-shore Fronts.....	92
	5.4.2 Shelf-break Jet Formation.....	96
	5.4.3 Surface Velocity and Shelf Break Upwelling.....	99
Chapter 6		
Summary and Conclusions.....		106
	6.1 Summary of Results.....	106
	6.2 Conclusion.....	109
Chapter 7		
Bibliography.....		113

List of Tables

Table 3.1. Characteristics of the AVHRR/2 sensor.....	27
Table 3.2. Satellite number and orbit, and time of data reception.....	31
Table 5.1. AVHRR image features.....	68
Table 5.2. Long-shore velocity estimates (cm/s) using AVHRR measurements, barotropic model, and measurements from the E2 current mooring.....	102

List of Figures

Figure 1.0. Continental margin schematic diagram	2
Figure 1.2. AVHRR imagery showing a) eddy and b) cold-water plume	6
Figure 1.3. The Vancouver Island study area and location of place names.....	9
Figure 2.1. Bathymetry along Vancouver Island	13
Figure 2.2. Bathymetric cross-sections at selected locations along Vancouver Island.....	14
Figure 2.3. Monthly mean Bakun "winds"	17
Figure 2.4. Circulation along Vancouver Island a) winter regime, b) summer regime.	18
Figure 2.5. Currents off Estevan Point	19
Figure 3.1. Emission spectra at different temperatures.....	28
Figure 3.2. Typical near-surface temperature profiles.....	34
Figure 3.3. Comparison of AVHRR SST (n6.26388) and in situ SST (Line E).....	36
Figure 3.4. Typical histogram of a thermal IR image	38
Figure 3.5. Map showing the location of SST transects, CTD stations, current meter locations, coastal wind stations, and lighthouse stations.....	43
Figure 4.1. Schematic diagram of the coastal upwelling regime showing the Ekman layers and the geostrophic interior	48
Figure 4.2. The notation used to describe the constant depth, two-layer model.....	49
Figure 4.3. The upwelling solution for an eastern boundary	54
Figure 4.4. The shelf region with variable topography on both sides of the shelf break..	57
Figure 5.1. a) Cape Scott wind b) Cape Scott Long-shore wind.....	61
Figure 5.2. Kains Island lightstation temperature	62
Figure 5.3. a) Estevan Point wind b) Estevan Point long-shore wind.....	64
Figure 5.4. Amphitrite Point lightstation temperature	65
Figure 5.5. Bakun Upwelling Index a) (51 N,131 W) b) (48 N,125 W).....	66
Figure 5.6. Stage 1 AVHRR imagery	69
Figure 5.6. Stage 1 AVHRR imagery (continued).....	71
Figure 5.7. Stage 1 cross-shore SST transects (day 195 to 197)	73
Figure 5.8. Stage 2 AVHRR imagery.	75
Figure 5.9. Stage 2 cross-shore SST transects (day 198-199)	77
Figure 5.10. Stage 3 AVHRR imagery	79
Figure 5.11. Stage 3 cross-shore SST transects (day 200 -202).....	81
Figure 5.12. Stage 4 AVHRR imagery	83
Figure 5.13. Stage 4 cross-shore SST transects	85
Figure 5.14. Long-shore SST transects south of Brooks Peninsula	87
Figure 5.15. Estevan Point a) temperature contour, b) sigma-t contour	89
Figure 5.16. Estevan Point velocity and sub-surface temperature	91
Figure 5.17. Cross-shore SST fronts	93
Figure 5.18. Estevan Point long-shore flow	98
Figure 5.19. Sobel edge maps. a) July 16, b) July 17	101

Acknowledgments

Much like clothing or the mask of emotion, ocean waves are the manifestation of the sea in motion, and yet beneath the waves, there are waves, currents, and an abundance of life that remain hidden to all but those who chip away at the surface facade, and dig deeply into its complexities in pursuit of understanding. During my thesis research, I have dug into the ocean in an attempt to understand some of these complexities, and in the course of understanding, I have developed a clarity of reason that applies to all endeavors. In this renaissance of clarity, I have been inspired by the dedication to understanding and the enthusiastic spirit of the people within the Department of Oceanography and beyond.

I would like to thank my thesis supervisor, William Hsieh, who encouraged me to focus my efforts when I was dealing with the vast amounts of AVHRR satellite data at the onset of my thesis and gently nudged in the right direction when I veered off course. I would also like to thank Rick Thomson at the Institute of Ocean Sciences who was a source of inspiration, and to echo Pijush Kundu's comment of a "cheerful voice over the telephone that was a constant reassurance that professional science can make some people happy". In addition, I would like to acknowledge my diving buddy, Peter Baker, who agreed with me that oceanographers should get wet on occasion, the "oceanography Dads", Guido Marinone and Roger Pieters, who were receptive to conversations on midnight feedings, David Jones, for creative solutions to the acquisition of Vancouver real estate, Ian "Mr. Upwelling" Jardine and Scott Tinis for their stimulating discussion, and Denis Laplante, who cheerfully provided an effective fly-swatter for every computer bug that flew his way.

Loving acknowledgment goes to my wife, Heather, who patiently endured the many evenings and weekends that I spent working on my thesis, and managed to always put the important issues in perspective, and to my children, Mark, Courtney, and Richard, who can sometimes teach adults to view the world in a different way. I would also like to thank my parents, who showed me the difference between brooms and books, and were tolerant of my curiosity, in spite of their warning that under no circumstances was I to do a valve-job on the car.

Said the Polar Bear to the Snow Mouse, "I am speaking of great things to come".

CHAPTER 1

INTRODUCTION

1.1 Coastal Processes

During the Pleistocene Epoch, between 15,000 and 7,000 years ago, the sea level was depressed by some 130 m from its present level (Siebold and Berger, 1982). Large areas of the continental shelves were dry due to the sea level drop, and rivers entered the ocean along the shelf and cut back into the shelf forming the present troughs and canyons that are ubiquitous along most continental shelves. As the continental glaciers began to retreat during the warming period that followed the Pleistocene, the glacier melt waters returned to the ocean and the sea level began to rise to its present day level. The now submerged continental shelves cover about 5% of the earth's surface and are the most productive fisheries areas in the world. Ryther (1969) describes the open sea, which comprises 90% of the ocean, as a biological desert that produces a fraction of the world's fish catch. Ryther continues by saying that the balance of the world's fish catch are caught in upwelling regions and coastal waters that cover the continental shelves. In addition to the biological productivity associated with the shelf regions, continental shelves have a large effect on the physical oceanography of coastal waters. The shelf area which is cut by troughs and canyons, impinged upon by coastal capes, and fed by rivers, can trap internal waves, enhance coastal currents, and in addition to coastal upwelling, the shelf break region can act as a secondary source of upwelling.

Figure 1.1 shows the general characteristics of the Vancouver Island continental margin. Extending from the coastline to the shelf break, the continental shelf averages

about 40 km wide, but has a maximum width of 65 km seaward of the Juan de Fuca Strait and is within 8 km of the coastline off Brooks Peninsula. The shelf break is characterized by a relatively rapid change in water depth as the continental margin changes into the area called the continental slope.

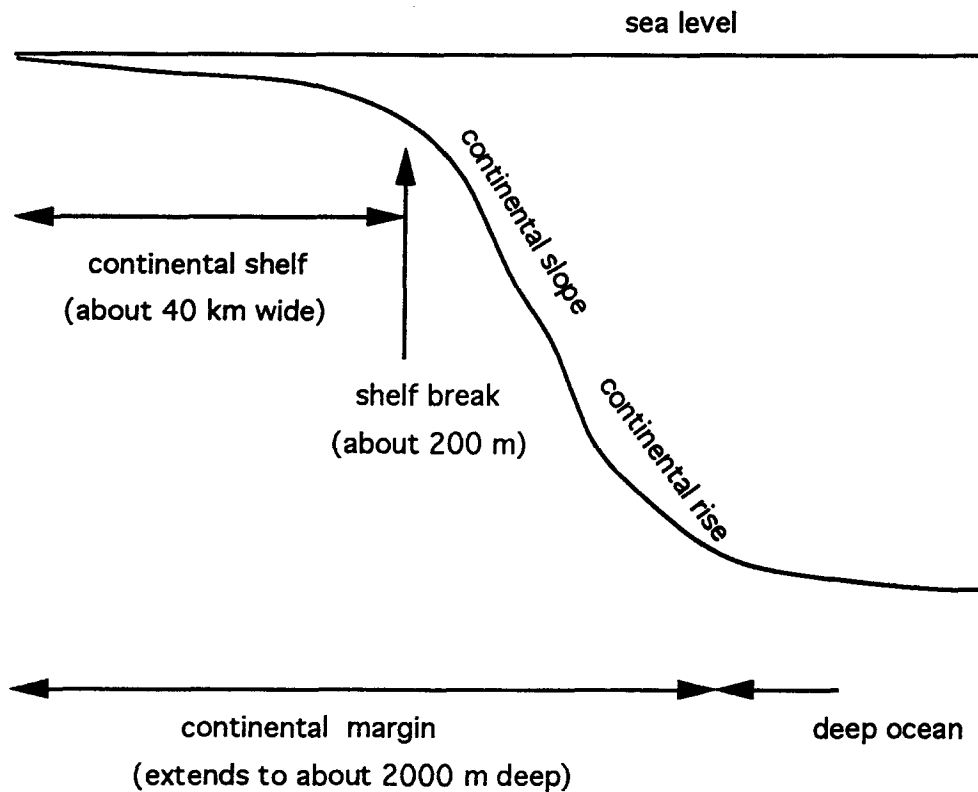


Figure 1. Continental margin schematic diagram (not to scale).

Beyond the continental slope, the topography gradually changes to the continental rise and eventually levels out and forms the floor of the deep ocean; the deep ocean floor is essentially featureless except for the occurrence of steep gradient sea mounts that can rise to within 30 m of the ocean surface. Most of the dynamical coastal processes occur within

100 km of the coastline, roughly an area that is shoreward of the continental slope; off Vancouver Island, the shelf break, shelf slope area is usually defined along the 200 m isobath. For the purpose of this thesis, the shelf break and shelf slope region will be referred to as the shelf break, and regions beyond the shelf slope will be referred to as the offshore or deep ocean; the continental shelf area will be referred to as the shelf or coastal region.

Bowden (1981) said that the shelf break zone divided the deep ocean regime from the shelf waters. He continued by saying that for circulation on the shelf, the deep ocean is involved as a driving force with the interaction taking place across the shelf break, and from the deep ocean side, the shelf break region can appear as a boundary layer of the deep-sea circulation. In contrast to the flow patterns of western boundary currents where a sharp gradient between the coastal and oceanic waters is a pronounced feature, the eastern boundary currents that flow offshore from Vancouver Island do not display strong frontal zones between coastal and oceanic waters. However, during an upwelling event, cold subsurface water is upwelled along the coast and in some cases at the shelf break, and strong thermal gradients can form between the upwelled water and the warmer surface water.

The thermal gradients that form during an upwelling event can be readily sampled by conventional means such as using a CTD probe, but the spatial and temporal aspects of the sea surface temperature (SST) gradients can also be sampled by using the Advanced Very High Resolution Radiometer (AVHRR) instrument that is on the NOAA series of polar orbiting satellites. The CTD data provides measurements in the water column, but unless there are many research ships sampling at a given time, a CTD survey will likely cover the study area only once during an order 10-day upwelling event.

In comparison, a satellite can sample the entire study area many times a day depending on the particular orbit and the number of satellites that are within reception range of the ground station. The trade-off with the increased spatial and temporal coverage is that the AVHRR instrument only measures the so-called skin temperature of the ocean surface; according to Robinson (1985), the actual thickness of the skin layer varies with the wavelengths of the emitted radiation, and between 3 and 14 μm (the infrared range), it is less than 0.1 mm thick. However, the skin measurement is usually reasonably representative of the upper few meters of the water column, the so-called bulk sea surface temperature, but the agreement does however depend on such factors as the depth of the upper mixed layer, the amount of incident solar radiation, and the moisture content of the atmosphere above the sea (Stewart, 1985).

During times of strong winds from the northwest, satellite imagery often reveals the complex SST structure off Vancouver Island (some bias is introduced since clear satellite imagery is related to high pressure and northwesterly winds). The appearance of filaments, plumes, mesoscale meanders, and eddies are common features. The July 25, 1985 NOAA 9 infrared satellite image shown in Figure 1.2a is an example of an eddy that was situated southwest of Brooks Peninsula. The 60 km diameter eddy (E) was visible in the satellite imagery until July 29th. and was then lost due to cloud cover. AVHRR imagery often shows eddies in the vicinity of Brooks Peninsula, and the geographic location of the eddies is perhaps related to the local bathymetry. Eddies off Vancouver Island have been investigated by Thomson and Gower (1985), and Thomson (1984) and they suggest that eddy formation is due to baroclinic instabilities of a poleward flowing coastal jet and the instabilities may have been triggered by variations in the topography. Eddy formation and mesoscale meanders related to instabilities and topography effects were also investigated by Ikeda et al. (1984), and Ikeda et al. (1984a).

Figure 1.2b shows an example of plume formation off Vancouver Island. The NOAA 9 satellite image taken on August 2, 1988 shows cold water that extends to approximately 50 km offshore from northern Vancouver Island to Estevan Point; near Estevan Point, the cold water abruptly stops and an offshore plume (P) extends nearly 100 km in the offshore direction. South of Estevan Point, some clouds are visible, but the SST is considerable warmer than further north. The abrupt change in the SST and the formation of the offshore plume is perhaps related to the longshore gradient of the wind: strong winds at the northern end of Vancouver Island coupled with weak, or decreasing winds to the south (R. E. Thomson, pers. comm.).

The use of satellite imagery to study mesoscale processes is a tempting tool, but just as an eddy appears, or a cold water plume begins to migrate offshore, the SST structure is hidden by clouds. Since the AVHRR instrument is a passive receiver which is in contrast to an active instrument such as synthetic aperture radar, thin clouds can attenuate the radiation from the sea surface and cause an apparent reduction in the SST, and thick clouds can result in the satellite measuring the cloud-top temperature. Depending on the frequency of the observed dynamical process, a few days of clouds may be tolerated, but extended periods of thick cloud cover can result in a SST structure that is under sampled. Clouds can therefore cause problems, and one of the initial requirements of an AVHRR data set is that there are enough cloud-free images that adequately span a process such as upwelling.

Cloud-free AVHRR satellite imagery between July 13 to July 24, 1984 was obtained from the UBC Satellite Oceanography and Meteorological Lab (SOMeL) archive. The July sequence comprised thirteen late afternoon and early evening satellite passes, and two early morning passes. Due to the frequent occurrence of clouds along the west coast, it is usually difficult to obtain a reasonable long time series of cloud-free AVHRR images.

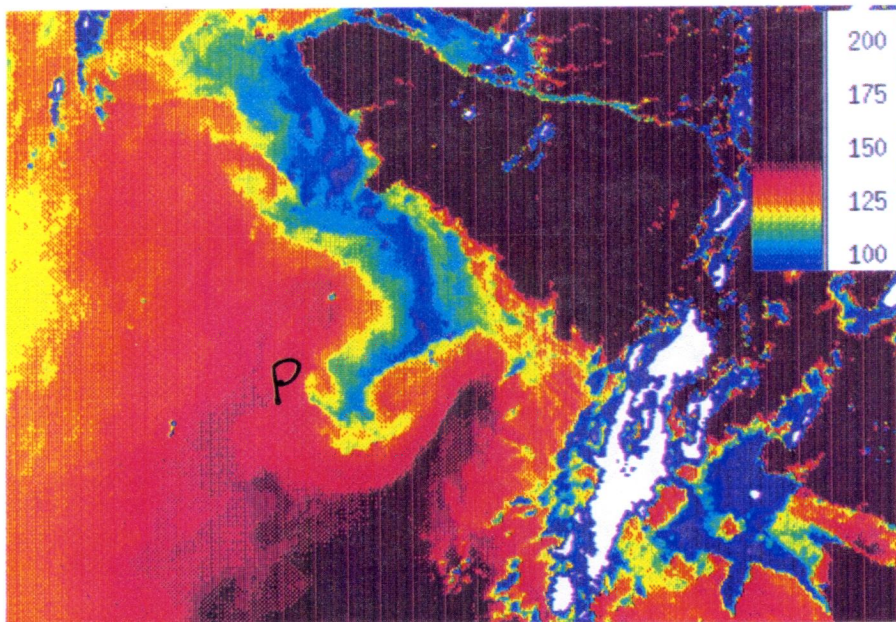
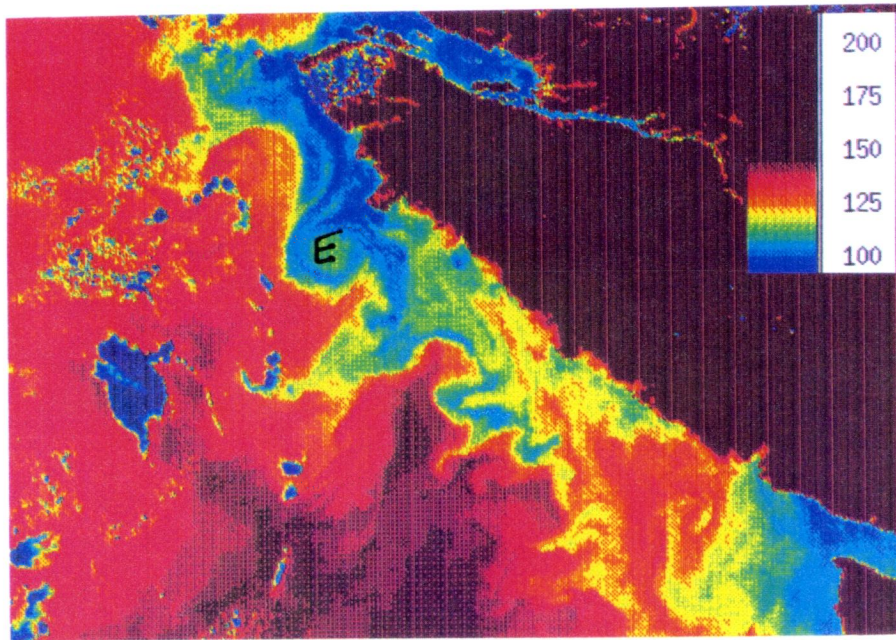


Figure 1.2. a) July 25,1985 AVHRR image showing an eddy off Brooks Peninsula b) August 2, 1988 AVHRR image showing a cold-water plume. Note the clouds (coloured white) in bottom image. The temperature scale ($\times 10^{-1}$) is shown in the upper right corner

In addition, the satellite imagery must be correlated with the dynamical process that is being observed. A few clear images between many days of cloudy imagery may show the presence of upwelled water along a coastline, but it may not be possible to ascertain what stage of the upwelling event that the cloud-free imagery is showing. It is therefore advantageous to have a time series of satellite imagery that spans the observed process.

The July 1984 imagery of the west coast of Vancouver Island covered a period of time when there was a dramatic increase in the upwelling-favourable winds. The imagery was available before, during and after the upwelling event, so it was possible to observe the spatial and temporal variations in the SST structure as the cold, upwelled water appeared at the surface of the ocean. In conjunction with the satellite data, coastal wind data were available from Estevan Point and Cape Scott, along the west coast of Vancouver Island, and near the end of the satellite coverage, an oceanographic cruise took place and a cross-shore CTD survey that included Estevan Point and Cox Point, provided hydrographic measurements within the water column (see Figure 1.3). In addition to current meter measurements offshore of Estevan Point, measurements of temperature were also available from two lighthouse sampling stations at Amphitrite Point and Kains Island. The data provided some insight into the upwelling event off Vancouver Island, and how the upwelling process relates to the appearance of cold water off Brooks Peninsula during the early stages of upwelling, the formation of cold water along the shelf break that is probably due in part to shelf break upwelling, the intensification of the shelf break current as the winds increased in strength, and the cold water that remained along the shelf break during a time of intense warming over the shelf as the winds decreased in strength.

1.2 The Study Area

Situated on the west coast of British Columbia, Vancouver Island is about 450 km in length, Figure 1.3. Although reference is made to the west coast of Vancouver Island, the main area of study was from Cape Scott, at the north end of Vancouver Island, to Cox Point in the south, a distance of 265 km. The offshore extent of the study was approximately 100 km (well beyond the shelf break), and this distance encompassed the spatial variability of the SST structure that was observed in the AVHRR satellite imagery. However, the width of the continental shelf varies along Vancouver Island, and at Brooks Peninsula, the continental shelf reaches its narrowest extent of about 8 km wide, with the depth rapidly dropping to over 1000 m within about 10 km of the shelf break.

Although more details will be given in the next chapter, the oceanography along Vancouver Island is highlighted by a number of characteristic features. As previously mentioned, the continental shelf width varies along Vancouver Island and is widest in the southern end where the broad extent of the shelf supports an active biological community. The broad shelf region is cut by the Juan de Fuca Canyon at the entrance to Juan de Fuca Strait; situated in the vicinity of the Canyon is the cyclonic Juan de Fuca Eddy (Freeland and Denman, 1982). In addition to the fresh water input from the Fraser River that makes its way to the ocean through the Juan de Fuca Strait, rivers and streams along the west coast of Vancouver Island act as fresh water sources (LeBlond et al., 1986). In response to seasonal changes in the wind field, the shelf break current changes direction (Ware and Thomson, 1986); during the summer months, predominately northwesterly winds drive the current equatorward, and during the winter months, southeasterly winds drive the shelf break current poleward. Inshore of the shelf break current, the Vancouver Island Coastal Current (VICC) flows poleward year-round (Freeland et al., 1984).

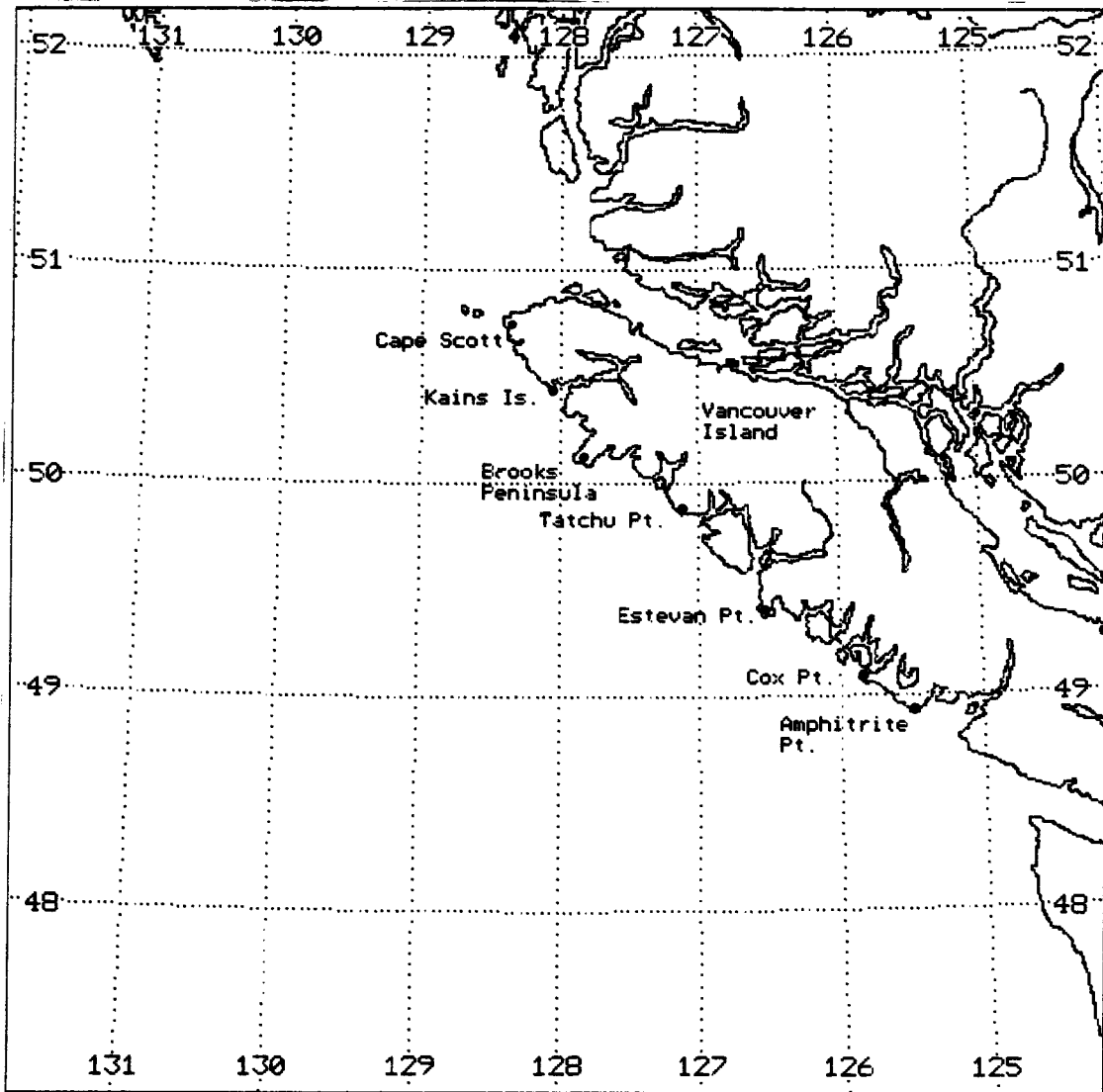


Figure 1.3. The Vancouver Island study area and location of place names.

1.3 Thesis Objectives and Overview

The preceding comments have introduced some of the important elements in the study of the shelf break current response to wind forcing and serve as a guide to some of the thought processes that have occurred during this study. The major objectives of this thesis will be to attempt to answer the following questions: 1) What are the spatial and temporal scales of the upwelling event? 2) AVHRR satellite imagery reveals the complex SST pattern during an upwelling event, but is the satellite data related to dynamical processes in the ocean interior or does it just represent surface features? 3) Is the cold water that initially appears at the tip of Brooks Peninsula and eventually migrates equatorward during an upwelling event due to advection by the mean currents or is there shelf break upwelling? 4) What dynamical processes are forcing the cold water to remain centered along the shelf break as the water migrates equatorward from Brooks Peninsula? 5) Is the observed upwelling event typical of the Vancouver Island response or are the observed SST patterns unique to the July 1984 event?

The next chapter will look at the oceanography around Vancouver Island. The variability of the seasonal wind field and the ensuing seasonal variability of the current structure will be discussed, and as well, previous observations of upwelling events are presented. Chapter 3 will concentrate on the satellite-data collection, processing and analysis. The basic procedure by which AVHRR data are converted into SST is outlined, and a comparison between AVHRR SST measurements and *in situ* temperature measurements is also presented. Chapter 3 also outlines the techniques that were used to enhance the satellite imagery, so that the spatial and temporal variations of the SST fronts are easier to identify than in the unenhanced imagery. The basic two-layer upwelling theory will be presented in chapter 4, and the conditions when shelf break upwelling is likely to

occur are presented. In addition, observations of shelf break upwelling are summarized. Chapter 5 begins by looking at the wind field, coastal temperatures, and the Bakun Upwelling Index during the upwelling event. The upwelling event is divided into four stages, and the Chapter 5 continues by discussing the SST variations during the upwelling event by using AVHRR imagery and cross-shore SST transects. Chapter 5 concludes by offering a dynamical interpretation of the upwelling event based on cross-shore thermal fronts, conservation of potential vorticity, and estimates of the long-shore velocity. Chapter 6 will summarize the observations and present concluding comments.

CHAPTER 2

THE OCEANOGRAPHIC SETTING

2.1 Vancouver Island Oceanography

2.1.1 Bathymetry

The rugged west coast of Vancouver Island is cut by many long, narrow inlets. The geography of the land is reflected along the continental shelf region where numerous canyons slice the shelf, Figure 2.1. The irregular, but broad shelf in the vicinity of Barkley Sound is highlighted by the Juan de Fuca Canyon. Freeland and Denman (1982) report the presence of a topographic upwelling centre that is driven by the interaction between the coastal currents and the Juan de Fuca Canyon, and results from later investigations reported by Ware and Thomson (1988) suggest that the upwelling in the canyon is linked to wind-induced upwelling along the outer shelf. The quasi-permanent eddy that is frequently observed in the vicinity of the Canyon is commonly called the Juan de Fuca Eddy. North of Barkley Sound, the shelf is more regular, but gets progressively narrower until reaching the narrowest point just off Brooks Peninsula.

AVHRR satellite imagery of the SST patterns along Vancouver Island frequently shows significant variation north and south of Brooks Peninsula that is due in part to the variability in the topography along the continental shelf. Across-shore transects digitized from hydrographic charts (Fig 2.2) show the dramatic differences for various locations along Vancouver Island. At the northern end of Vancouver Island, Kains Island has a shelf

width of around 15 km, and beyond the shelf the depth quickly drops to over 1500 meters (see Figure 1.3 for the location of Kains Island). Tatchu Point displays similar shelf topography to Kains Island, but with a slightly wider shelf and a more gradual decrease in depth beyond the shelf.

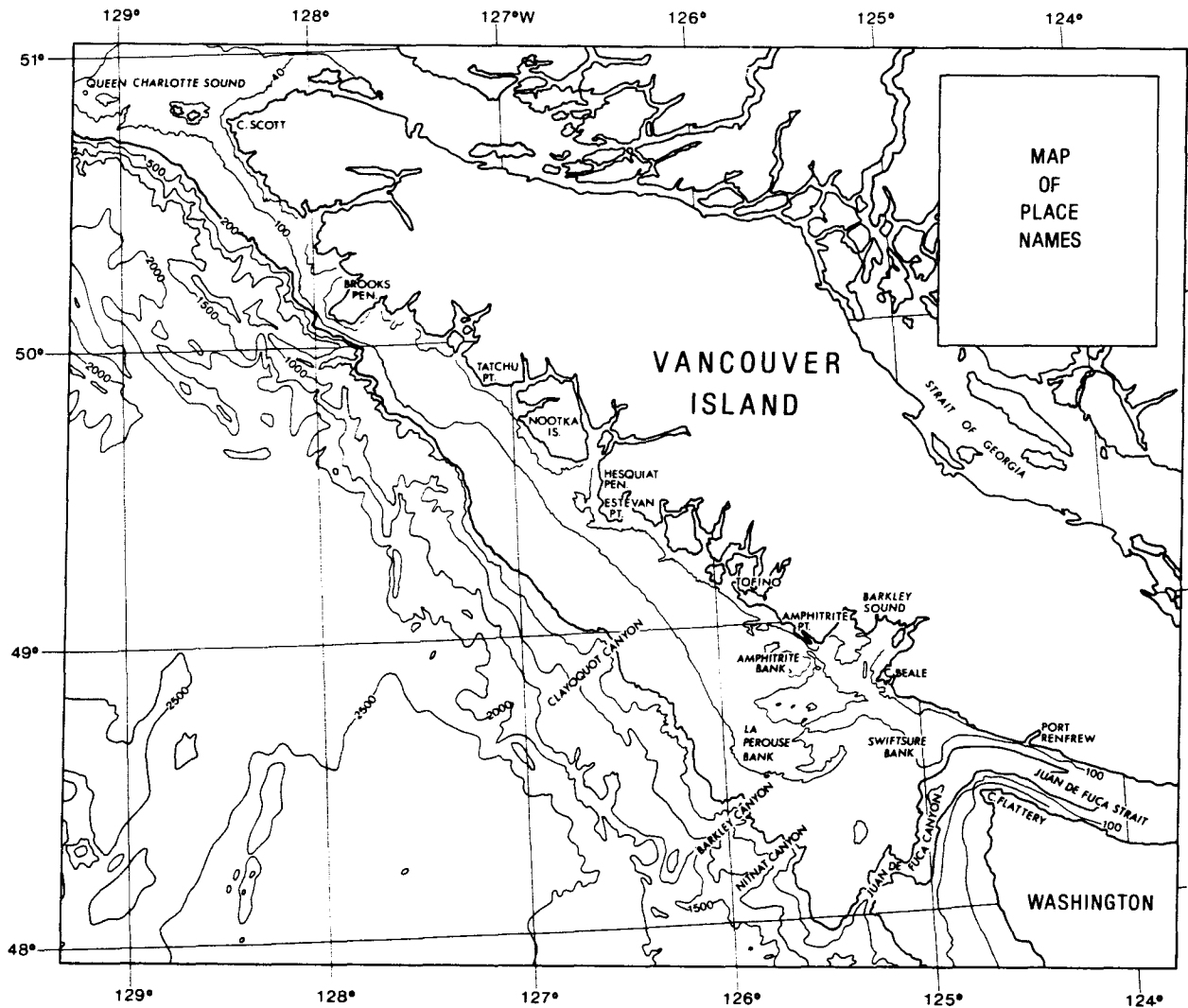


**Figure 2.1. Bathymetry along Vancouver Island.
From Thomson (1990)**

At Brooks Peninsula, between Kains Island and Tatchu Point, the shelf-width is narrow, and the steep topography beyond the shelf rapidly drops to over 1000 m deep and forms the seaward head of Quoukinsh Canyon. At the southern end of Vancouver Island, Cox Point (just northwest of Tofino) has a wide shelf region with an offshore extent of nearly 50 km that gradually drops to 1500 m deep over the next 35 km.

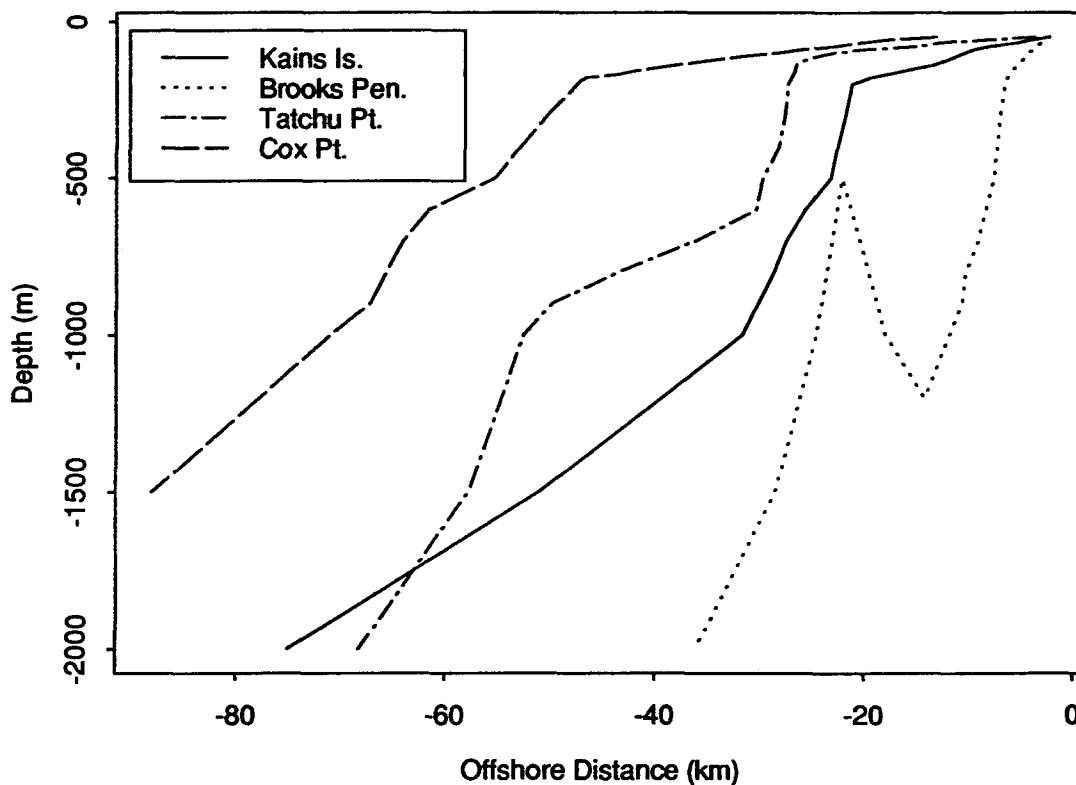


Figure 2.2. Bathymetric cross-sections at selected locations along Vancouver Island.

2.1.2 Winds and Currents

The currents along Vancouver Island have been studied as far back as the 1930's. In most cases, the inferred current structure was based on observations of temperature and salinity and the use of the geostrophic method. In 1974, the first use of submerged current meters was used to measure coastal currents off Tofino, and between May 1979 and September 1980, the Coastal Ocean Dynamics Experiment (CODE) was the first major investigation of the circulation and water properties along Vancouver Island; this study entailed numerous current moorings both on and off the shelf, and extensive hydrographic sampling (Thomson et al., 1986a, and Freeland et al., 1984). In the early 1980's, AVHRR satellite data were readily available and Emery et al. (1986) adapted techniques that had been used to detect ice and cloud motion and developed an objective method to estimate surface currents; their approach used a maximum cross-correlation procedure between a small subset of the first image and a slightly larger search area in the succeeding image.

Based on geostrophic analysis, Dodimead et al. (1963) and Favorite et al. (1976) commented on the seasonal cycle of the current structure off Vancouver Island. During the summer, a period of weak northwest winds prevail which result in relatively weak currents and meanders and eddies were frequently observed. In the winter, strong southeast winds produce stronger currents than the summer conditions, and the occurrence of meanders and eddies was less pronounced. Between the summer and winter flow regimes, there were variable currents associated with the change of the mean wind direction which result in the Spring Transition and the Fall Transition. Sea level pressure, averaged between 1946 and 1988 for the months of January (winter regime) and July (summer regime), obtained from

the Comprehensive Ocean-Atmosphere Data Set archive indicate that during the winter, the Aleutian Low dominates, and the coastal winds along the west coast of Vancouver Island are predominantly from the southeast (Thomson 1981); the strongest winds are observed from October through March, and by April the Aleutian Low has weakened considerably. Between April and September, the North Pacific High dominates the atmospheric pressure distribution and the coastal winds along Vancouver Island are typically from the northwest.

The large scale seasonal variation in the atmospheric pressure distribution also appears in the seasonal structure of the winds along the coast of Vancouver Island and influences the dynamical processes over the shelf region. Bakun winds, (Figure 2.3) , which are calculated from 6-hourly synoptic pressure analysis for a 3-degree latitude/longitude grid (Mason & Bakun, 1986) are shown for the location 49° N, 126° W, approximately 10 km seaward of Amphitrite Point. The monthly mean winds clearly shows the seasonal variation in the wind direction with winds from the southeast during the winter months, and upwelling favourable winds from the northwest during the summer months. Thomson (1983) observed that for periods greater than two days, the synthetic Bakun winds are representative of the actual winds.

The combination of a good understanding of the seasonal wind structure and an extensive field program during the CODE led Freeland et al. (1984) to resolve the seasonal circulation pattern along Vancouver Island. During the winter (Figure 2.4a), the northward flowing Davidson Current is observed seaward of the shelf, and the buoyancy driven Vancouver Island Coastal Current flows northward over the shelf (Hickey et al., 1991) with current speeds of 30 to 40 cm/s observed approximately 15 km from shore. During the summer months (Figure 2.4b), the offshore flow reverses direction in response to the changing winds and the southward flowing shelf-break current is observed, reaching peak speeds of about 20 cm/s during August.

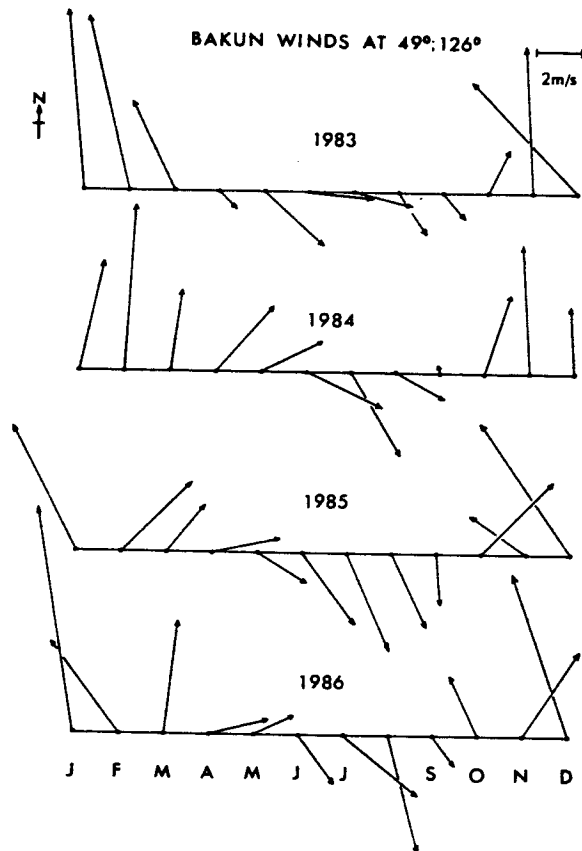
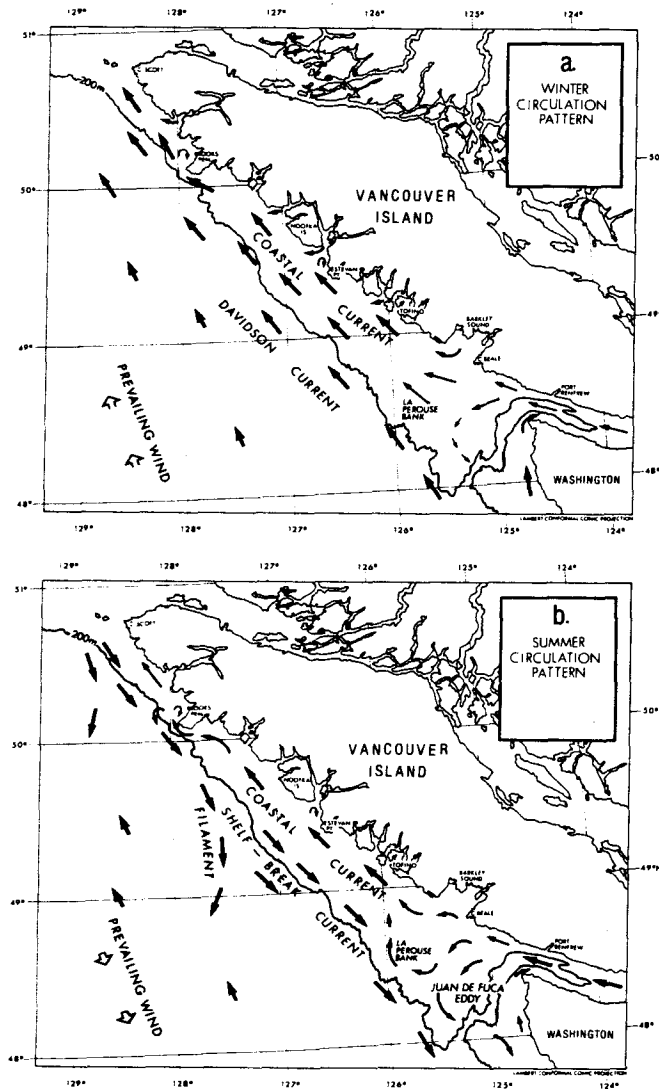


Figure 2.3. Monthly mean Bakun "winds". From Thomson et al. (1990).

In contrast to the offshore flow, the Vancouver Island Coastal Current continues to flow northward, but with currents speeds slower than in the winter. Observations of the shelf break current by AVHRR satellite imagery frequently shows the formation of plumes and filaments that can extend up to 100 km offshore. These filaments, similar to those observed

in the California Current System by Mackas et al. (1991) and Ramp et al. (1991) can cause a significant flux of biomass from the coastal to the offshore waters, and in addition, the fate of particulate and dissolved carbon that may be transported offshore in the filaments is one aspect of a study reported by Denman et al. (1992).



**Figure 2.4. Circulation along Vancouver Island
a) winter regime, b) summer regime. From
Thomson (1990).**

Current meter data from the Coastal Ocean Dynamics Experiment also revealed a more complete picture of the vertical current structure that was best resolved off Estevan Point during July, 1980. As depicted in Figure 2.5, the northward flowing Vancouver Island Coastal Current is present within 20 km of the coast. In the top 300 m, centered seaward of the shelf break, there is strong seasonal jet that reverses direction in response to changes in the large-scale wind field. Below the seasonal jet, there is a persistent northward flow which is probably an extension of the California Undercurrent. In the offshore regime, there is deep-sea circulation which fluctuates substantially, but does not show as clear a seasonal cycle as the inshore currents.

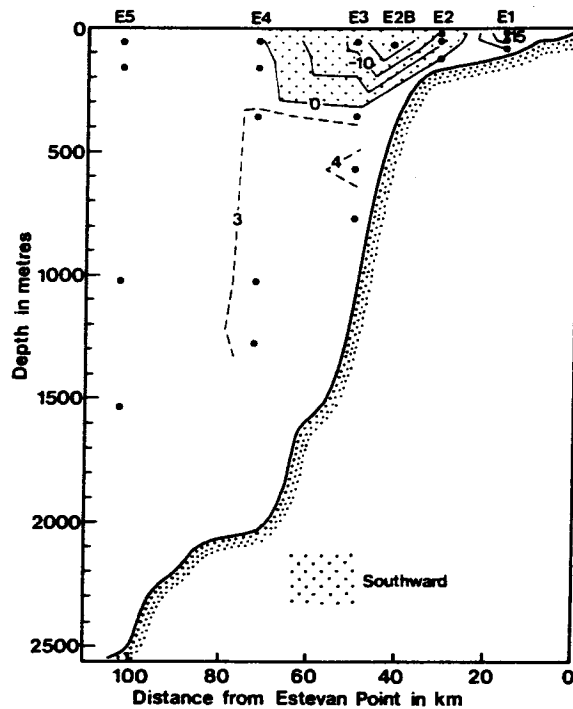


Figure 2.5. Currents off Estevan Point during July, 1980. From Freeland et al. (1984).

2.2 Vancouver Island Upwelling

2.2.1 Overview

In its simplest physical conceptual interpretation, upwelling is a process that draws cold, subsurface water into the warmer surface layer of the ocean. The extension of the conceptual model to the solution of the mathematical equations that model the upwelling process is an exceedingly complex problem; however, the salient features of the upwelling process can be explained in conceptual terms. In the northern hemisphere, upwelling favourable winds blow with the coastline to the left of the wind direction. Due to the Coriolis force, the net transport in the surface Ekman layer (the upper 20 - 50 m) is in the offshore direction. Conservation of mass requires that the offshore flow must be balanced, and this balance is in the form of an onshore flow that upwells water along the coast (coastal upwelling) and at the edge of the continental shelf (shelf break upwelling).

Due to the constraints of no flow through the coastline, the upwelled water must move in a vertical direction which results in the upward bending of the isopycnal surfaces toward the coast, and the resulting pressure gradient causes an increase in the equatorward long-shore current leading to what Charney (1955) called a coastal or surface jet. The width of the jet is given by the baroclinic Rossby radius of deformation, $a = c/f$ (Gill, 1982), where c is the speed of a long internal wave, and f is the Coriolis parameter, which at mid-latitude in the northern hemisphere has a typical value of $(10^{-4}) \text{ s}^{-1}$; in the case of a two-layer fluid, $c^2 = g'H$, g' is the reduced gravity, and H is the equivalent depth given by $H_1H_2/(H_1 + H_2)$. The Rossby radius increases toward the equator, and according to Emery et al. (1984), the internal Rossby radius in the vicinity of Vancouver Island is typically 15 to 20 km; in contrast, the external Rossby radius in the in the Vancouver

Island region is around 1300 km. In concert with the formation of the coastal jet, a weak, subsurface poleward-flowing undercurrent develops over the shelf. These features are typical of an upwelling event, but spatial and temporal variability can readily occur when other factors such as topography, stratification, the presence of capes, and variations in the wind field are taken into consideration.

2.2.2 Observations

Upwelling occurs along the continental margins in many areas of the world, notably the coast of Africa, Peru and the west coast of Canada and the United States. In a comparative study of the upwelling regions off Oregon, northwest Africa, and Peru, Smith (1981) observes that local long-shore winds are the primary cause of the upwelling response, but the response is also a function of the topography and stratification. The seasonal cycle of the winds and the similarities in the stratification group Africa and Oregon together, but it is possible to pick out some differences. Smith continues by commenting that in contrast to the other areas, the upwelling response off Peru shows significant differences. The winds off Peru are nearly always upwelling-favourable and hence do not display a dominant seasonal cycle, and in addition, the year to year variations associated with El Niño can affect the upwelling response. Upwelling off Vancouver Island is similar to that off Oregon, but because Vancouver Island is at the northerly limit of a substantial upwelling season, the upwelling response is not as strong as it is to the south (Freeland and Denman, 1982).

Most of the upwelling studies off the coast of Vancouver Island have been done over the last decade, due in part to the convenient access to AVHRR satellite data. The spatial variability of the upwelling signal makes satellites an ideal platform from which

observations of SST structure during an upwelling event can be readily observed. Using AVHRR satellite data, Ikeda and Emery (1984) observed an upwelling event off Vancouver Island during the summer of 1980. Before the intensification of the upwelling-favourable winds, there was a cold band of water over the shelf break. As the winds increased, there was a simultaneous decrease in the SST near the coast, and the offshore boundary of the coastal band of cold water propagated seaward to the shelf break at a speed of about 10 km/day. At the end of the upwelling event, the cold band of water remained over the shelf break and warmer water appeared over the shelf. The authors continue by saying that the cold band of water that remained could be an indication of shelf break upwelling or the advection of cooler surface water from north of Brooks Peninsula. In a study by Jardine (1991), the area around Brooks Peninsula was pinpointed as a source of upwelled water in response to northwesterly winds, but the response was limited to an area around the south coast of Brooks Peninsula, so it was not possible to estimate if cold water was advected southward, thus accounting for the band of cold water that remained over the shelf break in the Ikeda and Emery result.

In a recent study by Fang and Hsieh (1992), Empirical Orthogonal Function (EOF) analysis of eight summers of AVHRR satellite imagery off Vancouver Island had four dominant EOF modes. Accounting for 33% of the variance, mode 1 resembled the mean of all the images. The second mode, which represented 12% of SST variance, showed a topographic upwelling response in the form of a zero crossing line that is approximately aligned with the 200 m contour, thus suggesting upwelling over the shelf break. The third mode (9% of the variance) showed cool water extending southwestward off Brooks Peninsula, and the fourth mode (5% of the variance) showed a cool water plume extending off Cape Scott. The third and fourth modes could represent water that is upwelled in the vicinity of Brooks Peninsula and Cape Scott and then advected southward by the prevailing winds.

Many of the observations of upwelling off Vancouver Island display the features that are indicative of a classical upwelling response. In all cases, the importance of a long-shore coastal wind as the dominant forcing mechanism has been noted, and the appearance of cold water along the coast, and in some instances along the shelf break, was observed. Compared to studies off the coasts of Oregon and California, investigations of upwelling off Vancouver Island are sparse. The higher occurrence of studies off Oregon and California is perhaps related to the stronger upwelling signal and the importance of upwelling to fisheries in these regions.

In spite of less intensive studies of upwelling off Vancouver Island compared to areas to the south, the dynamical processes affecting the upwelling response off Vancouver Island are complex. Crepon et al. (1984) have shown that the intensity of the upwelling is greater on the leeward side of a cape compared to the windward edge; the rectangular cape in this study is similar to Brooks Peninsula at the northern end of Vancouver Island. Brooks Peninsula was the subject of a study by Freeland (1990) and he showed that a southward long-shore flow (shelf break current) can support topographic Rossby lee waves, and strong offshore flow occurs on the downwind edge of the Peninsula and produces features that look like squirts and jets which are occasionally observed in AVHRR satellite imagery. A study by Peffley and O'Brien (1976) suggests that bottom relief is more important than variations in coastline geometry in causing localized upwelling. However the effect of a 20 km long headland (Brooks Peninsula) that protrudes into a 20 to 40 km horizontal-scale flow (shelf break current) cannot be ignored. Variations in the long-shore topography was the central issue in a study by Janowitz and Pietrafesa (1982). These authors showed that the lowest-order barotropic flow was along the isobaths, and upwelling occurred if the slope decreases in the downstream direction so that the isobaths diverge. The results of the Janowitz and Pietrafesa study may apply in the

region between Brooks Peninsula and the shelf region off Barkley Sound where the slope of the continental shelf changes dramatically between these two locations.

2.3 Summary

The North Pacific Ocean sea level pressure distribution is dominated by the presence of the Aleutian Low during the winter months and the North Pacific High during the summer months. The large scale pressure variations force a seasonal cycle in the winds along the west coast of Vancouver Island. During the winter, the winds are predominantly from the southeast, and the poleward flowing Davidson Current is observed along the shelf. Confined to within approximately 20 km of the coastline, the buoyancy driven Vancouver Island coastal current also flows in a northerly direction. The transition to the summer-regime flow conditions occurs during the Spring Transition, around March or April, and the coastal winds are driven by the North Pacific High.

During the summer, the winds are predominantly from the northwest, and upwelling is a common occurrence off Vancouver Island. Longshore winds drive the upwelling, but variability in wind strength and topography can modify the upwelling response. The summer-regime winds also produce a change in the mean circulation pattern off Vancouver Island. The equatorward shelf break current is established in the top 300 m of the water column, and is roughly centered seaward of the shelf break. Despite the change in the wind direction, the Vancouver Island Coastal Current continues its primarily northward year-round flow. Sometime in the late September, early October time frame, the Fall Transition occurs, and the winds return to blowing primarily from the southeast. In the offshore region, there are fluctuations in the circulation, but the seasonal variability does not appear related to the coastal cycle

CHAPTER 3

DATA COLLECTION AND PROCESSING

3.1 Advanced Very High Resolution Radiometer

3.1.1 Background

Since the days of using a weighted cable to measure the depth of the ocean, there have been major advances in the development of instruments to measure various ocean properties. Measurements of temperature have always been important in oceanography, and through the initial use of reversing thermometers to present day electronic temperature measurements taken by CTD probes, the thermal structure of the ocean has become better understood. However, most of the temperature measurements are discrete samples that are usually separated by tens of kilometers, and in the open ocean, the sampling separation distance can extend to hundreds of kilometers due to the vast expanse of the oceans. To provide a more extensive spatial picture of the surface thermal structure of the ocean, thermal infrared (IR) scanners were developed. The first generation of IR scanners were subject to a number of problems that included poor spatial resolution, and a high degree of electronic noise that introduced significant spatial and temporal errors (Legeckis, 1978).

Infrared scanners were initially flown on aircraft, and were later introduced as part of the instrument package on meteorological satellites. In 1972, a Very High Resolution Radiometer (VHRR) was placed on the NOAA series of polar orbiting meteorological satellites. The VHRR scanner offered better spatial resolution and decreased electronic noise compared to the first generation of IR scanners. With the improvements in the IR

measurements, VHRR measurements from satellites could be routinely taken, and the broad spatial coverage that satellite radiometers provided enabled the detection of SST fronts associated with ocean currents and upwelling. In 1978, the Advanced Very High Resolution Radiometer (AVHRR) was placed on the NOAA satellites. In contrast to the one visible and one infrared channel, and the analog data transmission scheme of the VHRR sensor, the AVHRR sensor had two visible and two infrared channels, and transmitted 10-bit binary data in High Resolution Picture Transmission (HRPT) mode that provided 1024 radiance level measurements. The AVHRR/2 sensor was introduced shortly after the AVHRR sensor and provided a third infrared channel.

Table 3.1 list some of the major characteristics of the advanced very high resolution radiometer, specifically the AVHRR/2 sensor. The sensor has five channels that span the electromagnetic spectrum from the visible through the infrared wavelengths. Channel 4 is typically used to measure the SST due to the balance between atmospheric transparency and the peak of the thermal emission occurring in the 10.3 to 11.3 μm wavelength range. Channel 3 suffers from a high degree of solar reflectance during the day, but can be readily used for nighttime measurements of the SST. The spatial resolution of AVHRR imagery is 1.1 km at the nadir point (a point on the earth directly below the satellite), but increases to around 7 km as measurements are taken near the outside edge of the 2580 km swath width. The instrument noise is usually converted into a Noise Equivalent ΔT , NE ΔT , where ΔT refers to the apparent change in temperature. The NE ΔT value of 0.12 K at 300 K means that AVHRR measurements can detect relative changes in the SST of around 0.12 K, but in practice the NE ΔT value is usually higher due to the introduction of errors such as calibration errors, and atmospheric effects (Robinson, 1985), and Kaufman and Holben (1993) comment on errors introduced by the drift of the NOAA-7 AVHRR sensor between 1981 and 1990.

AVHRR/2 Sensor		
Wavebands(μm)	Channel 1	0.58-0.68
	Channel 2	0.725-1.10
	Channel 3	3.55-3.93
	Channel 4	10.3-11.3
	Channel 5	11.5-12.5
Sensitivity (IR)	NEAT	0.12 K at 300 K
Digitization levels		1024
Resolution		approx. 1.1 km
Swath width		2580 km

Table 3.1. Characteristics of the AVHRR/2 sensor

3.1.2 Sea Surface Temperature

The basic principle underlying the operation of IR sensors is that the wavelength that black bodies emit is temperature dependent. The sun emits at short wavelengths with peak emission in the visible, and the thermal emission from the earth peaks around 10 μm , in the infrared range. The spectral characteristics of black bodies are given by Planck's radiation law which are plotted for various temperatures as shown in Figure 3.1. Thermal emissions from the earth are in the 300 K range. The emissivity, which is the ratio of emittance for a real surface at a given temperature to that of a black body at the same temperature, is around 0.98 for the sea surface and thus the sea surface radiates very nearly as a black body.

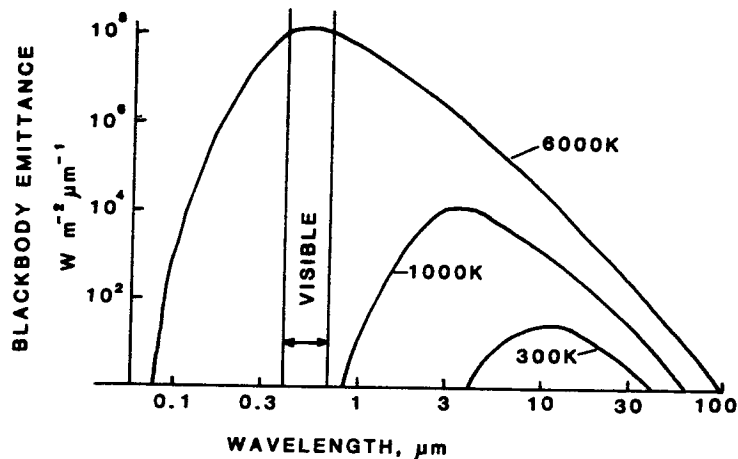


Figure 3.1. Emission spectra at different temperatures. From Robinson (1985).

Black-body radiation characteristics are utilized to measure the SST by using an AVHRR sensor. On the satellite, a black-body cavity is heated to some temperature and this temperature is measured by four Platinum Resistance Thermometers (PRT). At the end of each AVHRR earth scan line, the AVHRR sensor views the black-body and views cold, deep space (deep space is assumed to be 4 K). Therefore, each scan line contains a digitized value of the radiance level from the earth for all five channels, plus radiance levels from the on-board black-body and deep space. In addition, the temperature of the black-body is calculated by taking the average of the four PRT measurements.

Prior to the launch of the satellite, the AVHRR sensor is calibrated so that its response as a function of wavelength is known. By combining the sensor response function, the Planck radiation law, and the radiance level measurements from the satellite black-body and deep space, a relationship between the digitized radiance levels that the AVHRR sensor measures and the temperature can be calculated (see Robinson, 1985 for further details). The relationship between radiance level and temperature can be applied to the radiance levels that were obtained from viewing the earth, and the earth radiance levels can be converted into a temperature. In summary, the AVHRR sensor scans perpendicular to the flight direction of the satellite, and for each approximately 1.1 km square area on the earth (varies with scan angle), a radiance level is measured and hence for the appropriate channel, a temperature is calculated. The radiance levels are continuously measured from the satellite, so that a radiance level map of the earth is produced that has a meridionally extent equaling the swath width of the AVHRR sensor (2580 km), and a zonal extent that is limited by the reception range of the ground station, which for the UBC Satellite Oceanography and Meteorological Lab (SOMeL) extends from the Baja Peninsula to the Beaufort Sea.

3.2 AVHRR Data Processing

3.2.1 The Data Set

As previously mentioned, the initial requirement when using AVHRR satellite data is that a sufficient number of cloud-free images are available that adequately represent the spatial and temporal variability of the observed dynamical process. Along the west coast of Vancouver Island, the highest probability of obtaining cloud-free images occurs during the summer months (June through September). In addition, the July through September time frame coincides with the strongest upwelling signal and the peak velocity of the shelf break

current. Using the summer months as a time frame guide, approximately 400 AVHRR satellite images between 1980 and 1991 were obtained from the SOMeL archive and subsequently navigated and calibrated (navigation and calibration described below). Of the original 400 images, 110 images over all years satisfied the minimum criteria of being reasonably cloud-free along the west coast of Vancouver Island. The 110 images used were not evenly distributed over all years. Depending on the weather, some years had considerable more cloud-free images and image sequences than other years. In conjunction with a good image sequence, there was the additional requirement of obtaining other data to support the satellite imagery. A sequence of imagery obtained from July 1984 provided the best combination of satellite coverage and the availability of hydrographic and wind data.

Table 3.2 lists the satellites used and the local time that the satellite was over Vancouver Island during the study period in 1984. For all of the satellite passes, Vancouver Island was within a reasonable distance of the sub satellite track (a line projected along the earth that is directly below the satellite), and therefore, the maximum 1.1 km resolution was obtained for each satellite image. The times of the satellite passes were usually in the late afternoon or early evening, but two passes were in the morning. The SST measurements taken in the afternoon are probably comparable with each other, but care must be taken when comparing the morning passes to the other passes. The consistency of the afternoon and evening passes is due to the relatively small change of the net heat flux at the sea surface during this time. However, during clear nights, there is a significant flux of heat away from the sea surface, so the morning SST measurements may show an apparent decrease, and as the solar radiation from the sun increases during the day, there will be an apparent increase in the SST. The diurnal variation in the SST must be considered when comparing daytime and nighttime imagery, but spatial variability, where the relative SST between regions on the image does not vary significantly, can be readily compared for nighttime and daytime imagery.

Satellite	Date and Time
NOAA 6 26231	July 13 19:44 PDT
NOAA 7 15779	July 14 16:51 PDT
NOAA 6 26253	July 15 09:11 PDT
NOAA 7 15793	July 15 16:39 PDT
NOAA 7 15807	July 16 16:26 PDT
NOAA 6 26274	July 16 20:06 PDT
NOAA 7 15821	July 17 16:14 PDT
NOAA 6 26288	July 17 19:48 PDT
NOAA 7 15835	July 18 16:02 PDT
NOAA 6 26302	July 18 19:24 PDT
NOAA 7 15863	July 20 15:37 PDT
NOAA 6 26367	July 23 09:20 PDT
NOAA 7 15906	July 23 15:41 PDT
NOAA 7 15920	July 24 16:28 PDT
NOAA 6 26388	July 24 20:20 PDT

Table 3.2. Satellite number and orbit, and time of data reception

3.2.2 Navigation, Calibration, and SST Retrieval

Satellite image navigation or geocoding, is a process by which the raw satellite image is transformed into a selected geographic map projection. The navigation process also includes corrections for geometric distortions caused by satellite orbit variations, satellite altitude, and geometric distortions due the Earth shape and rotation. According to Emery et al. (1989), and Emery and Ikeda (1984) there are essentially two methods to navigate polar-orbiting satellite data, and both methods yield similar results; in both cases, the geometric transformation scheme to rotate the image to an acceptable map projection is similar, but the procedures to correct for geometric distortions is different. In the first case, only a limited knowledge of the satellite orbit is available and the navigation procedure relies on the extensive use of Ground Control Points (GCP) to correct for errors. In the second case, highly accurate ephemeris data (orbital parameters) are used to locate the satellite as a function of time, and ground control points are only required to correct for satellite timing errors and altitude. For both navigation schemes, the authors report location accuracy in the order of 2 km. The SOMeL uses the second method of navigation, and a process called nudging is also used to correct for satellite timing errors. The nudging procedure requires the image to be shifted to whatever geographic features are present in the image, thus obtaining location accuracy in the 2 km range. The second navigation scheme is more accurate than the first when no GCP are available; the lack of GCP can easily occur when the satellite image does not include land.

The calibration component of the images processing converts the digital radiance levels into a measure of the temperature. As outlined above, the calibration procedure to convert from the AVHRR sensed radiance levels to the SST is well known, but due to atmospheric effects, the radiance measured may not represent the true SST. As outlined by

Abbott and Chelton (1991), some of the atmospheric effects that can reduce the transmission of IR radiation through the atmosphere and cause an apparent reduction in the SST include variable amounts of water vapour in the air, the presence of aerosols in the stratosphere from sources like the 1991 volcanic eruption of Mt. Pinatubo, and the largest single source of error is due to the presence of undetected clouds. Various methods such as those developed by Walton et al. (1990), and McClain et al. (1982) have been reasonably successful in using the multi-channel capacity of the AVHRR data to correct for atmospheric effects.

Another source of error in the calculation of the SST is due to the variability of the thermocline structure of the ocean. As shown in Figure 3.2, the near-surface temperature of the ocean can vary depending on the degree of wind mixing and the time of day when the SST is measured. Temperatures as high as 21° C have been measured in the top surface layer in a few British Columbia fjords on calm, sunny days (Thomson, 1981). The temperature in the upper few meters of the water column represent the so called bulk sea surface temperature, but the AVHRR sensor only measures the top 0.1 mm, the so called skin temperature. However, studies by Wick and Emery (1992), Schluessel et al. (1990), and Emery (1989) have shown that the skin temperature is reasonably representative of the bulk sea surface temperature, but the agreement depends on the depth of the upper mixed layer.

3.2.3 *In Situ* Comparison

Given the degree of processing required and the possibility for errors, it is sometimes surprising that AVHRR measurements of the SST yield the reasonably accurate results that are routinely obtained. Studies by Tabata (1981) off Vancouver Island report

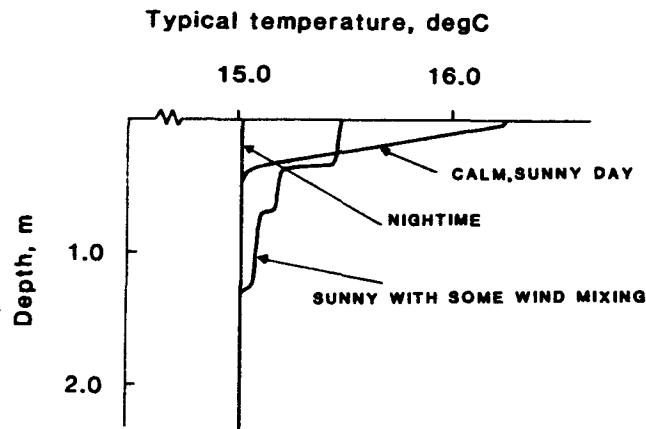


Figure 3.2. Typical near-surface temperature profiles. From Robinson (1985)

good agreement between AVHRR measurements of the SST from satellites as compared to *in situ* SST measurements from ships; significant deviations between the two temperature measurements are typically due to atmospheric effects, radiometer calibration errors, or errors in shipborne measurements. At the end of the July 1984 study, an oceanographic cruise took place off Vancouver Island and shipborne measurements of the SST were compared to those obtained from the satellite. For quality control in the comparison of satellite and buoy SST measurements, Walton et al. (1990) suggest that the satellite measurements should be within four hours of the *in situ* measurements. The July 1984 data set contained one satellite pass that coincided with *in situ* SST measurements that was within the time guideline, and the SST from this image was correlated with the near-surface hydrographic measurements of the temperature.

Temperature measurements were obtained from Line E (Cox Point) off Vancouver Island (see Figure 3.5); station E1 (over the 50 m isobath) was sampled at 7 pm Pacific Daylight Time (PDT) on July 24, 1984 and station E9 (over the 1500 m isobath) was sampled at 2 am (PDT) on July 25, 1984. At 8:20 pm (PDT) on July 24, 1984, there was an overpass of the n6 spacecraft (orbit number 26388). In future, unless otherwise indicated, the convention will be adopted that all times will be PDT, the year will be 1984, and the satellites will be referred to as n6 or n7 plus the orbit number; in this comparison case, the satellite reference name is n6.26388. The channel 4 n6.26388 image was navigated and calibrated, but there were no corrections for atmospheric effects applied to the image.

The latitude and longitude of each station (E1-E9) was converted into image coordinates, and for each pixel that corresponded with a hydrographic station, the average temperature of the surrounding four pixels was calculated, and the average temperature was assigned to the central pixel value. The averaging process helped to reduce the errors due to the conversion from geographic to image co-ordinates and errors due to the navigation process. The comparison between surface shipborne-measurements and the satellite measurements of the SST is shown in Figure 3.3a, and Figure 3.3b shows the correlation coefficient (r) as a function of the depth. At the surface, the correlation coefficient is around 0.9, increases slightly between 2 and 3 m of depth, and drops off significantly after 3 m. One-metre averaged temperature profiles show a sharp decrease in the upper 5 m, and the correlation increase is presumably due to the AVHRR SST, which is slightly less than *in situ* surface temperatures (Figure 3.3a); the lower AVHRR-sensed measurements are in better agreement with CTD measurements a few metres below the surface. Although there are only nine sample pairs, the assumption will be made that the temperature correlation agree over the entire spatial extent of the study area for a single image, and that the agreement will also hold for the entire July sequence of images.

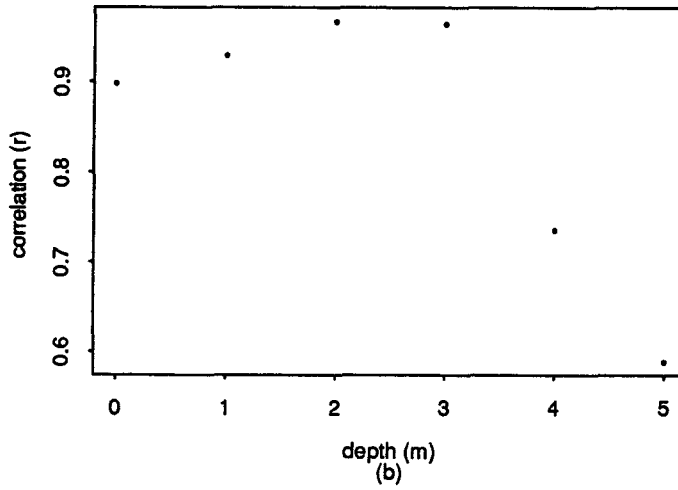
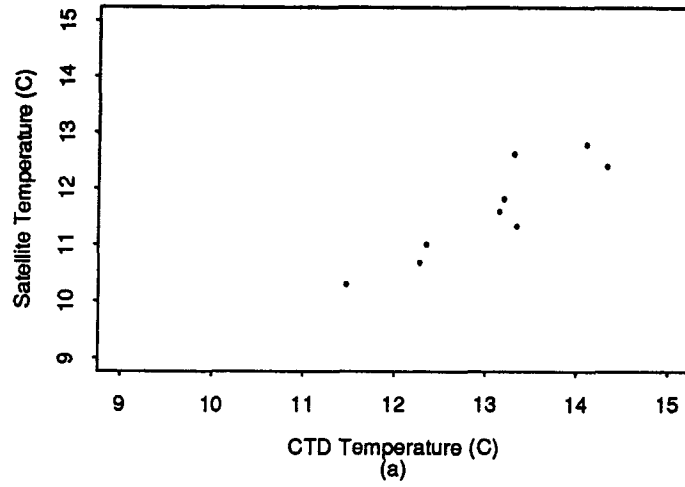


Figure 3.3. a) Comparison of AVHRR SST (n6.26388) and *in situ* SST (Line E) b) Same as in (a), except AVHRR SST compared to Line E for increasing depth.

3.3 Image Analysis

3.3.1 Feature Identification

There are numerous digital image processing techniques that help to produce clear pictures of the SST structure and aid in the identification of oceanographic features. One of the basic techniques is image enhancement. The process of image enhancement relies on the distribution or histogram of pixel values for a given image. Most images are converted from a 10-bit to a 8-bit format during the calibration process, which will yield, in the case of a channel 4 IR image, a temperature range between 0 and 25.5° C (pixel values are displayed as integers between 0 and 255 and the decimal point is mentally inserted). In the case of summer-time image at mid latitude, low temperature values are usually associated with clouds, mid-range temperatures typify the ocean, and high temperatures are associated with land (Figure 3.4). If the range of ocean temperatures is known, then all pixel values less than the minimum ocean temperature can be set to some value, say zero, and all pixel values greater than the ocean temperature can be set to some value, say 255. The enhancement function is designed to set high and low pixel values (temperatures) equal to some constant, and the pixel values that represent the ocean temperature are linearly stretched. The linear stretching increases the contrast between adjacent pixels and makes the SST gradients easier to detect.

Another technique for feature identification is an edge detector. The basic principle in edge detection is to calculate the sea surface temperature gradient in two orthogonal directions for an image. The gradient indicates if there are changes in the pixel values, which in the case of SST, might indicate the location of a temperature front.

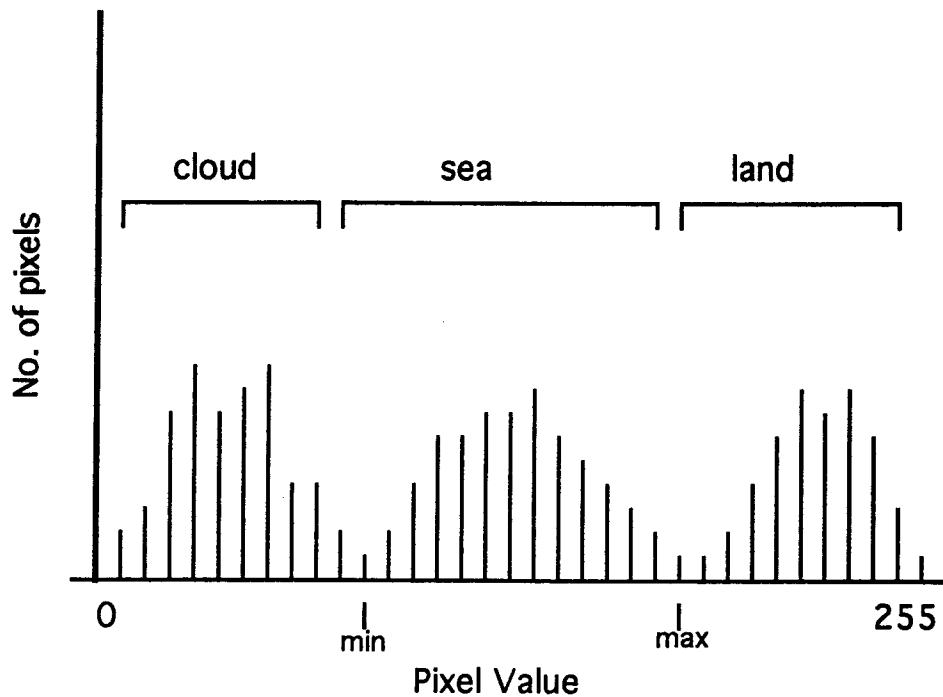


Figure 3.4. Typical histogram of a thermal IR image. Adapted from Robinson (1985)

Simpson (1990) indicates that prior to applying an edge detector routine to an image, the image should be cloud-screened, and in addition to cloud-screening, Jensen (1986) comments that the application of a low-pass filter to the image will produce the most striking edge enhancement. Cloud-screening was done in two different ways. The first method was by visual inspection. Since the spatial variation of clouds is different than the spatial variation of the SST structure, a low temperature SST front will appear spatially different from a cloud formation. The visual inspection process works well for thick clouds, but thin clouds and fog are more difficult to detect. The second method uses the multi-channel capacity of the AVHRR data to do the cloud-screening. Liquid water drops are strong scatters in channel 1 (visible wavelength), and cloud reflectivity can approach

70 percent (Saunders and Edwards, 1989); therefore, the presence of clouds will increase the scatter of the incident solar radiation and hence increase the amount of solar radiation that is reflected. A channel 1 threshold value of 75 was used to detect the presence of clouds. When a channel 1 pixel value was greater than 75, the corresponding pixel in the channel 4 (IR) image was set to zero. The visual inspection scheme and the multi-channel procedure were useful for detecting the presence of clouds, although both methods required some subjective interpretation of the final results.

Variations in the SST usually occur over a large spatial extent, so the application of a low-pass filter to an image will block the high spatial frequency detail. The 3x3 weighted-filter, as indicated by (3.1), was developed by Wang et al. (1983); compared to an unweighted filter, the unequal size of the matrix elements helps to reduce image blurring by attenuating the loss of high frequency detail. Each of the filter weights was divided by four so that the sum over all weights was equal to one. The application of the Wang filter results in the low-pass images being two rows and two columns shorter than the original image. To solve the computer hardware display problem of the reduced image size, the pixel values at the border of the filtered image were duplicated, and the duplicated pixel values added to the rows and columns of the filtered image. With the addition of two rows and two columns, the filtered image is the same size as the original image. Since the dynamical processes of interest were near the centre of the image, the artificial image extension at the borders did not introduce spurious information.

$$\begin{matrix}
 0.25 & 0.50 & 0.25 \\
 0.50 & 1.00 & 0.50 \\
 0.25 & 0.50 & 0.25
 \end{matrix} \tag{3.1}$$

Following cloud-screening and low-pass filtering, an edge detector was applied to the July image sequence. There are numerous edge detectors available, but the Sobel edge detector was used. According to Pratt (1991), the Sobel edge detector is more sensitive to diagonal edges than to horizontal and vertical edges, and the Sobel routine provides the most linear response when comparing the detected edge angle to the actual orientation of the edge. The 3x3 Sobel edge detector has the form,

$$G(j,k) = \left\{ [G_R(j,k)]^2 + [G_c(j,k)]^2 \right\}^{1/2} \quad (3.2a)$$

$$G_R(j,k) = \frac{1}{K+2} [(A_2 + KA_3 + A_4) - (A_0 + KA_7 + A_6)] \quad (3.2b)$$

$$G_c(j,k) = \frac{1}{K+2} [(A_0 + KA_1 + A_2) - (A_6 + KA_5 + A_4)] \quad (3.2c)$$

where $K = 2$, and the pixel-numbering convention ($A_0 - A_7$) is given by (3.3).

$$\begin{array}{ccc} A_0 & A_1 & A_2 \\ A_7 & G(j,k) & A_3 \\ A_6 & A_5 & A_4 \end{array} \quad (3.3)$$

The motivation for the $K = 2$ weighting is to give equal importance to each pixel in terms of its contribution to the spatial gradient. In most of the imagery, the SST gradients were sharp enough so that the distinction between the cold, upwelled water, and the warmer shelf and offshore waters was readily apparent; however, the Sobel edge detector was effective at delineating temperature fronts when the SST gradients were not as sharp. The application of the Sobel edge detector to the SST imagery also provided an objective method to measure the spatial location of a temperature front: the sharper the SST gradient, the more robust the Sobel edge detector response.

3.3.2 Sea Surface Temperature Transects

Transects of the digitized data were taken perpendicular and parallel to Vancouver Island. The perpendicular (across-shore) transects were taken at five locations (see Figure 3.5): Kains Island, Brooks Peninsula, Tatchu Point, Estevan Point, and Cox Point. Each cross-shore transect was approximately 110 km in length and the geographic location was selected to coincide with hydrographic lines that the Institute of Ocean Sciences routinely samples. The parallel (long-shore) transects were taken to roughly line up with the 100, 200, 1000, and 2000 m isobaths along Vancouver Island and were about 300 km in length. The satellite images were sampled using a bilinear interpolation algorithm developed by Thomas (1987) that translates latitude and longitude into an (x,y) location, and relates the (x,y) location to pixel co-ordinates in the image matrix. The algorithm is given by,

$$T(x,y) = dydxP_1 + dy(1-dx)P_2 + dx(1-dy)P_3 + (1-dx)(1-dy)P_4 \quad (3.4)$$

$T(x,y)$ is the temperature, P_{1-4} are the satellite temperatures of the four pixels nearest the (x,y) location, and dx and dy are the differences between their pixel co-ordinate in the image matrix and the (x,y) location.

Although the satellite imagery was essentially cloud-free, there were some patches of cloud, and due to satellite data reception errors, dropout (a lost scan line) would sometimes occur. Both of these conditions would produce a spike in the SST transects (clouds and dropout were given a pixel value of zero). Spikes in the transect data were corrected by interpolating the temperature across the spike by looking at the temperature before and after the spike. In the along-shore direction, a maximum of five contaminated pixels were corrected within a 50 km distance, and in the cross-shore direction, a maximum of three contaminated pixels were corrected within a 25 km distance.

The values of five and three pixels were subjectively selected, and the 50 and 25 km distances are the along-shore and across-shore coherence scale along Vancouver Island as suggested by Thomson (1984); however, the quality of the data was such that the interpolation distance guideline was never exceeded.

3.4 Hydrographic, Wind, and Bakun Upwelling Index Data

Hydrographic data were obtained from the Ocean Physics Group at the Institute of Ocean Sciences (IOS); cruise 84-13 was from July 23 to July 26, 1984 and the end of the satellite data sequence overlapped with the beginning of the 84-13 cruise. The 84-13 cruise (Figure 3.5), was only in the southern end of Vancouver Island with sampling from the Strait of Juan de Fuca to Line G, at Estevan Point. At each station, measurements of temperature, salinity, sigma-t, and geopotential anomaly as a function of the pressure were obtained (Thomson et al., 1986). There were also subsurface current measurements from a depth of 30 m taken at station E2 (off Estevan Point) and in addition, continuous measurements of the temperature at 30 m depth for station E2, and at 5 m depth at station T3 (off Cox Point) were also obtained.

The Atmospheric Environmental Service (AES) maintains climatological stations along the west coast of Vancouver Island that measure wind speed and direction either hourly or every three hours. Wind data were obtained from June through September, 1984, from two locations: Cape Scott, at the northern end of Vancouver Island, and Estevan Point, further south (see Figure 3.5). The wind data were averaged in 6-hour bins and rotated 30° from the north to produce cross-shore and long-shore components of the wind speed. In addition, daily point measurements of the sea surface temperature and the sea surface salinity were obtained from the Amphitrite Point Lightstation; similar temperature and salinity values were also obtained from the Kains Island Lightstation.

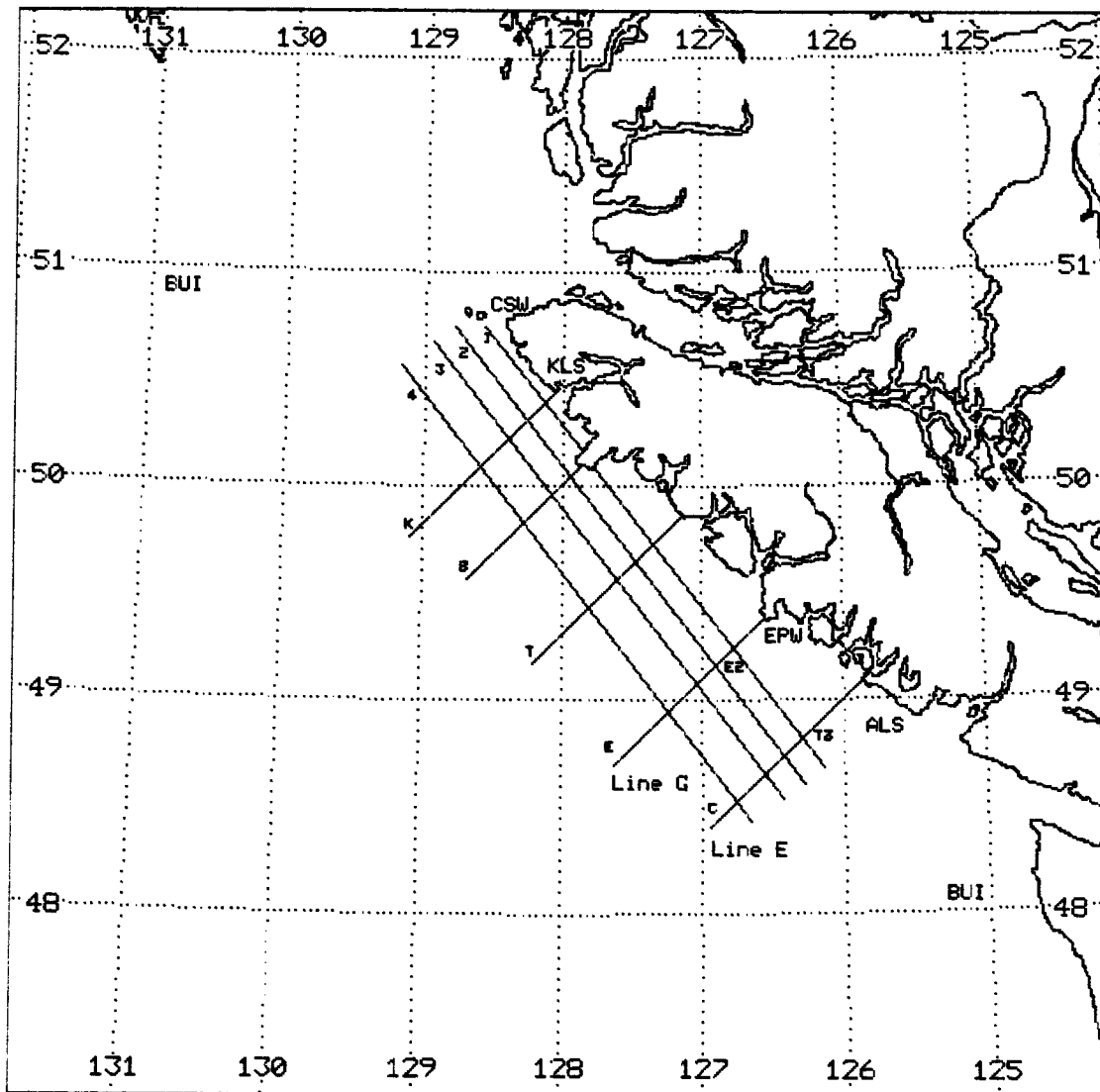


Figure 3.5. Map showing the location of: SST transects: Cross-shore (K=Kains Is., B=Brooks Peninsula, T=Tatchu Pt., E=Estevan Pt., C=Cox Pt.) and Longshore (1=100 m isobath, 2=200 m isobath, 3=1000 m isobath, 4=2000 m isobath); CTD lines: (Line G-Estevan Pt., Line E-Cox Pt.); Current meters (E2 and T3); Coastal wind stations: (CSW=Cape Scott, EPW=Estevan Pt.); Lighthouse stations (KLS=Kains Is., ALS=Amphitrite Pt.); Bakun Upwelling Index (BUI) at 51°N,131°W and 48°N,125°W.

The Bakun Upwelling Index (BUI) is based on estimating the wind stress on the sea surface at various points along a coastline. According to Bakun (1973), the stress is calculated according to the classical relation involving the square of the wind speed (4.1); the wind speeds are estimated for 3-degree latitude-longitude grids based on 6-hourly objectively analyzed synoptic pressure field. The Ekman transport is calculated from the wind stress, and the component of the transport perpendicular to the coastline is taken as an indication of the amount of water upwelled through the Ekman layer to replace the water that is driven offshore. Positive values of the Index indicate upwelling and negative values indicate downwelling. Daily BUI values were obtained for two positions: one was at 48° N latitude and 125° W longitude, just south of Vancouver Island, and the other BUI value was obtained for 51° N latitude and 131° W longitude, northwest of Vancouver Island.

3.5 Summary

Fifteen AVHRR satellite images were obtained from the UBC SOMeL archive. The images were navigated and calibrated to produce an image that was 512x512 pixels with a resolution 1.1 km per pixel. After navigation, the images were nudged which reduced the navigation error to about 2 km. The AVHRR channel 4 images were calibrated to produce temperatures between 0 and 25.5° C. Calibration errors result in a relative temperature uncertainty (image to image comparison) of about 0.5° C, and atmospheric effects can introduce errors in the 1.0 to 1.5° C range when comparing satellite sensed measurements of the temperature to *in situ* temperature measurements (Stewart, 1985). The satellite-derived SST and the *in situ* temperatures were well correlated in the upper few meters of the water column, but the correlation decreased for depths greater than approximately 3 m.

Hydrographic data were obtained that gave measurements of temperature, salinity, sigma-t, and the geopotential anomaly. The data from a subsurface current moorings were also available, and in addition, the subsurface moorings also provided continuous

measurements of the temperature at a depth of 30 m and 5 m. Hourly and 3-hourly wind data were obtained from two climatological stations along the west coast of Vancouver Island, and two lightstations provided daily measurements of the sea surface temperature and the sea surface salinity. Bakun Upwelling Index values were available from two locations that were north and south of Vancouver Island.

CHAPTER 4

UPWELLING THEORY

4.1 Basic Two-layer Theory

4.1.1 Coastal Transport

When the wind blows over the ocean, there is a vertical flux of horizontal momentum into the ocean surface. The mean rate of momentum transfer to the ocean surface is equal to the wind stress τ ,

$$\tau = C_D \rho u^2 \quad (4.1)$$

where ρ is the density of the atmosphere, u is the wind speed (usually taken at 10 m above the surface), and C_D is the drag coefficient. According to Gill (1982), the drag coefficient increases with wind speed, and for low wind speeds, C_D has a value of about 1.1×10^{-3} . For wind speeds between 6 m/s and 22 m/s, a commonly used version of the drag coefficient is given by Smith (1980), and has the form shown in (4.2).

$$C_D = (0.61 + 0.063u) \times 10^{-3} \quad (4.2)$$

Due to the Coriolis force, the wind stress at the ocean surface forces a surface current that is directed to the right (Northern Hemisphere) of the wind stress. The surface current rotates continuously with depth, while decaying exponentially with a scale of order 10 to 20 m (Apel, 1987); the decay scale depth, which is referred to as the Ekman surface layer, is the region of the water column where the applied wind stress is absorbed. The end result of the vertical transfer of momentum to the Ekman surface layer is that the net, depth-integrated transport is directed 90° to the right of the wind stress direction. When a wind blows with a coastline to the left of the wind direction, the effect of the depth-integrated transport directed perpendicularly to the coastline is that upwelling occurs to replace the water that is advected offshore in the Ekman surface layer.

Huyer (1983) comments that in addition to the Ekman surface layer, the idealized vertical structure of the water column also has an Ekman bottom layer and an interior region (Figure 4.1). The Ekman bottom layer is comparable in thickness to the surface Ekman layer. Between the surface and the bottom layers is the interior region, and in this region, the pressure gradient balances the Coriolis force and the flow is assumed to be geostrophic. In the open ocean, the geostrophic interior occupies most of the water column, but closer to shore the Ekman layers occupy a significant fraction of the water column. Huyer continues by saying that during an upwelling event, most of the onshore flow is through the geostrophic interior and the flow in the bottom layer is relatively weak.

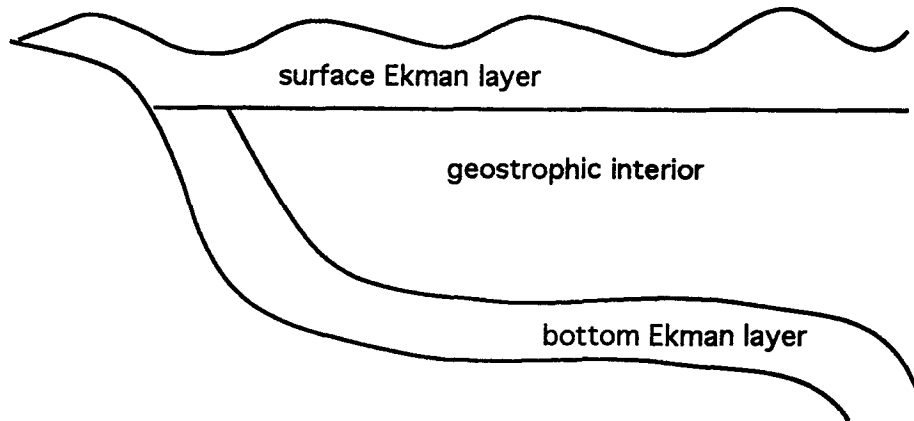


Figure 4.1. Schematic diagram of the coastal upwelling regime showing the Ekman layers and the geostrophic interior.

4.1.2 Two-layer Flow

Although the distributions of water properties such as density and temperature is continuous in the ocean, it is computationally easier to divide the ocean into layers, and each layer is assumed to represent the variation of the vertical structure of the water column. A two-layer model is the simplest approach and the minimum number of layers required to represent the first baroclinic, or internal mode. The baroclinic mode is defined as a flow for which the isobars and the isopycnals are not parallel, and in theory there are an infinite number of baroclinic modes. The two-layer model also represents the barotropic, or external mode, and unlike the baroclinic mode, the barotropic mode is a flow for which the isobars and the isopycnals are parallel. Although a two-layer model contains only two vertical modes, LeBlond and Mysak (1977) comment that for long-period hydrostatic motion, most of the energy is usually confined to the first two modes.

The easiest way to take into account the vertical variation of density, which is a feature of any upwelling event, is to use a two-layer model. The top layer depth is selected to represent the density values in the mixed layer, and the bottom layer depth represents the density value for the deep ocean; the density in each layer is assumed to be constant. Along Vancouver Island, the mixed layer depth is typically in the upper 200 m (Thomson, 1984). Figure 4.2 shows the notation used for the two-layer model, and the development essentially follows Gill (1982).

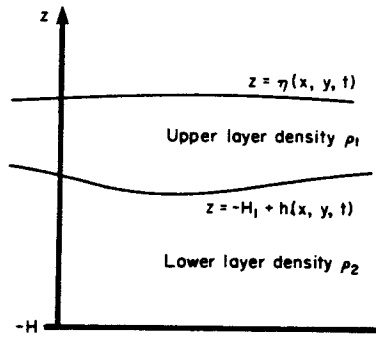


Figure 4.2. The notation used to describe the constant depth, two-layer model. From Gill (1982)

The upper layer density is ρ_1 , and u_1 and v_1 are the horizontal velocity components. H_1 is the depth of the upper layer while at rest, and $z=\eta(x,y,t)$ is the surface elevation. Similarly, ρ_2 , u_2 , v_2 , H_2 , and $z=-H_1+h(x,y,t)$ are the values for the lower layer, with $H=H_1+H_2$, the total depth. In the upper layer, the linear shallow water equations with wind forcing are,

$$\frac{\partial u_1}{\partial t_{(I)}} - fv_{1(II)} = -g \frac{\partial \eta}{\partial x_{(III)}} + \frac{\tau_x}{\rho_1 H_{1(IV)}} \quad (4.3a)$$

$$\frac{\partial v_1}{\partial t_{(I)}} + fu_{1(II)} = -g \frac{\partial \eta}{\partial y_{(III)}} + \frac{\tau_y}{\rho_1 H_1} \quad (4.3b)$$

and for the lower layer, the equations have the form,

$$\frac{\partial u_2}{\partial t_{(I)}} - fv_{2(II)} = -g \frac{\partial \eta}{\partial x_{(III)}} - g' \frac{\partial h}{\partial x_{(V)}} \quad (4.4a)$$

$$\frac{\partial v_2}{\partial t_{(I)}} + fu_{2(II)} = -g \frac{\partial \eta}{\partial y_{(III)}} - g' \frac{\partial h}{\partial y_{(V)}} \quad (4.4b)$$

Terms (I) are the local time rate of change of the velocity components, or the Eulerian velocities. Term (II) represent the effects of the Coriolis force, where f is the Coriolis parameter. Terms (III) are the horizontal pressure gradients which by use of the hydrostatic approximation are written in terms of the free surface perturbation, η , and g is the acceleration due to gravity. Terms (V) are the same as terms (III) except that h is the interface displacement between the two fluid layers, and g' is the reduced gravity, which as the form,

$$g' = g(\rho_2 - \rho_1) / \rho_2 \quad (4.5)$$

Terms (IV) represent the surface stress imposed by the wind, and are the pathways by which horizontal momentum is transferred into the water column.

In the upper and bottom layers, the continuity equations have the form,

$$\frac{\partial(\eta + H_1 - h)}{\partial t_{(I)}} + H_1 \left(\frac{\partial u_1}{\partial x} + \frac{\partial v_1}{\partial y} \right)_{(II)} = 0 \quad (4.6a)$$

$$\frac{\partial(h)}{\partial t_{(I)}} + H_2 \left(\frac{\partial u_2}{\partial x} + \frac{\partial v_2}{\partial y} \right)_{(II)} = 0 \quad (4.6b)$$

The continuity equations indicate that for terms (II), the divergence of the horizontal transport will cause a downward displacement of the free surface and an upward displacement of the interface between the two layers, terms (I).

The derivation of the linear shallow water equations includes the f-plane, the hydrostatic, and the Boussinesq approximations. Additional details on the derivation are outlined in Gill (1987), Pedlosky (1987), and LeBlond and Mysak (1977). For large-scale ocean flows, the Coriolis parameter, $f=2\Omega\sin\theta$, varies with latitude. However, the variation of f is only important for oceanic events of very long time scale (a few weeks), or very long length scales (thousands of kilometers); otherwise, f can be assumed to remain essentially uniform (Kundu, 1990). When the horizontal velocities are large compared to the vertical velocities, and the scales of horizontal motions greater than the depth, then the pressure perturbation is independent of depth, and the pressure can be calculated using the hydrostatic equation which assumes a static fluid, hence the hydrostatic approximation. The Boussinesq approximation as outlined by Pond and Pickard (1983), assumes that if the density variations are small, then their effect on the mass of the fluid can be neglected, but their effect on the weight of the fluid must be considered. In other words, the average density over a region can be used in the horizontal direction, but for the vertical direction, the in situ density must be used to calculate the pressure field.

For the baroclinic mode, the free surface displacements are smaller than the interface displacements, and the rigid lid approximation can be made which allows (4.6a) to be written as,

$$\frac{\partial(-h)}{\partial t_{(I)}} + H_1 \left(\frac{\partial u_1}{\partial x} + \frac{\partial v_1}{\partial y} \right)_{(II)} = 0 \quad (4.7)$$

The velocity difference between the two layers can be obtained by subtracting (4.4) from (4.3) to obtain,

$$\frac{\partial \hat{u}}{\partial t} - f \hat{v} = g' \frac{\partial h}{\partial x} + \frac{\tau_x}{\rho_1 H_1} \quad (4.8a)$$

$$\frac{\partial \hat{v}}{\partial t} + f \hat{u} = g' \frac{\partial h}{\partial y} + \frac{\tau_y}{\rho_1 H_1} \quad (4.8b)$$

and the continuity equation is written as,

$$-\left(\frac{1}{H_1} + \frac{1}{H_2} \right) \frac{\partial h}{\partial t} + \frac{\partial \hat{u}}{\partial t} + \frac{\partial \hat{v}}{\partial t} = 0 \quad (4.9)$$

where,

$$\hat{u} = u_1 - u_2; \hat{v} = v_1 - v_2 \quad (4.10)$$

Now consider the special case when there are no variations in the along-shore direction, $\partial/\partial x \rightarrow 0$, a vertical wall that corresponds to the coastline at $y = 0$, a constant

depth, and the wind stress τ_x is constant and $\tau_y = 0$. Then (4.8) and (4.9) can be combined into a forced shallow water equation with a solution of the form,

$$\hat{v} = \left(\frac{\tau_x}{\rho f H_1} \right) \left(1 - \exp\left(\frac{-y}{a}\right) \right) \quad (4.11a)$$

$$h = \left(\frac{c \tau_x}{\rho g' H_1} \right) \left(\exp\left(\frac{-y}{a}\right) \right) t \quad (4.11b)$$

$$\hat{u} = \left(\frac{\tau_x}{\rho H_1} \right) \left(\exp\left(\frac{-y}{a}\right) \right) t \quad (4.11c)$$

where c is the speed of a long internal wave and is given by,

$$c^2 = \frac{g' H_1 H_2}{(H_1 + H_2)} \quad (4.12)$$

and $a = c/f$ is the Rossby radius of deformation. Pedlosky's (1974) comments that the Rossby radius is the key offshore scale, which is verified by the appearance of the Rossby radius in the horizontal velocities and the upwelling rate in (4.11). For the case of an eastern boundary, the graphical solution of (4.11) is shown in Figure 4.3. Subsurface water is upwelled to replace the surface water that is advected offshore due to the Ekman transport. In the upper layer, a coastal jet is formed that flows equatorward and intensifies with time; the cross-shore scale of the upwelling response is given by the internal Rossby radius of deformation. In the lower layer, a poleward countercurrent is formed that usually flows in the opposite direction to the wind.

In a study by Allen (1973), upwelling and coastal jets were investigated for a continuously stratified ocean that had the same coastline geometry as the two-layer model. The results were similar to those obtained by the two-layer model, and Allen noted that the coastal jet formed in response to an increase in the along-shore winds, and the formation time scale was on the order of a few days. As with the two-layer case, the coastal jet was in geostrophic balance such that the vertical velocity shear in the jet was related to the across-shore density gradient by the thermal wind relationship.

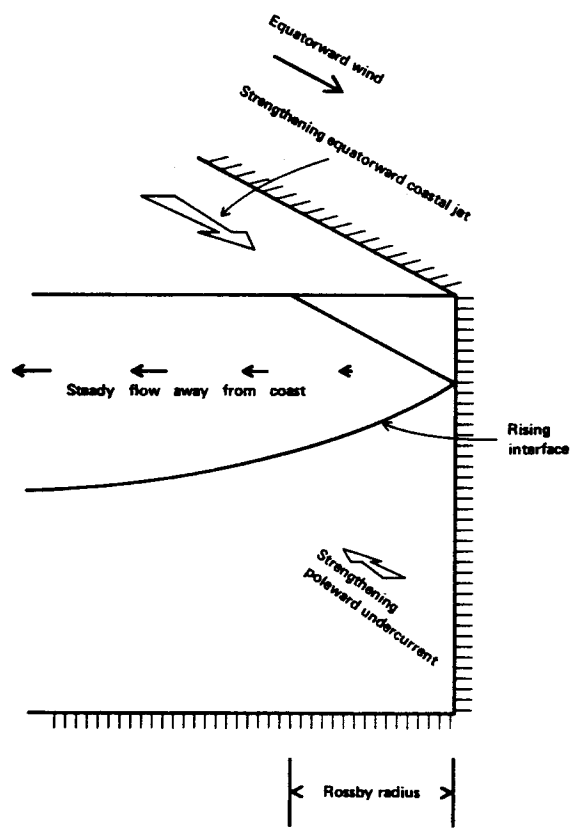


Figure 4.3. The upwelling solution for an eastern boundary. From Gill (1982)

4.2 Shelf Break Effects

4.2.1 Observations

In the previous section, a two-layer model of coastal upwelling was discussed. Since the depth was constant, topographic variations in the form of a shelf break that represent a more realistic coastline could not be included. The presence of the shelf break does not significantly change the salient features of the upwelling response (Csanady, 1982), but it does introduce the possibility of the occurrence of shelf break upwelling and the formation of a shelf break jet. Both the shelf break upwelling and the shelf break jet are similar in structure, but generally weaker in magnitude than their coastal counterparts; however, these events frequently occur and they are observed in most upwelling regions.

Off Vancouver Island, Ikeda and Emery (1984) observed a band of cold water that remained roughly centered along the shelf break during an upwelling event. Along the northwest African shelf, Barton et al. (1977) observed cold water that appeared over the shelf and gradually migrated to the shelf break. Despite the persistence of upwelling favourable winds, Barton commented that the cold water remained along the shelf break until the winds weakened. Although the presence of cold water along the shelf break was thought to be due to shelf break upwelling in each of the previous studies, both authors point out that the cold water may not be due to upwelling, but may result from water that is advected from other regions further upstream.

Further observations of shelf break upwelling were noted by Dickson et al. (1980) who used AVHRR image of the Celtic Sea to investigate a narrow ribbon of cold water that was aligned along the top of the continental slope; transects across the shelf break show

warmer water on either side of slope water thus suggesting that shelf break upwelling was occurring. Petrie (1983) studied the current response to transient wind forcing at the shelf break off Nova Scotia. He observed that at the onset of upwelling favorable winds, upwelling occurs at the shelf break prior to the appearance of upwelled water on the shelf, and the shelf break upwelling was confined within the Rossby radius of the break. In addition, Petrie commented that strong long-shore currents with large vertical shears were also confined to the shelf break area.

4.2.2 Upwelling and Jets

Analytical and numerical models have been developed to try and explain the observations of shelf break upwelling and the formation of jets along the shelf break. As a minimum requirement, the models must incorporate a variation of topography to allow for the change of depth that usually begins at the shelf break and extends down the continental slope. In addition, the models should include variability of the flow that is driven by the wind stress, and stratification to incorporate the characteristic bending of the isopycnals and isotherms at the shelf break and the coastline during an upwelling event. In the observations of shelf break upwelling mentioned previously, the upwelling at the shelf break was related to long-shore winds that setup the classical two-layer, constant depth upwelling circulation pattern that had water moving onshore in the interior and bottom layer to replace the offshore transport in the surface layer; however, the upwelling flow pattern is modified in the presence of variable topography.

When topographic variations in the form of a shelf break are introduced, Hill and Johnson (1974) suggest that a shear layer is formed above the shelf break, and the main purpose of the shear layer is to smooth out the discontinuity in the long-shore velocity that exists on either side of the shelf break. Associated with the discontinuity in the velocity is

the production of vertical motions that lead to upwelling into the surface Ekman layer. Johnson and Nurser (1984) investigated shelf break upwelling by looking at the effect of varying the topography on both sides of the shelf break. They suggest that the amount of upwelling at the shelf break depends on the slopes α_L and α_R , Figure 4.4.

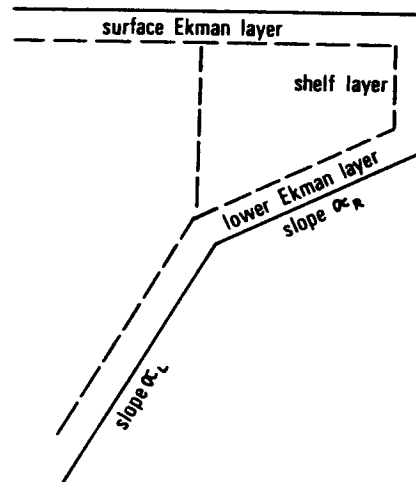


Figure 4.4. The shelf region with variable topography on both sides of the shelf break. From Johnson and Nurser (1984)

If $\alpha_L = \alpha_R$ (e.g. constant depth case), then there is no upwelling at the shelf break, but if α_L is greater than α_R (e.g. Hill and Johnson, 1974), there is a moderate amount of upwelling at the shelf break. As α_L becomes very much greater than α_R , the shelf break upwelling approaches a maximum, and strong currents develop along the shelf.

Using a two-layer model, Csanady (1973) investigated the forced response of a suddenly imposed long-shore wind. An equivalent depth scheme was used to smooth out the bottom topography, and the key result of Csanady's study was the development of a long-shore jet; the jet was centered along the shelf break and the jet velocity increased linearly with time. O'Brien and Hurlburt (1972) developed a two-layer numerical model that incorporated a shelf break. Their results indicate that in addition to coastal upwelling, there was secondary upwelling at the shelf break which was accompanied by a long-shore jet in the upper layer; in agreement with other studies, the upwelling and the jet were weaker than their coastal analogs. Using potential vorticity arguments, O'Brien and Hurlburt comment that the upwelling region and the jet will have the same width scale.

4.3 Summary

In the Northern Hemisphere, when the wind blows with the coastline to the left of the wind direction, the wind stress will drive an equatorward long-shore current, but the Coriolis force will cause the net, depth-integrated transport to be directed perpendicular to the coastline. In the case of two-layer, constant depth model, the offshore Ekman transport in the upper layer is balanced by return flow through the lower layer. The presence of the coastline causes a one-sided divergence situation, and the lower layer water is upwelled to replace the water that is advected offshore. The Ekman transport sets up an offshore pressure gradient which cause the formation of a baroclinic coastal jet; both the upwelling region and the jet have the same horizontal width scale that is given by the internal Rossby radius of deformation.

Based on theoretical studies and observations, shelf break upwelling and the formation of shelf-break jets are due to a change of the bottom topography at the shelf break. In the case of shelf break upwelling, vertical velocities are generated in the vicinity of the break which forces cold, subsurface water to the surface Ekman layer. The upwelled

water is confined to the shelf break region with the horizontal width scale given by the internal Rossby radius of deformation, which is typically on order of 10 to 40 km for most coastal regions. In concert with the shelf break upwelling, a shelf break jet can form which will have peak velocities in the area that corresponds to reasonably rapid changes in the bottom topography. As is the case for the upwelled water at the shelf break, the horizontal width scale of the jet is also controlled by the internal Rossby radius. The jet is assumed to be in geostrophic balance with the cross-shore pressure gradient, which implies that vertical shear in the jet is related to the cross-shore density gradient; the jet is also confined to the oceanic surface layer. Shelf break upwelling and shelf break jet formation are a common occurrence, and they are observed in most upwelling regions.

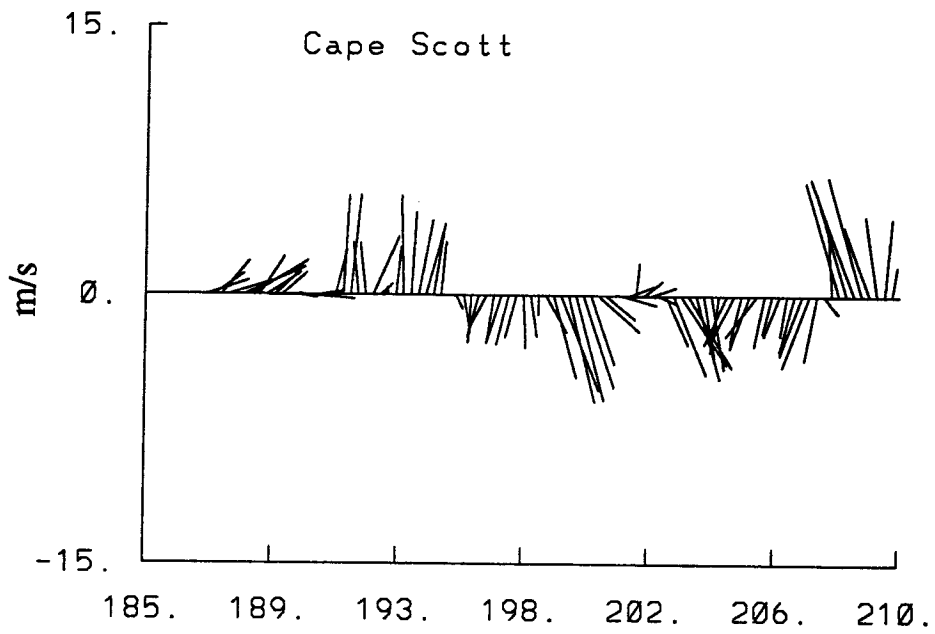
CHAPTER 5

UPWELLING EVENT: OBSERVATIONS AND ANALYSIS

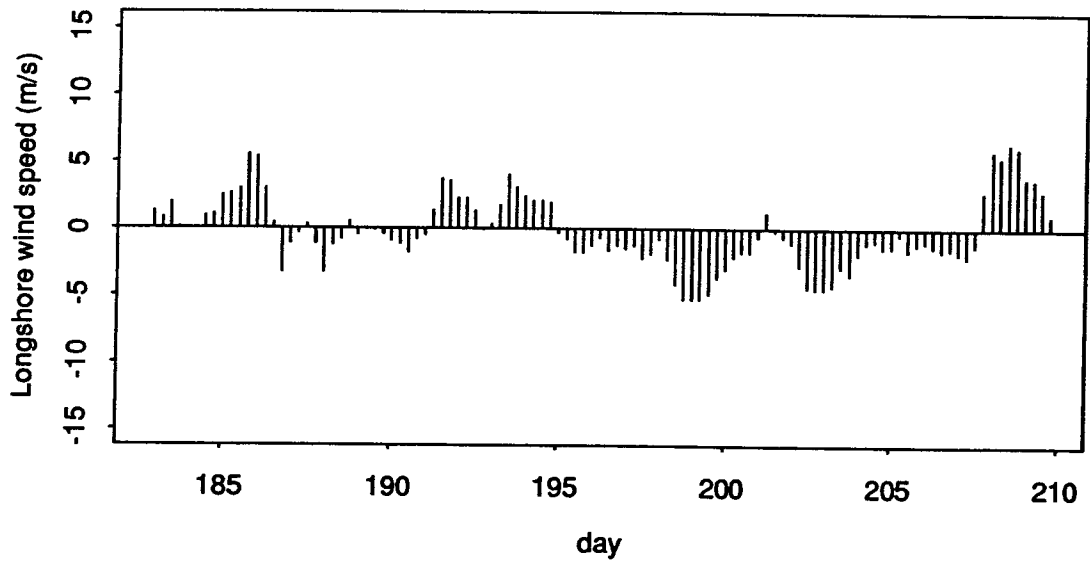
5.1 Wind and Coastal Temperatures

Wind speed and direction were obtained from two climatological stations along Vancouver Island: Cape Scott, at the northern end, and Estevan Point, toward the southern end (see Figure 3.5). The Cape Scott station will be used to represent the wind conditions at the northern end of the Vancouver Island, and the Estevan station will represent the wind conditions at the southern end during the upwelling event. Wind data in the vicinity of Brooks Peninsula would have provided a more complete picture, but it was not until November 1984 that the Atmospheric Environmental Service installed an automated climatological station on Solander Island, at the tip of Brooks Peninsula.

Figure 5.1a shows the wind at Cape Scott. The upward vertical direction is to the north, and the y-axis is the wind speed in m/s with the x-axis indicating the day-number for 1984; day 1 corresponds to January 1, and December 31 corresponds to day 366 (1984 was a leap year). The same day-number convention will be used for all time-based plots unless otherwise indicated. Prior to the upwelling event, the winds were generally from a southeasterly direction. Around day 195 (July 13), the winds become upwelling favourable until nearly day 209 (July 27); however in the middle of the July 13 to July 27 time frame, there is a brief period, around day 203 (July 23) when the winds weaken. Shortly after day 209, the winds return to downwelling favourable conditions.



a



b

Figure 5.1. a) Cape Scott wind (unrotated) Cape Scott Long-shore wind (rotated 30° from north)

The long-shore component of the wind for Cape Scott is shown in Figure 5.1b. The upwelling favourable conditions between day 195 and day 209 are evident, and the weakening of the winds around day 203 can be clearly seen. The temperature response to the winds at Kains Island (to the south of Cape Scott) can be seen in the Kains Island lightstation temperature record shown in Figure 5.2. As the upwelling favourable winds increase at Cape Scott, there appears to be a one to two day lag in the corresponding drop in the temperature at Kains Island; peak winds occur around day 199 and minimum temperatures are near day 201. The weakening winds that follow show up in the temperature increase, and as the winds strengthen, there is the related drop in temperature, which reaches a secondary minimum around day 208.

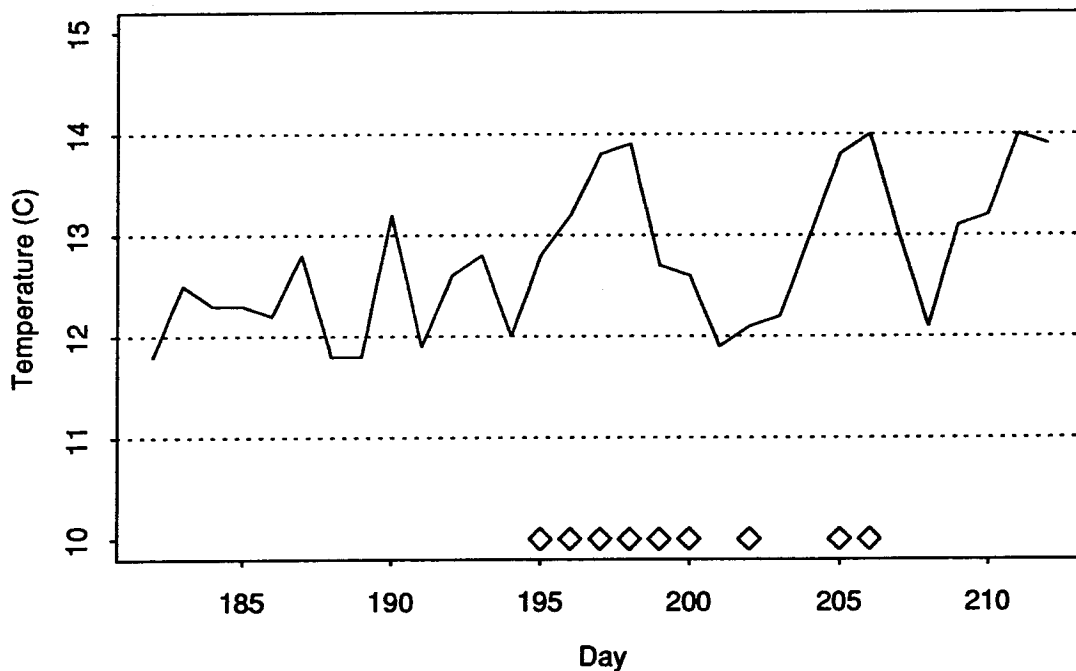
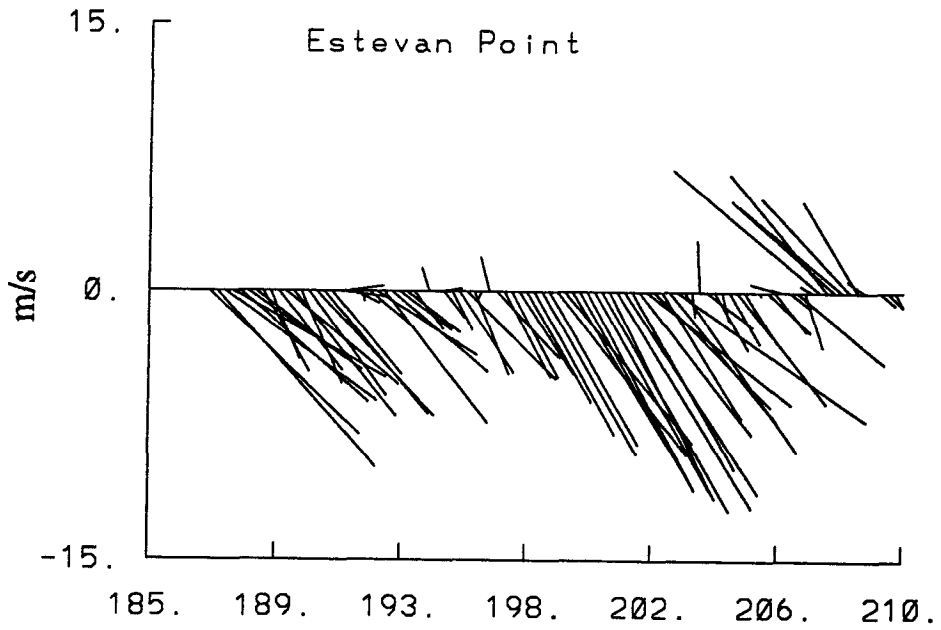


Figure 5.2. Kains Island lightstation temperature. The \diamond symbol indicates times when satellite data were available.

The Estevan Point winds are shown in Figure 5.3a. Upwelling favourable winds are apparent from around day 187 (July 5) through nearly day 210 (July 28), but from day 187 to day 195 (July 13), the winds get progressively weaker before increasing in strength again after day 195. The wind structure is easier to see in the Estevan Point long-shore wind component (Figure 5.3b). Prior to the AVHRR observed upwelling event, the winds are upwelling favourable, with speeds around 10 m/s. The winds subside and reach a minimum around July 13; a period of intense northwesterly winds follows and lasts for about eight days. The winds peak around day 200 (July 18), and dramatically reduce in strength around day 203 (July 21). Using (4.2) with the wind speed set to an average of 10 m/s, a C_D values of 1.24×10^{-3} is calculated, and if this C_D value is substituted into (4.1) with $\rho = 1.293 \text{ kg/m}^3$, an estimate of 0.16 N/m^2 is obtained for the wind stress at Estevan Point. A similar calculation for Cape Scott using an average of 2.5 m/s yields a wind stress estimate of 0.01 N/m^2 .

The temperature time series at the Amphitrite lightstation (south of Estevan Point) is shown in Figure 5.4. In response to the upwelling favourable winds, the temperature drops around day 190 (July 8) and fluctuates between 11° and 12° C , but the temperature gradually increases from day 190 through day 199 as the winds weaken. Around day 196 (July 14), the winds begin to increase in strength and reach a peak of nearly 12 m/s on day 200 (July 18). The temperature at Amphitrite begins to drop at day 199 and by the next day, the temperature is around 11° C . The temperature remains at 11° C until nearly day 203, but dramatically increases to over 14° C on day 206 (July 24) as the upwelling favourable winds weaken significantly.



a

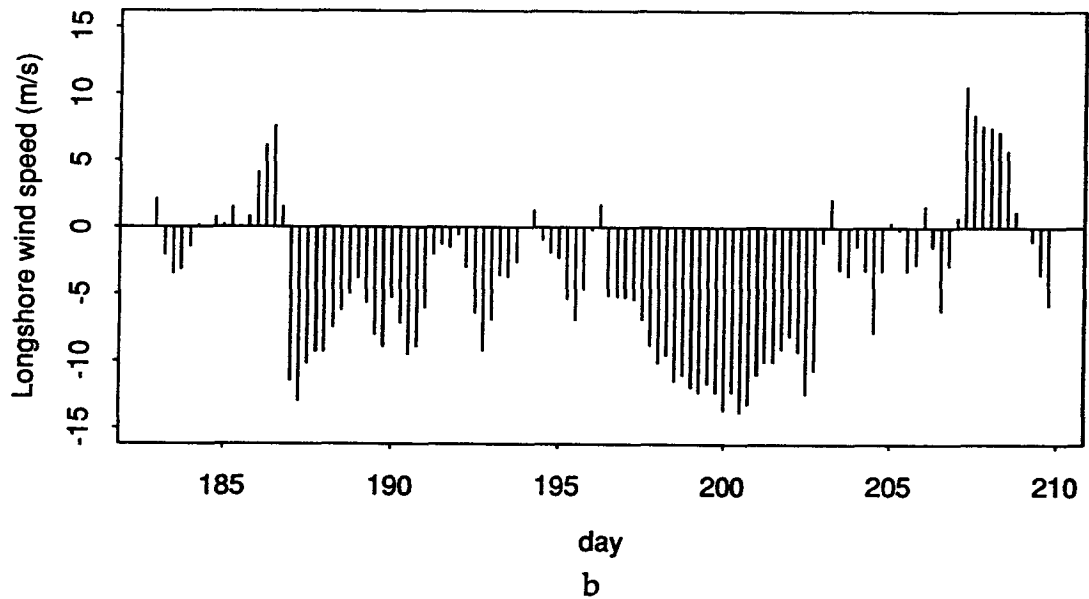


Figure 5.3. a) Estevan Point wind (unrotated) b) Estevan Point long-shore wind (rotated 30° from north)

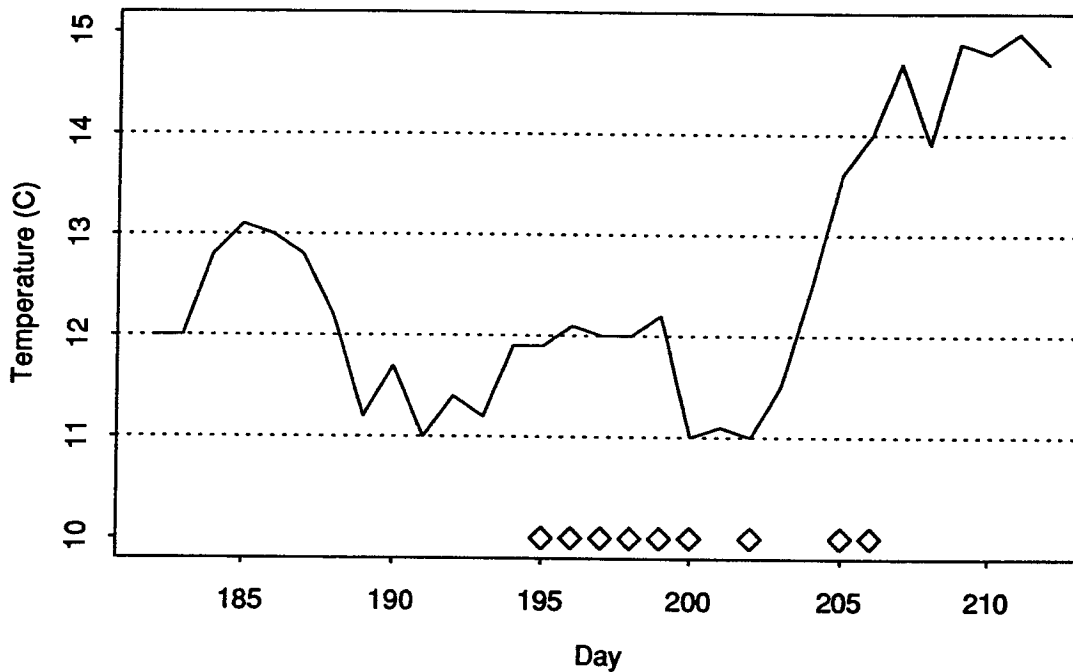


Figure 5.4. Amphitrite Point lightstation temperature. The \diamond symbol indicates times when satellite data were available.

Based on the coastal wind data and the temperature measurements at the Amphitrite Point and Kains Island lightstations, the temperature decrease at the lightstations is associated with an increase in the northwesterly winds. The wind data represents two sample points along Vancouver Island, but the wind measurements agree qualitatively with the wind regime along the entire west coast of Vancouver Island. Figure 5.5 shows the Bakun Upwelling Index for two positions: 51° N, 131° W, northwest of Vancouver Island, and 48° N, 125° W, south of Vancouver Island. The Bakun Index is calculated from a 3-degree latitude/longitude pressure field grid and measures the rate of upwelling or downwelling in $\text{m}^3 \text{sec}^{-1} (100\text{m})^{-1}$ of coastline. The variability of the Bakun Index at the

northern site (Figure 5.5a) agrees with the variability in the long-shore component (upwelling favourable) of the wind at Cape Scott: the amount of upwelling increases before and after day 200 (see Figure 5.1b). To the south (Figure 5.5b), the Bakun Index has an average value of about 40 from around day 190 through day 197. The Bakun Index increase dramatically and peaks at $134 \text{ m}^3 \text{ sec}^{-1} (100 \text{ m})^{-1}$ on day 200 (July 18), and then decreases to a value of about 25 on day 205 (July 23). The increase in the Bakun Upwelling Index agrees with the strengthening of the long-shore component (upwelling favourable) of the wind at Estevan Point (see Figure 5.3b).

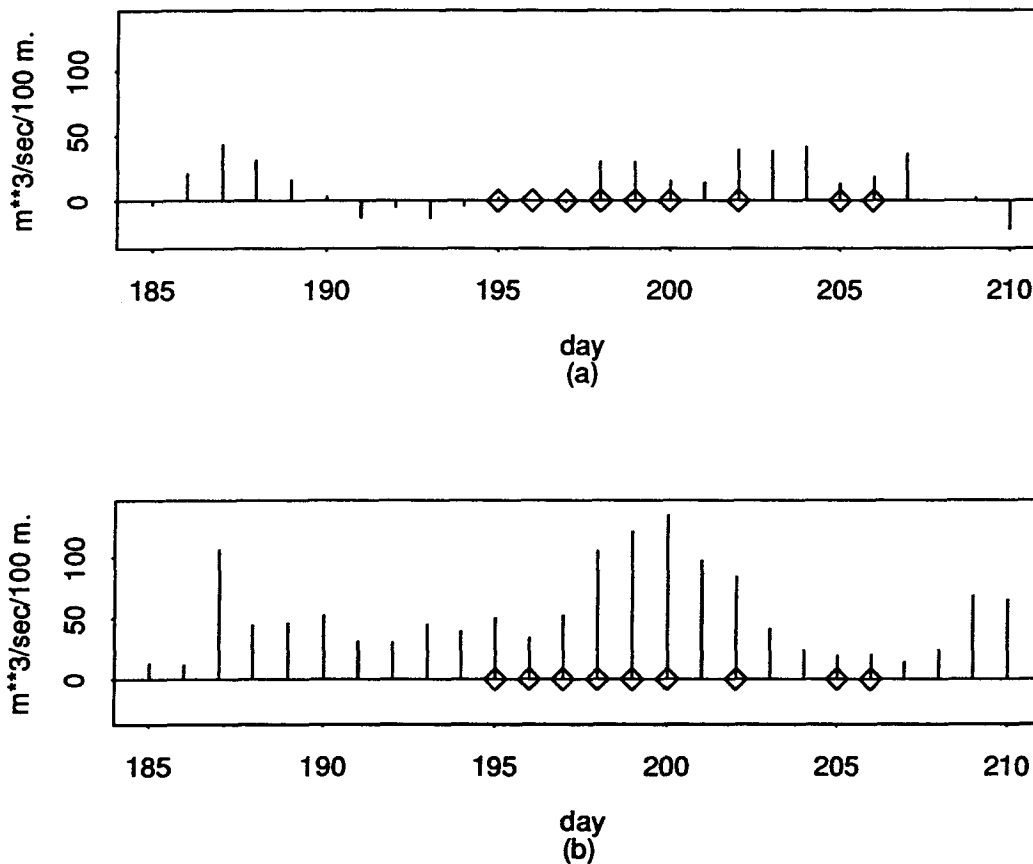


Figure 5.5. a) Bakun Upwelling Index ($51^\circ \text{ N}, 131^\circ \text{ W}$) b) Bakun Upwelling Index ($48^\circ \text{ N}, 125^\circ \text{ W}$)

5.2 AVHRR Observations

AVHRR imagery was available from July 13 to July 24 (see Table 3.2). Although there was typically a late afternoon and an early evening pass each day, only the temperature calibrated, channel 4 imagery from the late afternoon passes will be discussed. The exception to the late afternoon imagery will be for July 13, when only the early evening pass was available. As was shown in Figure 3.2, the near-surface temperature profile of the ocean varies depending on the time of day and the weather conditions; therefore, comparing imagery that was obtained at roughly the same time each day should yield more consistent results.

The AVHRR observations of the upwelling event will be divided into four stages. The observations will be mainly south of Brooks Peninsula, along the shelf, shelf break, and offshore waters. Stage 1 is from July 13 to July 15 (day 195 to 197), and deals mainly with the formation of cold water around Brooks Peninsula, and to a lesser extent, the cold water formation in the vicinity of Cape Scott. Stage 2, July 16 through July 17 (day 198 to 199) entails the period when the winds are increasing in strength and there appears to be an equatorward migration of cold water along the shelf break. Stage 3 occurs during the time when the winds are at their maximum strength, July 18 through July 20 (day 200 to 202), and there is evidence cold water over the entire shelf, and shelf break regions. Stage 4, July 23 to July 24 (day 205 to 206), is the relaxation period when the winds significantly reduce in strength and there is intense warming over the shelf region to the south of Brooks Peninsula, but a band of cold water persists along the shelf break.

5.2.1 Stage 1: July 13-15

The July 13 (day 195), n6.26231 image is shown in Figure 5.6a. The SST are reasonably consistent over the shelf and offshore waters (D), but there is some evidence of colder water along the coastline (A). (The letters correspond to the features on the AVHRR images, Table 5.1). There is also colder water in the vicinity of Brooks Peninsula (B), and Cape Scott (C); the appearance of cold water in these two regions has been observed in the AVHRR data from other years and usually indicates the pending start of an upwelling event. The cold water around Brooks Peninsula is perhaps due to enhanced upwelling that is related to variations in the local topography.

Letter Code	AVHRR Feature
A	coastal water
B	Brooks Peninsula
C	Cape Scott
D	offshore water
E	shelf break jet
F	filaments
G	La Perouse Bank
H	Juan de Fuca St.

Table 5.1. AVHRR image features. The letters are printed on the AVHRR satellite images and relate to the corresponding feature identified in the satellite imagery.

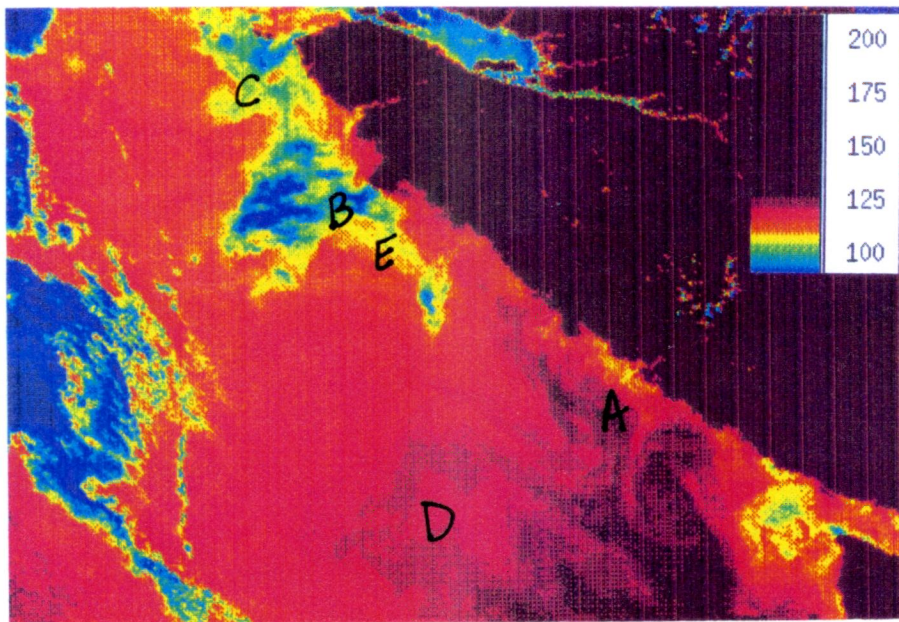
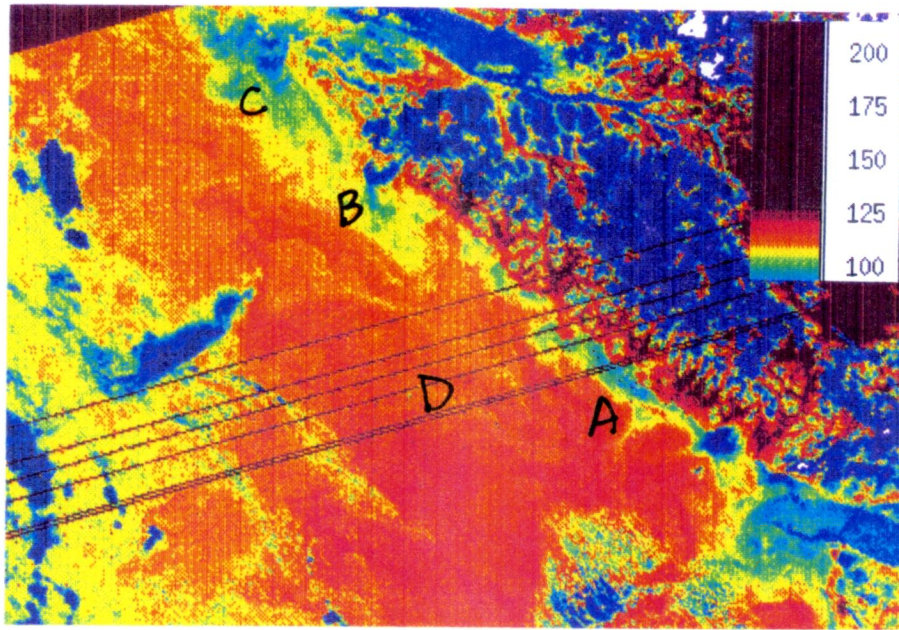


Figure 5.6. Stage 1 AVHRR imagery. a) July 13 (day 195) image, b) July 14 (day 196) image. The temperature scale ($\times 10^{-1}$) is shown in the upper right corner

The following day, July 14 (day 196), the n7.15779 image (Figure 5.6b) shows relatively warm offshore waters (D) with temperatures in the 13 to 14° C range. Along the coastline (A), there are isolated patches of colder water with temperatures that are typically around 11 to 12° C. Water in the 11 to 12° C range is also observed around Cape Scott (C) and Brooks Peninsula (B). In the vicinity of Brooks Peninsula there are patches of clouds that cause an apparent reduction in the sea surface temperature; however, the water at the tip of Brooks Peninsula is still colder than the water on either side of the Peninsula. Extending equatorward from Brooks Peninsula is the indication of a jet-like structure that is roughly centered along the shelf break; the jet-like structure will be referred to as the shelf-break jet. The jet, which will be defined to include surface water that is bounded by the 12° C isotherm, extends about 40 km to the south of Brooks Peninsula, but patches of cloud obscure the southern tip of the jet. (The 12°C isotherm was selected because it is common to all the AVHRR images, and it can be used as an indicator of the relative change in the long-shore SST structure during the upwelling event, but the actual core of the shelf-break jet is in the 10 to 11° C range.)

The July 15 (day 197), n7.15793 image is shown in Figure 5.6c. The southern offshore waters (D) have increased in temperature from the previous day and are now in the 14° to 15° C range, with temperatures exceeding 15° C in the extreme southern waters (bottom middle of Figure 5.6c). Along the coastline (A), there are isolated patches of colder water with a temperature range that is comparable to the previous day, but there is no indication of a uniform decrease in the sea surface temperature along the coastline. The shelf-break jet extends approximately 50 km equatorward from Brooks Peninsula with temperatures of 14° C on the shoreward and seaward side of the jet. Around Cape Scott (C), the sea surface temperatures are in the 12° to 13° C range and extend to the coastline.

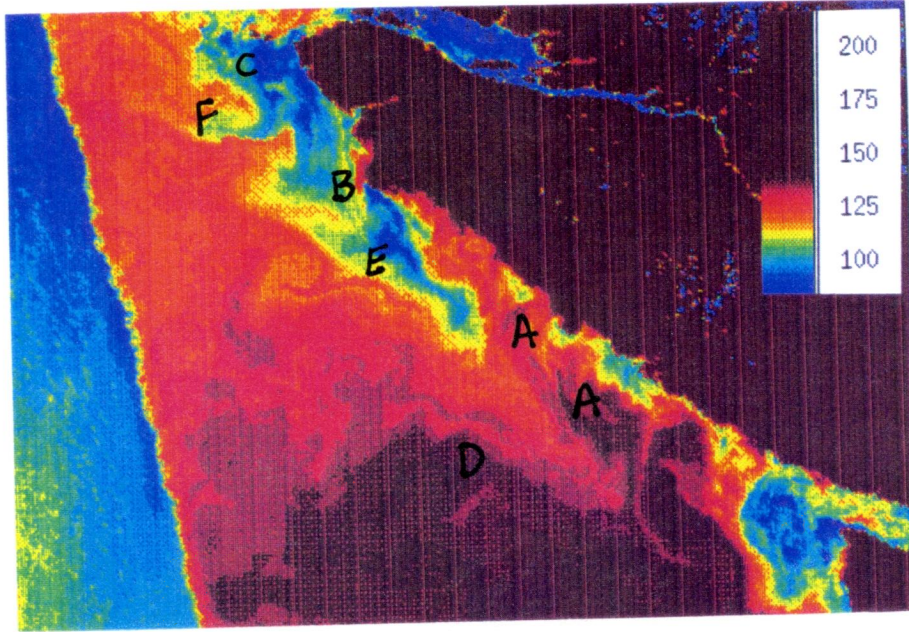


Figure 5.6. Stage 1 AVHRR imagery (con't). c) July 15 (day 197) image. The temperature scale ($\times 10^{-1}$) is shown in the upper right corner.

The cooler water along the coastline is in contrast to the band of warm water between the shelf break and the coastline, south of Brooks Peninsula. There is also evidence of frontal instability which can be seen in the wave-like sea surface temperature structure (F) between the cooler, coastal waters and the warmer, offshore waters.

Cross-shore SST transects were taken at Brooks Peninsula, Tatchu Point, Estevan Point, and Cox Point. Each transect is about 100 km, and except for stage 1, which does not include the July 13 image, the transects are the average temperatures over the imagery that entails each stage. The sharp increase in the transects that occasionally occurs at the coastline (see Figure 5.7b) is caused by navigation errors during image processing. Navigation errors can result in the image being slightly shifted relative to the transects, and when this happens, the transects sample land and water near the coastline. Since the land is considerable warmer than the water, when the temperature of the ocean and the land are averaged, an apparent increase in the SST occurs. Therefore, the SST minimum along the coastline will be taken a few kilometers from the shore to avoid the artificial temperature increase caused by the sampling errors.

The Brooks Peninsula (Figure 5.7a) transect indicates that the coldest water extends to slightly seaward of the shelf-break, and then the SST increases in the offshore direction. At Tatchu Point (Figure 5.7b), the SST is fairly consistent between 13° to 14° C, but there is evidence of the shelf-break jet that can be seen in the dip of the SST just seaward of the shelf-break. Moving to the south, Estevan Point and Cox Point (Figures 5.7c & 5.7d) show little variation in the cross-shore SST; the SST are essentially constant in the offshore waters, but the temperature decreases closer to the coastline. As previously mentioned, the temperature decrease could be due to local upwelling, or perhaps the decrease may be evidence of the poleward flowing Vancouver Island Coastal Current.

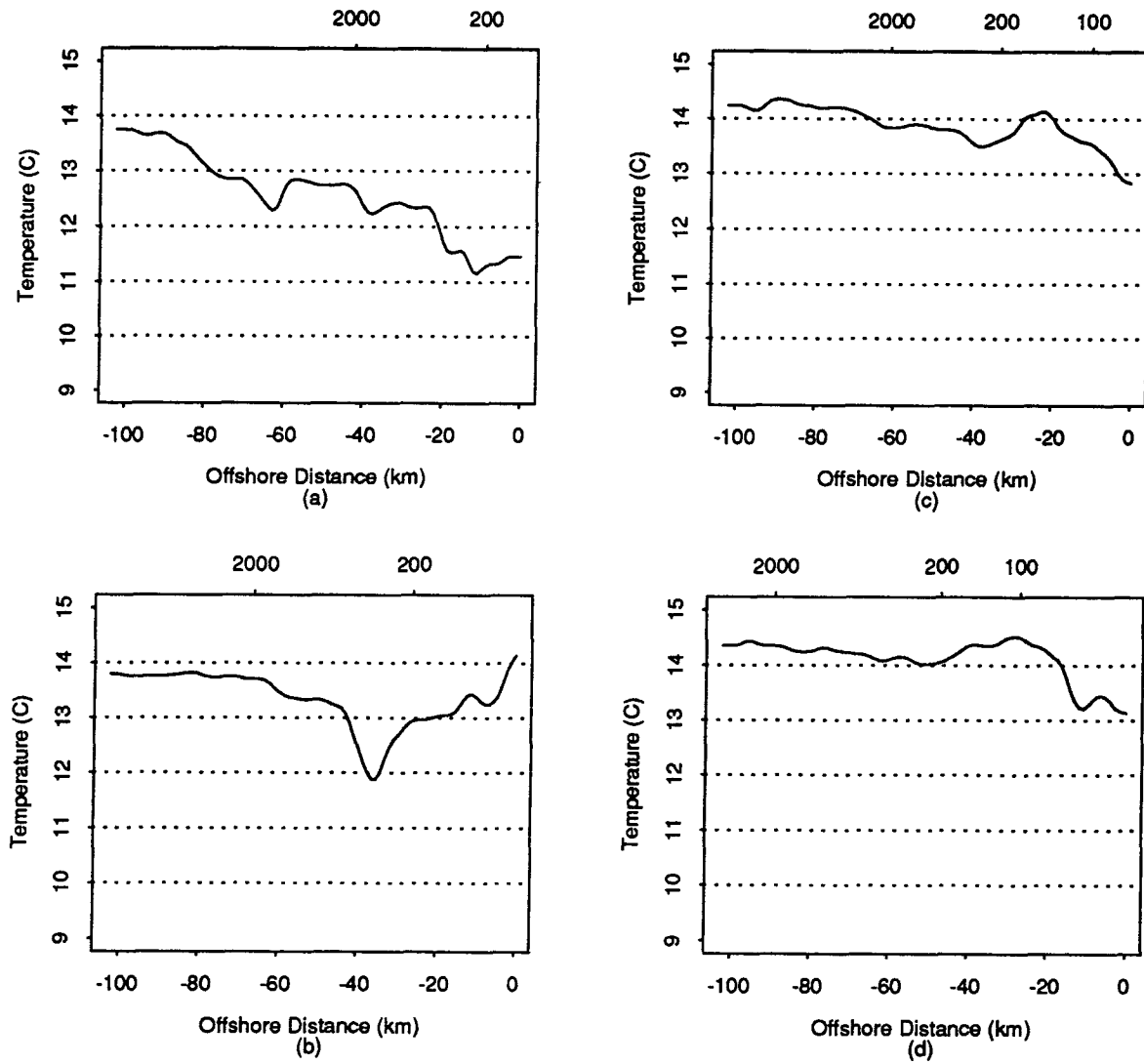


Figure 5.7. Stage 1 (day 195 to 197) cross-shore SST transects a) Brooks Peninsula b) Tatchu Point c) Estevan Point d) Cox Point. The location of the isobaths (m) is indicated at the top panel of each plot.

5.2.2 Stage 2: July 16-17

The onset of stage 2 is marked by an increase in the long-shore component of the wind (upwelling favourable) at both of the coastal stations. The July 16 (day 198), n7.15807 image is shown in Figure 5.8a. Temperatures of 12° to 13° C are observed along the coastline (A) with isolated patches of slightly cooler water. In the vicinity of La Perouse Bank (G), a tongue of 14° to 15° C water appears to be forming, and to the southeast, an area of colder water exists (H) that is probably due to outflow from the Juan de Fuca Strait (Griffin and LeBlond, 1990) or topographic upwelling (Freeland and Denman, 1982). The southern tip of the shelf-break jet has extended to approximately 90 km equatorward of Brooks Peninsula, and the band of warmer water between the jet and the coastline appears to be breaking down. At the tip of Brooks Peninsula (B), there are SST in the 10° to 11° C range that extend southward, but remain centered slightly seaward along the shelf-break and form the surface core of the shelf-break jet. North of Brooks Peninsula, the SST is masked by an extensive area of cloud cover. In the offshore waters (D), the SST have not changed significantly and remain around 14° to 15° C.

By July 17, the winds are nearing their peak value and the n7.15821 (day 199) image for this date is shown in Figure 5.8b. The 14° to 15°C offshore waters (D) have been pushed southward, and the northern extent of the 14° C water is nearly equal to the line of latitude that cuts across the northern tip of Washington State. The tongue of warmer water is still evident over La Perouse bank (G). There appears to be cold water along most of the coastline (A) with temperatures that have decreased from the previous day and are now in the 11° to 12° C range, but there are also isolated patches with SST around 10° C. The isolated patches of the colder water are probably due to small-scale variations in the topography that is causing local upwelling to occur in response to the large-scale increase

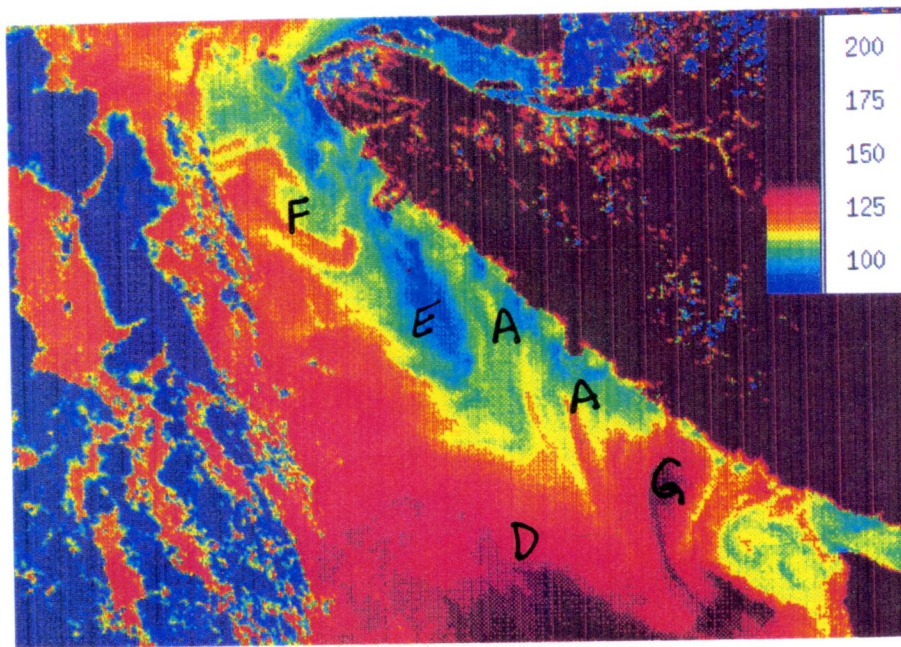
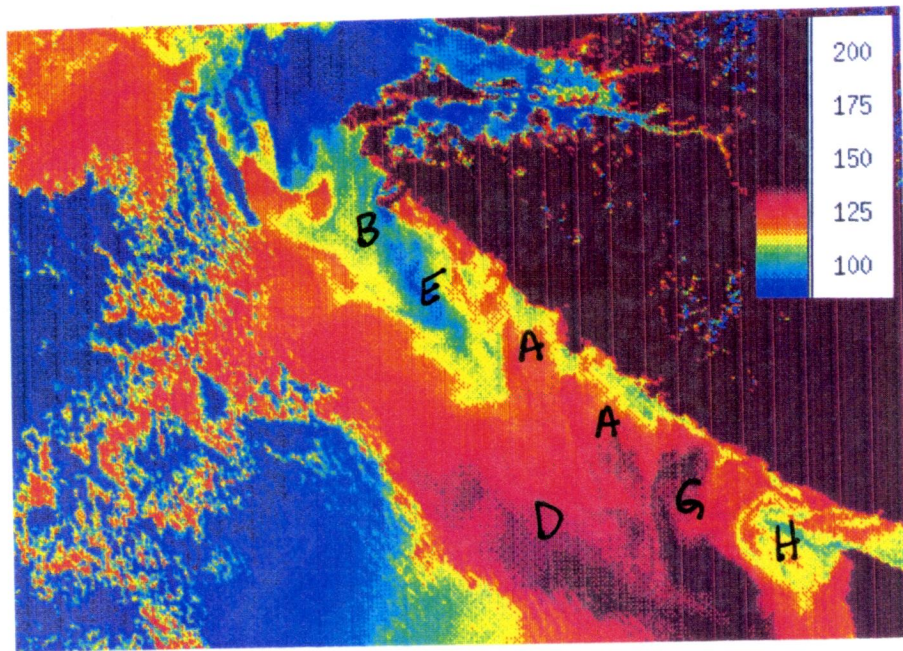


Figure 5.8. Stage 2 AVHRR imagery. a) July 16 (day 198) image, b) July 17 (day 199) image. The temperature scale ($\times 10^{-1}$) is shown in the upper right corner.

in the upwelling favourable winds. R.E. Thomson (pers. comm.) has suggested that the isolated patches of cold water along the coastline may also be related to tidal mixing and the formation of buoyant plumes of cold water that extend from the coastline. The shelf break jet is approximately 160 km equatorward of Brooks Peninsula, and there is a well developed 10° to 11° C surface core of the jet that extends about 100 to 120 km along the shelf-break. In the offshore waters between Brooks Peninsula and Cape Scott, there is continued evidence of frontal instability (F).

The cross-shore SST transects for stage 2 are shown in Figure 5.9. The SST structure at Brooks Peninsula (Figure 5.9a) has not changed significantly since stage 1. The coldest water is confined within approximately 10 km of the shoreline, and the temperature gradually increases before reaching a peak of about 13° C, seaward of the 2000 m contour. Evidence of the shelf-break jet can be seen in the SST transect at Tatchu Point (Figure 5.9b); the SST drops at the shelf-break and reaches a minimum just seaward of the shelf break. The cross-shore horizontal scale of the core of the shelf-break jet, as defined by the 11° C isotherm, is about 20 km. The offshore waters are about 1° C warmer on average than the shelf waters, with the maximum temperature of the shelf water occurring about mid-shelf.

The Estevan Point SST transect (Figure 5.9c) shows evidence of the shelf-break jet that can be seen in the slight temperature drop seaward of about the 200 m contour. As was the case at Tatchu Point, the shelf-water temperatures are at a maximum near the mid-shelf with a temperature decrease at the coastline. The same SST structure is apparent in the Cox Point transect (Figure 5.9d), but the temperature drop at the shelf break, indicating the presence of the shelf-break jet, is not as sharp as that at Estevan Point or Tatchu Point.

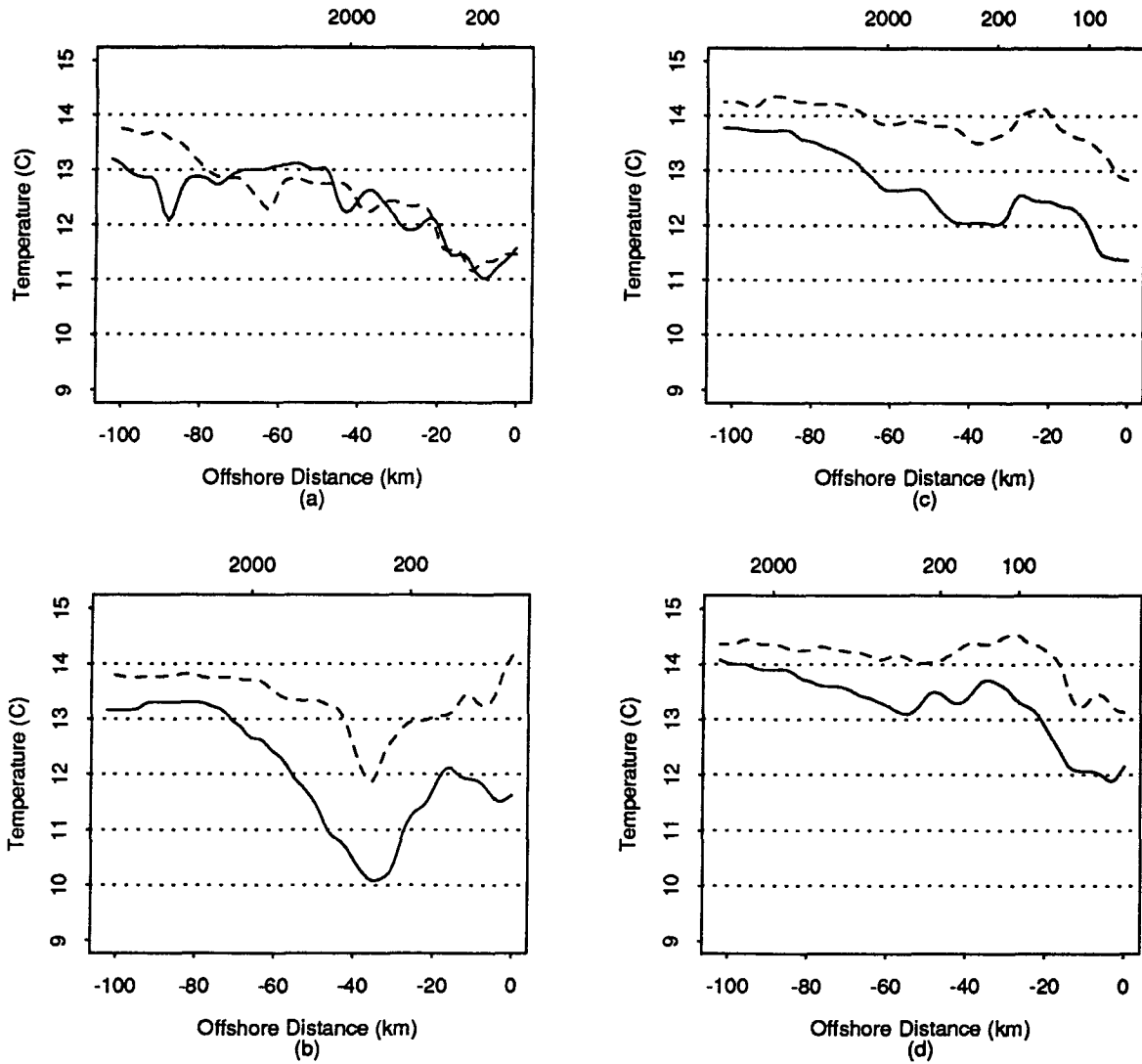


Figure 5.9. Stage 2 cross-shore SST transects (day 198-199) a) Brooks Peninsula b) Tatchu Point c) Estevan Point d) Cox Point. The location of the isobaths (m) is shown on the top of each plot. The dashed line is the cross-shore transect from stage 1.

The minimum SST for Estevan Point and Cox Point occurs at the coastline; this is in contrast to the Tatchu Point transect, where the minimum SST are at the shelf break. The bimodal temperature structure roughly between the 100 and 200 m in the Cox Point transect is due to the tongue of warm water over La Perouse Bank; the transect intersects the northern tip of the tongue and causes the apparent increase in the SST (see Figure 5.8b).

5.2.3 Stage 3: July 18-20

As was shown in Figures 5.1b, 5.3b, and 5.5, the peak winds occurred around July 18 (day 200); the peak winds at the northern end (Cape Scott) of Vancouver Island were at a maximum approximately one day before the peak winds near the southern end (Estevan Point). The July 18 (day 200), n7.15835 image is shown in Figure 5.10a. The decreased wind strength around Cape Scott (C) has resulted in an increase of the SST in the offshore waters as compared to the previous day, but the water along the shelf has remained essentially the same temperature. The structure of the shelf-break jet (E) does not seem as well defined as the previous images, but the southern tip of the jet is nearly 200 km equatorward of Brooks Peninsula. The 10° to 11° C surface core of the jet has also migrated equatorward. There is cold water along the coastline (A), and the coastal and shelf-break jet water does not appear to be mixing with the tongue of warm water that is sitting over La Perouse bank (G). In addition, the cold water at the mouth of the Strait of Juan de Fuca (H) does not appear to be breaking down the La Perouse Bank water, but in contrast to the previous image, cold water is evident between the northern tip of the tongue and the coastline; the cold water against the coastline could be due to the Vancouver Island Coastal Current that is advecting water northward from the Strait of Juan de Fuca outflow.

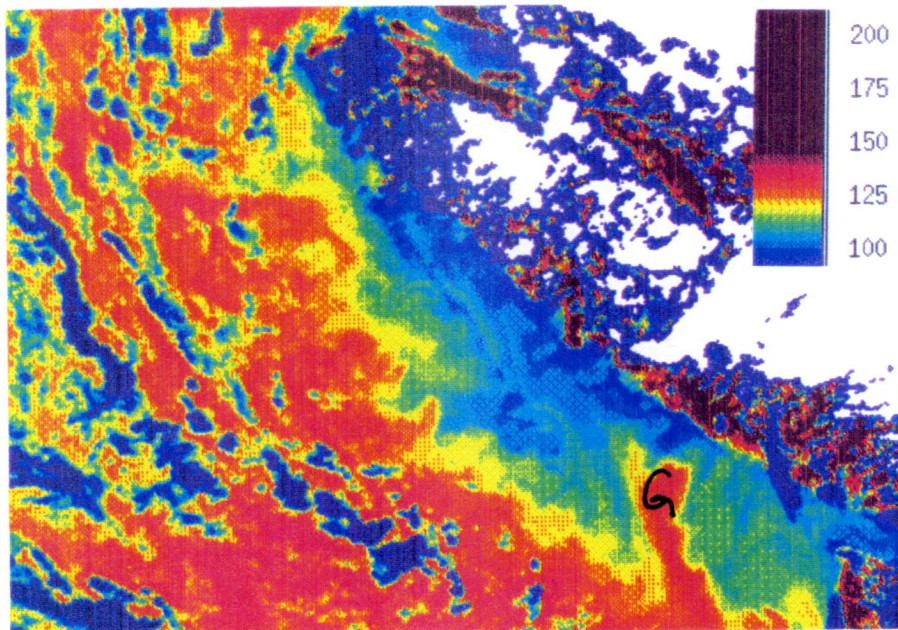
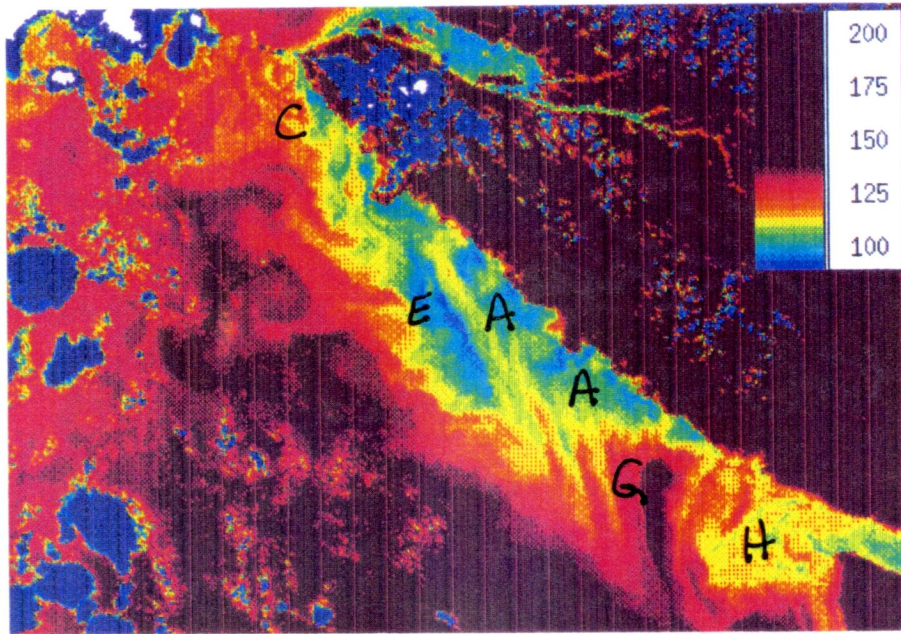


Figure 5.10. Stage 3 AVHRR imagery. a) July 18 (day 200) image b) July 20 (day 202) image. The temperature scale ($\times 10^{-1}$) is shown in the upper right corner.

The July 20 (day 202), n715863 image (Figure 5.10b) shows cold water along the entire coastline with no evidence of the thermal structure that defines the shelf-break jet. The average SST of the water along the shelf and offshore regions is in the 10° to 11° C range. The tongue of warmer water is still present over La Perouse Bank (G), but the temperatures have decreased and are typically 11 to 12° C. North of Brooks Peninsula there are patches of clouds along the coastline that extend to Cape Scott.

The interpretation of the July 20 image is not as obvious as the other images. There is a five-day gap between the July 13 to 18 image set and the July 23 to 24 image set. These images sets, with the exception of July 13, have entailed two passes per day, so that even though there may have been a change in the absolute SST between the two-daily images, the relative SST would have remained essentially the same, thus permitting a spatial comparison of the daily thermal structure. In contrast, there was only one AVHRR image available for July 20; however, multi-channel cloud detection analysis did not indicate the presence of clouds that may have caused an apparent reduction in the SST along Vancouver Island. Therefore, the satellite measurements obtained for July 20 would seem to indicate an over-all reduction in the SST as compared to the July 18 image.

The cross-shore SST transects for the July 18 to July 20 time frame are shown in Figure 5.11. As was the case for stages 1 and 2, the minimum SST for the Brooks Peninsula transect (Figure 5.11a) occur within approximately 10 km of the coastline. Gradually increasing from the 10° C minimum temperature at Brooks Peninsula, the SST reaches an average offshore value of around 12° C. The Tatchu Point transect (Figure 5.11b) shows that the temperature at the shelf-break has decreased slightly, but there has been a substantial decrease along the coastline; the coastline temperatures, which were previously around 1.5° C greater than the shelf-break temperatures are now 0.5° C colder. There is also evidence of a temperature maximum at mid-shelf, between the cooler shelf

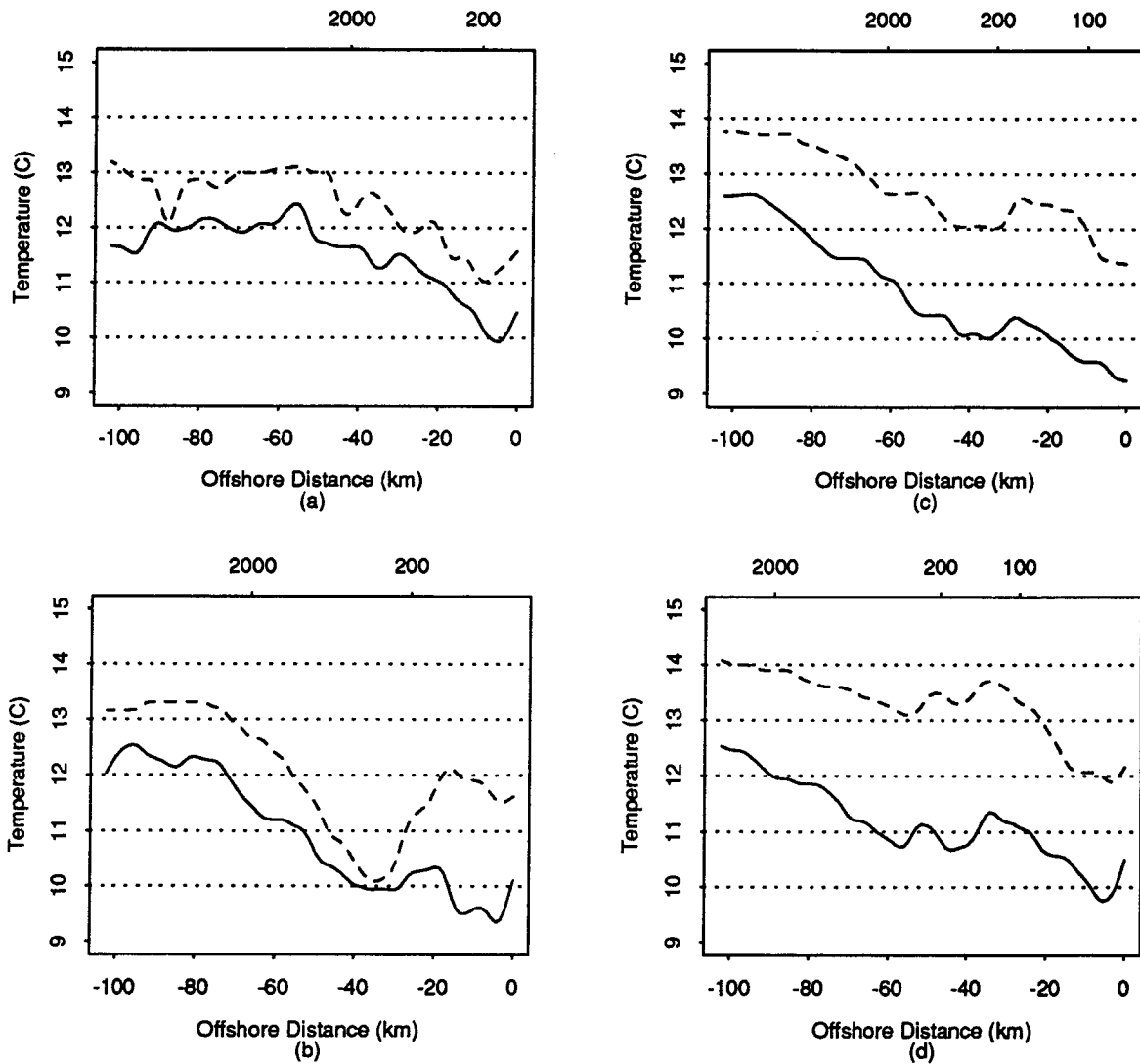


Figure 5.11. Stage 3 cross-shore SST transects (day 200-202) a) Brooks Peninsula b) Tatchu Point c) Estevan Point d) Cox Point. The location of the isobaths (m) is shown at the top of each plot. The dashed line is the cross-shore transect from stage 2.

break and coastal waters. The SST increases in the offshore direction and reaches a value of about 12° C, just seaward of the 2000 m contour.

The Estevan Point SST transect is shown in Figure 5.11c. The temperature at the coastline and at the shelf-break have each dropped about 2° C since stage 2, but there is still evidence of a local temperature maximum at mid-shelf. The SST drops slightly at the shelf-break and then increases. The Cox Point transect displays a similar structure to the Estevan Point and the Tatchu Point transect: cold water along the coastline, warming at mid-shelf, a slight temperature decrease at the shelf-break, and a temperature increase in the offshore direction. The bimodal temperature structure that is roughly between the 100 m and 200 m contour is more sharply defined than it was during stage 2.

5.2.4 Stage 4: July 23-24

Both the Bakun Upwelling Index and the coastal wind station data indicate that the upwelling favourable winds have significantly decreased in strength since the peak winds that occurred around July 18 (day 200). The July 23 (day 205), n7.15906 image is shown in Figure 5.12a. Along the coastline (A), there has been intense warming of the shelf waters with temperatures in the 13° C range. The 14° to 15° C tongue of warm water over La Perouse Bank (G) now extends to the coastline. Since there was no satellite imagery available, between July 20 and 23, it is not possible to tell if the warm tongue remained intact or mixed with the cooler, coastal water; however, the spatial location suggests that it did remain intact. As delineated by the 12° C isotherm, the shelf-break jet (E) is well defined and extends approximately 180 km equatorward of Brooks Peninsula, but still remains centered along the shelf-break. On both sides of Brooks Peninsula (B), there is evidence of 13° C water, but around Cape Scott (C), colder 10° to 12° C water covers the entire shelf.

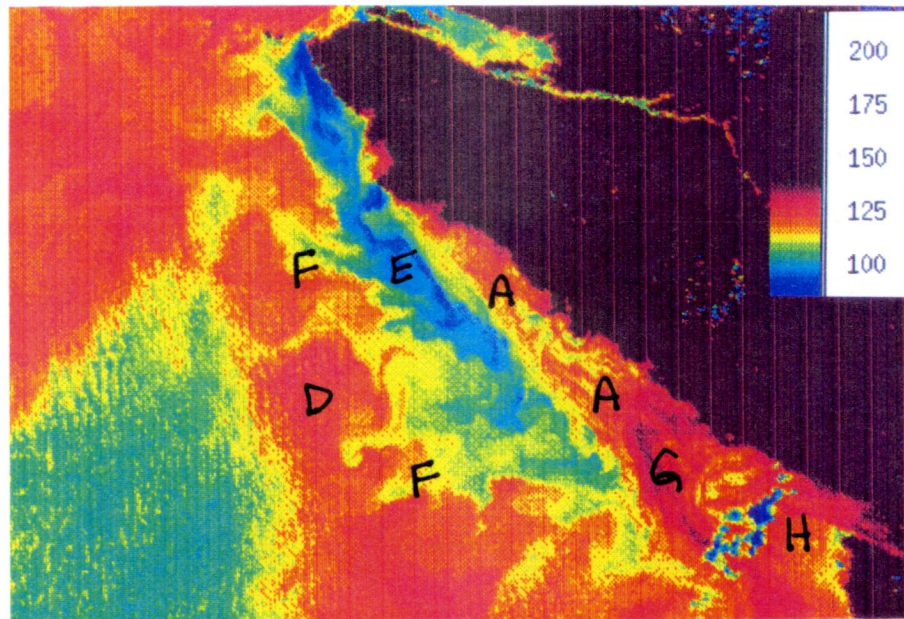
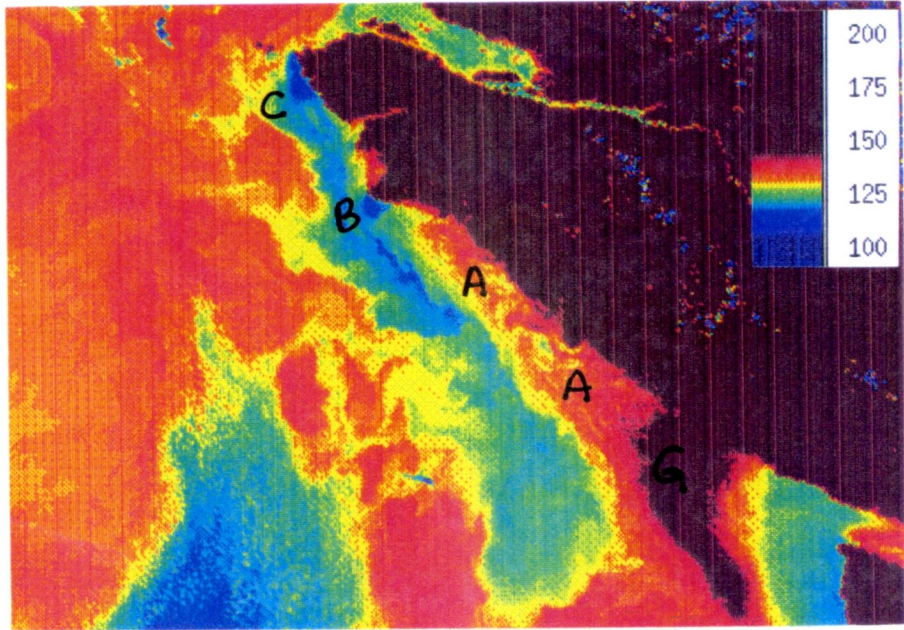


Figure 5.12. Stage 4 AVHRR imagery. a) July 23 (day 205) image b) July 24 (day 206) image. The temperature scale ($\times 10^{-1}$) is shown in the upper right corner.

On the following day, the n7.15920 (day 206) image (Figure 5.12b) does not indicate that any dramatic changes in the SST pattern have occurred. The cooler, shelf break waters (E) separate the warmer offshore (D) and shelf waters (A). The equatorward extent of the shelf-break jet is around 180 to 200 km, and the 10° to 11° C core of the jet extends approximately 120 km. Along the edge of the shelf-break jet, there are numerous cold-water filaments (F) extending into the offshore waters. There is still evidence of the warm, 14° to 15°C water over La Perouse Bank (G), and the colder water (H) that was present at the mouth of the Strait of Juan de Fuca (see Figure 5.8a) has increased in temperature and is now in the 13° to 14° C range.

The SST transects during stage 4 are shown in Figure 5.13. The Brooks Peninsula transect (Figure 5.13a) is similar to the transects taken at this location during the other stages: cold water within approximately 10 km of the coastline and a temperature increase in the offshore direction. Compared to the previous stage, the SST at the tip of Brooks Peninsula have increased about 0.5° C, but in the offshore waters, the temperature increase was around 1.0° C. To the south of Brooks Peninsula, the Tatchu Point transect (Figure 5.13b) shows the intense warming that has occurred along the shelf; the SST have increased to a maximum value of 14° C from a previous value of about 9.5° C during stage 3. The shelf-break jet signature is evident by the temperature minimum that is seaward of the shelf break.

The warming of the shelf waters is also apparent in the Estevan Point SST transect as shown in Figure 5.13c. The characteristic temperature drop occurs at the shelf break, followed by a gradual temperature increase in the offshore direction. The SST structure at Cox Point (Figure 5.13d) also shows the warm water over the shelf, and a temperature decrease at the shelf break; seaward of approximately the 2000 m contour, the SST

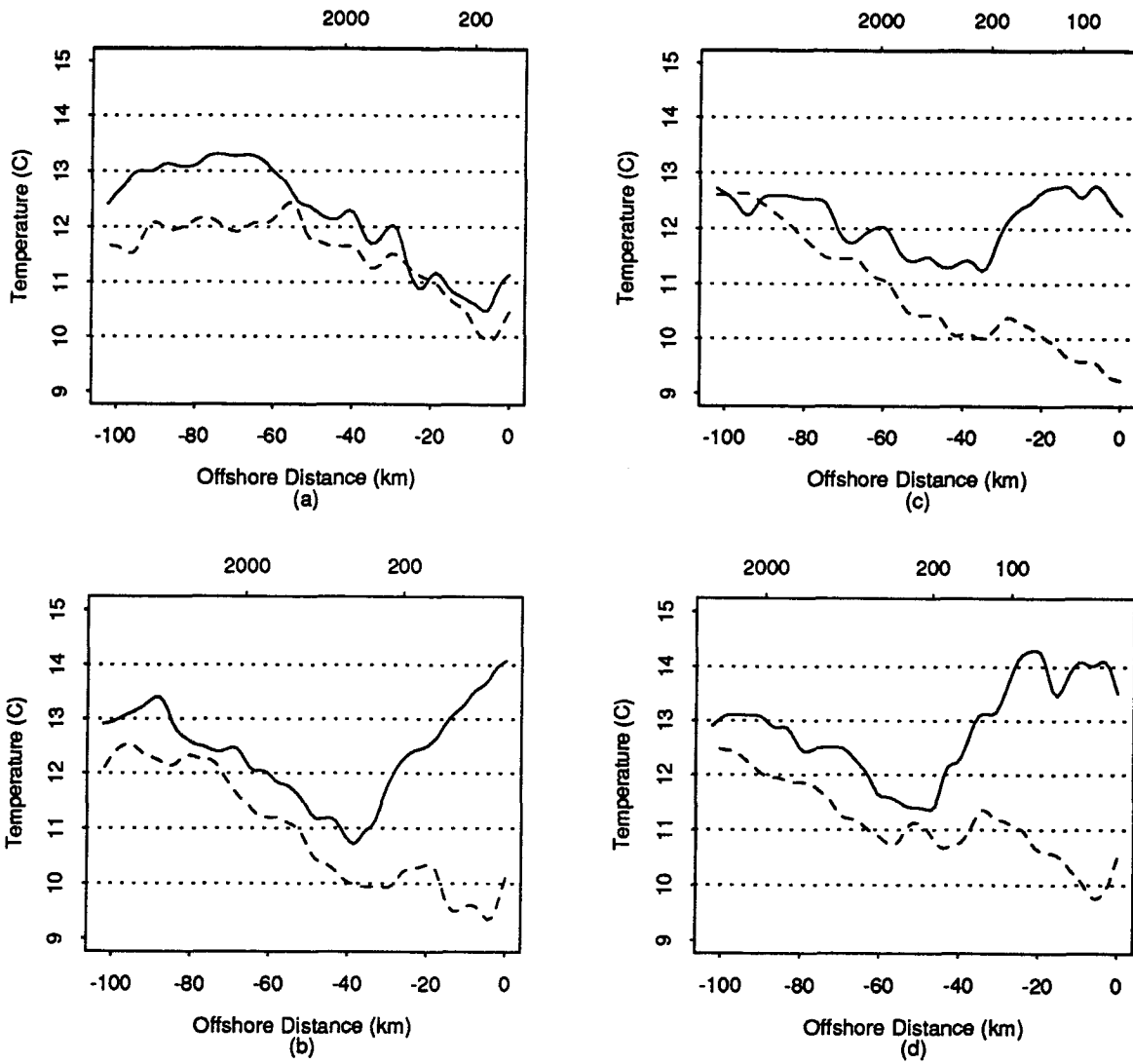


Figure 5.13. Stage 4 cross-shore SST transects a) Brooks Peninsula b) Tatchu Point c) Estevan Point d) Cox Point. The location of the isobaths (m) is shown at the top of each plot. The dashed line is the cross-shore transect from stage 3.

is essentially constant. The Cox Point transect also shows a sharp temperature fluctuation around the 100 m contour; this fluctuation is due to the warm water tongue over La Perouse Bank (see Figures 5.12b).

5.2.5 Long-shore Sea Surface Temperature

The temporal variation in the longshore averaged SST during the upwelling event is shown in Figure 5.14. Transects were taken roughly along the 100 m isobath (shelf water), 200 m isobath (shelf-break water), and the 1000 m isobath (offshore water), and extended approximately 220 km southward from Brooks Peninsula; each transect represent a sample of around 800 pixels. The late afternoon satellite passes (except July 13, day 195) were used to calculate the average temperature along the isobaths and the missing data points (days 201,203,204) were interpolated by means of a cubic spline.

On day 195 (July 13), the SST along the entire coast of Vancouver Island is uniform. From day 195 to day 197 (stage 1), the shelf and offshore temperatures are the same and increase in magnitude together. The shelf break temperature is also increasing during the same period, but by day 197 (July 15), the shelf-break temperature is about 1° C less than the shelf and offshore values; the temperature difference is due to the formation of the shelf-break jet that is gradually migrating equatorward and causing a lower average temperature along the shelf break. The overall-average SST reaches a maximum by day 197 (July 15). Following day 197, the winds increase in strength and there is an overall decrease in the SST (stage 2), but the coldest temperatures are still along the shelf break and the warmest temperatures are in the shelf waters; however, the temperatures along the shelf are approaching the shelf break temperatures.

Around day 200 (July 18), the winds are at a maximum, but it is not until day 202 that the minimum overall SST are observed (stage 3). By day 202, the shelf temperature is the same as the shelf break temperature, but the temperature in the offshore waters is about 1° C warmer. As the winds subside, the overall SST begin to increase (stage 4), but there is differential warming in the shelf, shelf break, and offshore waters.

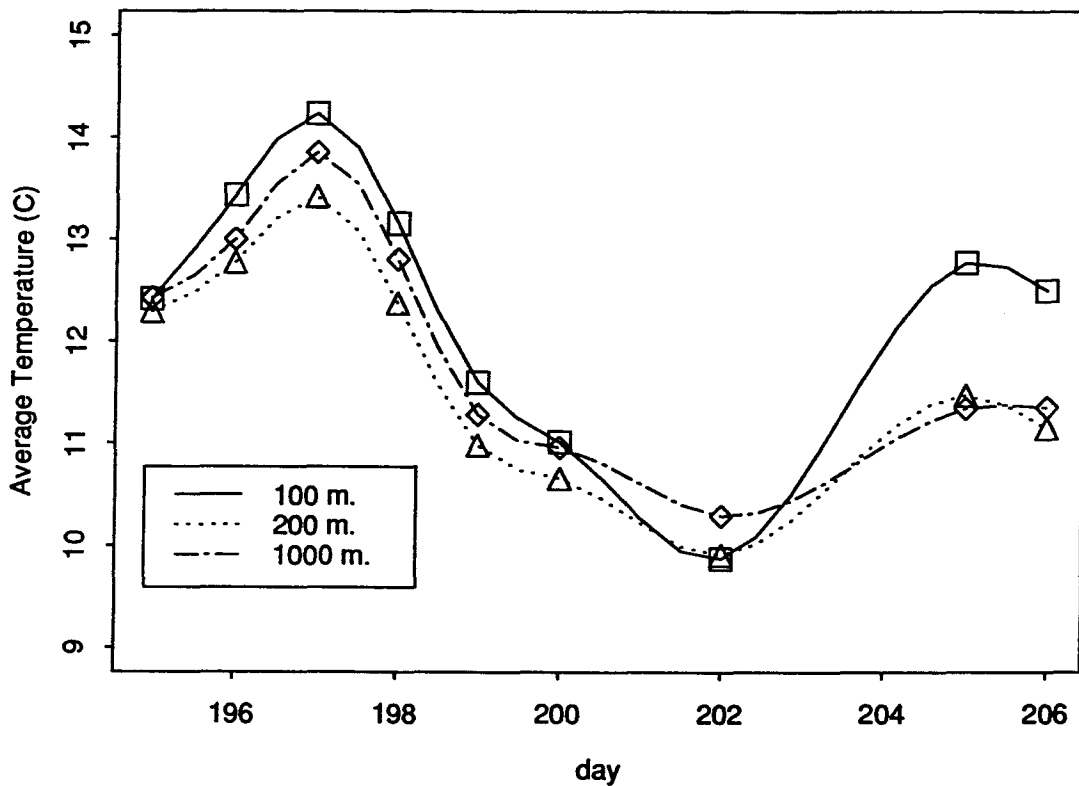


Figure 5.14. Long-shore SST transects south of Brooks Peninsula. The symbols (□△◇) indicate times when satellite data were available, and the lines (solid, dotted, broken) are the cubic spline fit to the long-shore averaged SST along the 100, 200, and 1000 m isobaths.

The most dramatic temperature rise is along the shelf where increases of about 3° C are observed. Both the offshore and the shelf break temperatures increase, but not to the same degree as the shelf temperatures. By day 205 (July 23), the shelf temperature is warmer than the offshore and shelf break temperatures, and the offshore and shelf break temperatures are essentially the same.

5.3 Hydrographic Structure

The Estevan Point hydrographic survey line (line G, Figure 3.5) was sampled between 8 am and 3 pm on July 25, one day after the last available satellite image; however, the temperature structure is probably similar to the previous few days and therefore represents the water properties during stage 4. The Estevan Point temperature and density structure for the top 200 m are shown in Figure 5.15. Below about 50 m, the isotherms (Figure 5.15a) and the isopycnals (Figure 5.15b) dome upward over the shelf and dip downward near the coastline and in the offshore region. The downward dip at the coastline is presumably due to the presence of the buoyancy driven Vancouver Island Coastal Current, and in addition, the downward dip seems to indicate that the characteristic upward tilt of the isopycnals and the isotherms associated with coastal upwelling is no longer present. Evidence of the equatorward flowing shelf break current is apparent in the downward tilt of the contours in the offshore direction.

In the upper 50 m, roughly delineated by the 8 degree isotherm and the 25.4 isopycnal, the wind influence can be seen in the water-property structure as compared to the conditions below 50 m. Over the shelf, the temperature structure indicates well stratified conditions, with isotherms that are essentially flat. The weak-wind conditions at the time of the hydrographic survey account for the shelf temperature structure, and AVHRR imagery also indicated that there was intense warming along the shelf. In the

vicinity of the shelf break, the isotherms dome upwards between the 200 m and the 1000 m contour, and the coldest water is slightly seaward of the shelf break; AVHRR imagery also shows cold water in the same location (see Figure 5.12b). The isotherm structure seems to indicate the occurrence of shelf-break upwelling that was probably at a peak around the time of the strongest winds (day 200), but has now subsided due to the weakening of the winds.

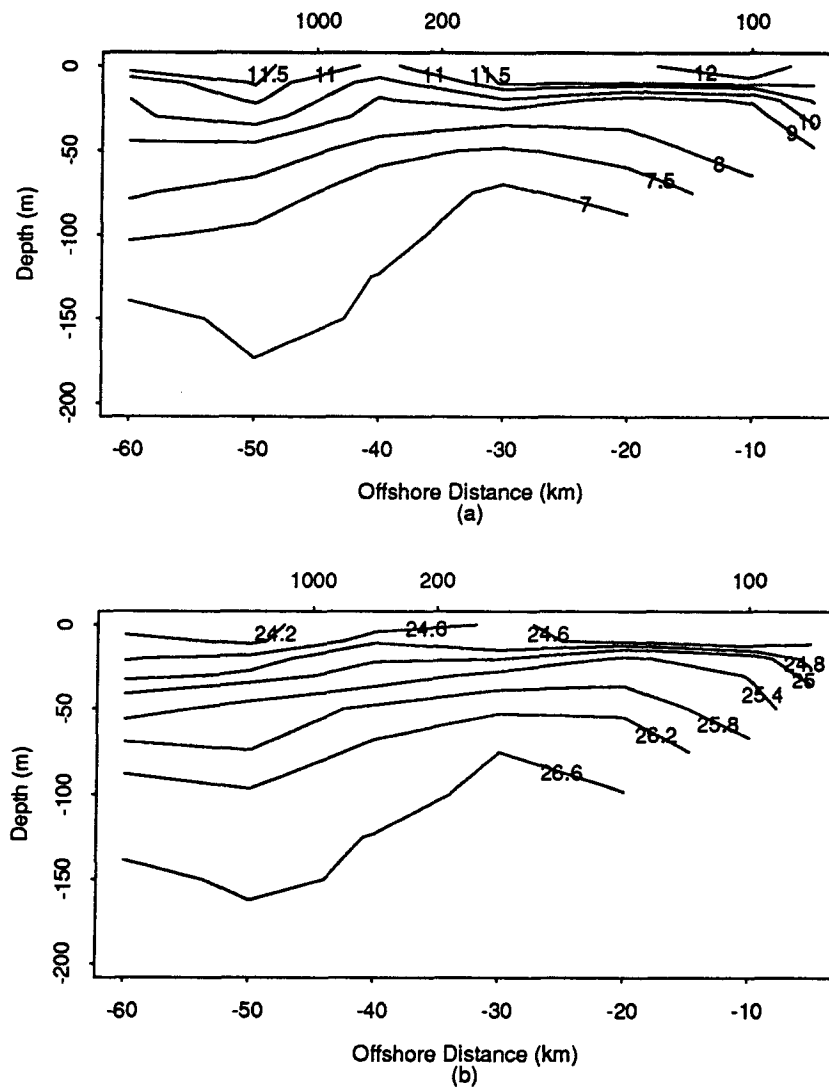


Figure 5.15. a) Estevan Point temperature contours b) Estevan Point sigma-t contours

Six-hourly subtidal velocity records from current meters at a depth of 30 m were obtained from station E2 (see Figure 3.5); station E2 is shoreward of the shelf break and on the hydrographic survey line that extends from Estevan Point. The current at E2 (Figure 5.16a) has a persistent southeasterly flow which is consistent with the direction of the shelf break current. Prior to the upwelling event, current speeds are around 20 cm/s. As the winds increase in strength, the current increases in strength to a peak value of around 30 cm/s, but continues to flow in essentially the same southeasterly direction. Following the peak in the wind stress (around July 18), the current speed decreases to the 5 to 10 cm/s range in response to the weakening winds.

The E2 mooring also recorded the six-hourly temperature at a depth of 30 m. As shown in Figure 5.16b, temperature is around 10° C, but as the winds increase, the temperature drops and reaches a minimum of about 8° C, near July 18 (day 200). There is some variability in the temperature as the winds weaken, but the temperature remains in the 8° C range. Six-hourly temperatures were also obtained at a depth of 5 m from the T3 station (see Figure 3.5). The mid-shelf, surface-layer time series at T3 (Figure 5.16c) is similar in structure to the temperatures at E2: prior to the upwelling event, temperatures are around 14° C and as the wind stress reaches a maximum, the temperature drops to about 11° C. However, in contrast to the E2 temperature structure that did not increase significantly as the winds weakened, the T3 temperature increases to around 13° C as the winds decrease in strength.

The temperatures variations from the subsurface moorings agree with the AVHRR observations and the temperature measurements from the Amphitrite Point Lightstation. The temperature decrease during the upwelling event is evident in the satellite imagery and the lightstation measurements, but as the winds weaken, the temperature increase along the shelf is greater than along the shelf break. AVHRR imagery and lightstation temperatures

indicate intense warming along the shelf which is consistent with the T3 temperature measurements, but along the shelf break, the temperature does not increase as dramatically. Satellite imagery and the temperatures at the E2 station verify the lower temperatures along the shelf break compared to the shelf temperatures.

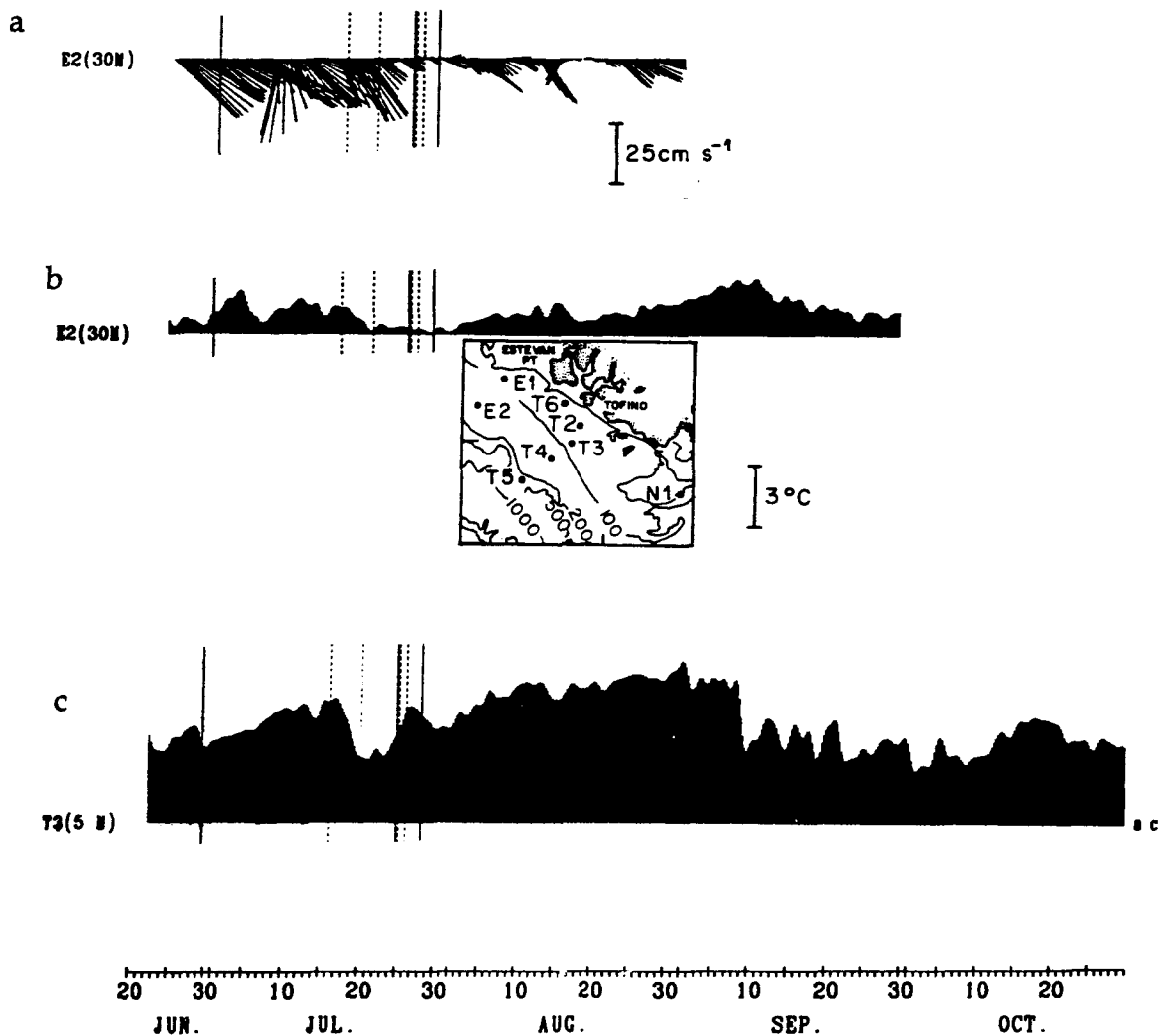


Figure 5.16. Estevan Point (E2) a) six-hourly subtidal velocity vectors b) six-hourly temperatures. Both (a) and (b) are at a depth of \approx 30 m. c) Cox Point (T3) surface layer six-hourly temperature at a depth of \approx 5 m. The baseline temperature is 8° C and the 3° C temperature scale is also shown. Adapted from Hickey et al. (1991)

5.4 Dynamical Interpretation

5.4.1 Cross-shore Fronts

The cross-shore structure of the SST south of Brooks Peninsula was examined using an edge detector (section 3.3); the edge detector provides an estimate of the SST gradient and hence will indicate the location of regions where there is a sharp change in the temperature. The output from the edge detector, as shown in Figure 5.17, indicated that there were four zones of strong SST gradients, or fronts: there was a shelf front (s) along the mid-shelf, a shelf-break front (b) that was generally along the inshore side of the shelf break, and an offshore front (o). There was also an indication of an offshore shelf-break front (d) that was on the offshore side of the shelf break and was probably the offshore extent of the cold-core of the shelf-break jet; this front was most pronounced off Tatchu Point (Figure 5.17b). The location of the minimum SST (t) that roughly defines the central axis of the shelf-break jet is also shown in Figure 5.17. The fronts in the vicinity of Brooks Peninsula are shown in Figure 5.17a. Due to the narrow continental shelf off Brooks Peninsula (see Figure 2.2), the shelf-break inshore front (b) and the minimum temperature (t) are at the same location, essentially along the shelf break, and show little variation during the upwelling event.

The offshore front (o) is about 40 km from the tip of Brooks Peninsula, but it does display some cross-shore variability. At the end of the upwelling event (day 205 to 206), there is a tendency for the offshore and the inshore shelf-break fronts to converge. The cross-shore SST transects discussed previously (see Figures 5.7a, 5.9a, 5.11a, 5.13a) show that the temperature increases in the offshore direction, out to approximately 40 to 50 km offshore (around the 2000 m contour), and remains fairly constant beyond that point. The offshore front probably indicates the offshore edge of the shelf break current.

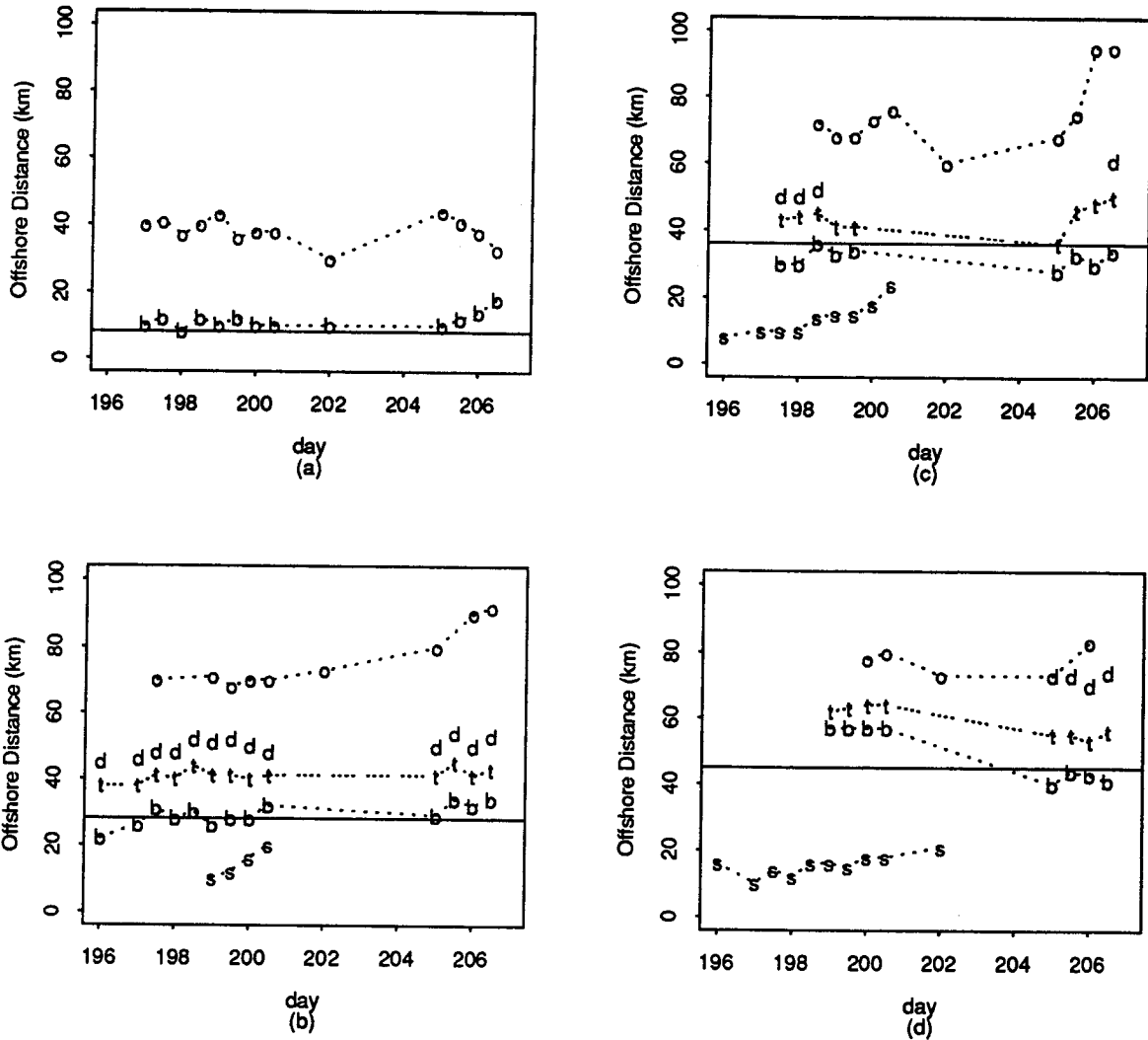


Figure 5.17. Cross-shore SST fronts a) Brooks Peninsula b) Tatchu Point c) Estevan Point d) Cox Point. s=shelf front, b=inshore shelf break front, t=minimum temperature (between the shelf break fronts), d=offshore shelf break front, o=offshore front. The letters (sbtdo) indicate the spatial location of the SST front calculated for each satellite image using the Sobel edge detector. The solid horizontal line is the location of the shelf break (≈ 200 m isobath) at each cross-shore location.

Moving to the south, the fronts off Tatchu Point (Figure 5.17b) and Estevan Point (Figure 5.17c) indicate the presence of a shelf front (s) that appears to migrate in the offshore direction. The shelf front is probably due to coastal upwelling, but between approximately day 200 and day 204, only the offshore front was detected, so it is not clear how far offshore the shelf front migrated. In a study off Vancouver Island, Ikeda and Emery (1984) quote an offshore migration rate of 10 km/day, and mention that the upwelling front they observed eventually passed beyond the shelf break. However, after day 204 of this study, the shelf front is not present indicating that coastal upwelling has ceased.

Along the shelf break at Tatchu Point, and to a lesser degree at Estevan Point, there is a well defined inshore shelf-break front (b) and an offshore shelf-break front (d). The minimum temperature (t) is between the fronts and remains seaward of the shelf break during the upwelling event. The cross-shore width of the shelf-break fronts (d - b) is about 20 km, and using (4.12) with $g'=0.02$, $H_1=200$ m, $H_2=1000$ m, and $f=10^{-4}$, gives a Rossby radius of about 18 km which agrees with the observations; the Rossby radius of 18 to 20 km is also consistent with the 15 to 20 km range for the Rossby radius as suggested by Emery et al. (1984). As previously mentioned, when shelf break upwelling occurs, the upwelled water is confined to the shelf break region with the cross-shore width scale given by the internal Rossby radius of deformation. Although the presence of a cross-shore scale that is consistent with the Rossby radius does not imply that shelf break upwelling is occurring, it does indicate that the cross-shore scale of the dynamical processes along the shelf break are characterized by the Rossby radius.

Approximately 70 to 80 km offshore of Tatchu Point and Estevan Point (Figure 5.17b & 5.17c), the offshore front (o) is evident. During the upwelling event, the offshore front is reasonably stationary, but after day 204 the front appears to migrate farther

offshore. Since the cross-shore frontal structure was calculated at discrete locations along Vancouver Island, the offshore migration, particularly at Estevan Point, indicates the presence of offshore filaments and does not indicate that the entire offshore front has migrated (see Figure 5.12b(F)). As was the case with Brooks Peninsula, the offshore front is probably the offshore edge of the shelf break current; evidence of this can be seen in Figure 2.5 that shows the velocity structure off Estevan Point during July 1980 and indicates the offshore edge of the shelf break current approximately 70 km from the coastline.

The frontal structure offshore of Cox Point is shown in Figure 5.17d. The shelf front (s), perhaps indicates that coastal upwelling is occurring. Given the separation between the shelf and the shelf-break fronts, it is unlikely that the two fronts merged during the upwelling event. Along the shelf break, the minimum temperatures (t) remain seaward of the shelf-break, but after day 204, there is a tendency for the minimum temperatures and the inshore shelf-break front (b) to migrate inshore. Approximately 70 to 80 km from the coastline, the offshore front (o) is present.

The offshore front at Brooks Peninsula was approximately 40 km from the coastline, but at Tatchu Point, Estevan Point, and Cox Point, the offshore front was between 70 and 80 km from the coastline. A study by Fang and Hsieh that used eight years of summer AVHRR data from Vancouver Island indicated that the offshore front was typically 70 km from the coastline, but varied depending on the upwelling response. The variation in the offshore front location is presumably related to the variation in the long-shore topography. The continental shelf is the narrowest off Brooks Peninsula and gets progressively wider toward the north; to the south of Brooks Peninsula, the continental shelf also gets wider and reaches its widest point off Barkley Sound (see Figure 2.1). In addition to the width of the shelf increasing, the gradient of the continental slope decreases

southward of Brooks Peninsula. As suggested by Mooers et al. (1976), the Rossby radius of deformation can be modified by topography so that the shelf and slope widths also become horizontal scales. The topographic variations that occur southward of Brooks Peninsula may account for the observed variations in the cross-shore SST frontal structure, and the tendency for the minimum temperature (t) to be displaced slightly seaward of the shelf break when moving in the southward direction.

5.4.2 Shelf-break Jet Formation

The preceding section indicated that the shelf break fronts were confined along the shelf break. Using a simple time-independent barotropic model as suggested by Thomson and Gower (1986), the governing equation is the conservation of potential vorticity,

$$\left(\bar{u} \frac{\partial}{\partial x} + \bar{v} \frac{\partial}{\partial y} \right) \frac{f + \bar{\zeta}}{H} = 0 \quad (5.1)$$

where (u,v) are the time-averaged cross-shore (x) and the long-shore (y) velocity components, $\bar{\zeta}$ is the vertical component of the mean relative vorticity, H is the depth, and f is the Coriolis parameter. Equation (5.1) can be expanded as,

$$\begin{aligned} & -u \left(\frac{1}{H^2} (f + \bar{\zeta}) \frac{\partial H}{\partial x} \right)_{(i)} + u \left(\frac{1}{H} \frac{\partial}{\partial x} (f + \bar{\zeta}) \right)_{(ii)} \\ & -v \left(\frac{1}{H^2} (f + \bar{\zeta}) \frac{\partial H}{\partial y} \right)_{(iii)} + v \left(\frac{1}{H} \frac{\partial}{\partial y} (f + \bar{\zeta}) \right)_{(iv)} = 0 \end{aligned} \quad (5.2)$$

Using scaling arguments outlined by Freeland et al. (1984), term (i) in (5.2) is much greater than term (ii) and term (ii) can be neglected. If there is no variation in the long-shore direction in H and $\bar{\zeta}$, then term (iii) vanishes, and term (iv) is written as $(H \beta \cos \theta)^{-1}$ where θ is the angle between the coastline and a line of longitude, and (5.2) can be written in the form,

$$\bar{v}(x) \approx \frac{fU}{H_0 \beta \cos \theta} \frac{1}{H} \frac{dH}{dx} \quad (5.3)$$

where $U = uH_0$ is the cross-shore transport in the benthic layer and the geostrophic interior at the edge of the continental margin (depth H_0) and is equal to the cross-shore transport $u_E \delta$ in the Ekman layer, where u_E is the Ekman layer cross-shore velocity, and δ is the Ekman layer thickness (see Figure 4.1). Thomson and Gower further assume an Ekman layer balance of the form,

$$\rho_0 f u_E = \frac{\partial \tau}{\partial z} \quad (5.4)$$

where ρ_0 is the water density and τ is the long-shore component of the wind stress. If (5.4) is integrated over the surface Ekman layer depth, and with the application of (4.1) and (4.2), equation (5.3) can be written as,

$$\bar{v}(x) \approx \frac{C_D \left(\frac{\rho_a}{\rho} \right) V^2}{H_0 \beta \cos \theta} \frac{1}{H} \frac{dH}{dx} \quad (5.5)$$

where $v(x)$ is the long-shore speed, C_D is the drag coefficient, ρ_a is the density of the atmosphere, ρ is the density of the water, and V is the long-shore component of the wind velocity. The long-shore speed $v(x)$ using digitized topography off Estevan Point and a wind speed of 7.5 m/s is shown in Figure 5.18. The results of this simple model show why the band of cold water observed along the shelf break will tend to remain centered slightly seaward of the shelf break: the peak long-shore speeds are along the shelf break where there is the rapid change in topography. Near the shoreline there are high speeds, but Freeland et al. (1984) comment that the Vancouver Island Coastal Current is buoyancy driven and not wind driven.

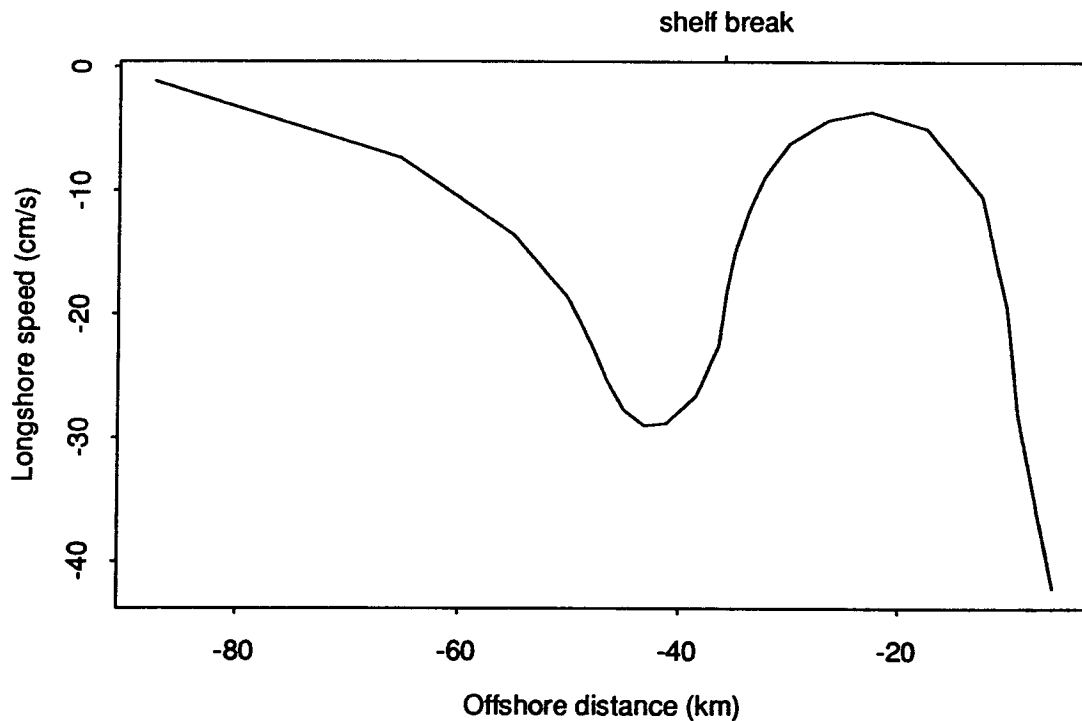


Figure 5.18. Estevan Point long-shore speed from (5.5) using $\rho_a/\rho \approx 10^{-3}$, $H_0 = 2500$ m, $\beta = 1.5 \times 10^{-11} \text{ m}^{-1}\text{s}^{-1}$, $\theta = 30^\circ$, and $V = 7.5$ m/s. The location of the shelf break (≈ 200 m isobath) is indicated at the top of the plot.

There is also a considerable amount of shear in the cross-shore direction; the shear on the onshore side of the shelf break is greater than the shear on the offshore side of the shelf break over the same cross-shore distance. The variation in the cross-shore shear, which is related to the cross-shore variation in the topography, may account for the continuous presence of the onshore shelf-break front which was most pronounced off Brooks Peninsula and Tatchu Point (see Figure 5.17). Although the offshore shelf-break front was continuous off Tatchu Point, at Estevan Point and Cox Point, the offshore shelf-break front was not as distinct, but appeared to merge with the offshore front.

5.4.3 Surface Velocity and Shelf Break Upwelling

A feature tracking method was used to estimate the surface velocities using sequential AVHRR images. The feature tracking method requires features in the satellite imagery to remain reasonably invariant over the period that the velocities are estimated, and in the case of AVHRR imagery, the natural choice for a feature is to select a strong thermal front. Studies by Kelly and Strub (1992), Ninnis et al. (1986), and Emery et al. (1986) have used a variation of the feature tracking scheme in the form of a cross correlation technique to automate the velocity field extraction from sequential AVHRR images; the surface velocity estimates they obtained were consistent with *in situ* current measurements and CTD-derived geostrophic currents. A modified version of the cross correlation technique was used by Holland and Yan (1992) to estimate surface velocities from AVHRR imagery separated by up to 24 hours, and their AVHRR velocity estimates agreed favourably with anchored and drifting buoy measurements.

The feature tracking procedure to estimate surface velocities can be simplified if a subregion of an entire AVHRR image is selected, and the surface velocities are calculated

within that subregion. A subregion was selected that was bounded in the long-shore direction by Brooks Peninsula and Cox Point, and in the cross-shore direction by roughly the 100 m and 2000 m isobaths; this subregion also contains most of the spatial variation in the SST observed during the upwelling event, and encompasses the cross-shore extent of the shelf break current.

The Sobel edge detector was applied to the July image sequence, and the locations of the sharpest edge detector responses, which corresponds to the strongest thermal gradients, were calculated. The spatial differences of the edges were measured between sequential day-time satellite images (24-hour separation), and the difference converted into a surface velocity. R. E. Thomson (pers. comm.) suggested that maximum velocities of the shelf break current are order 100 cm/s, so an edge decorrelation scale of 85 km was used, which means that a given edge represents the same thermal front if the edge moved less than 85 km in 24 hours. To further simplify the velocity estimates, only the long-shore velocity was calculated; the sharpest long-shore response of the edge detector occurred at the equatorward edge of the shelf break jet, and the long-shore migration of this edge presumably represents the surface expression of the intensification of the shelf break current.

The results of the Sobel edge detector for July 16 (day 198) and July 17 (day 199) are shown in Figure 5.19. In the Sobel edge-maps, it was possible to identify three dominant edges, S1, S2, and S3 that roughly correspond to the 12°, 11°, and the 10° isotherms (the relationship of the edges to the isotherms was verified by checking the spatial location of the edges to the spatial location of the isotherms obtained from a contour plot of the SST). The equatorward tip of the edges was along the shelf break, and the AVHRR-derived velocities were estimated by measuring the displacement of each edge.

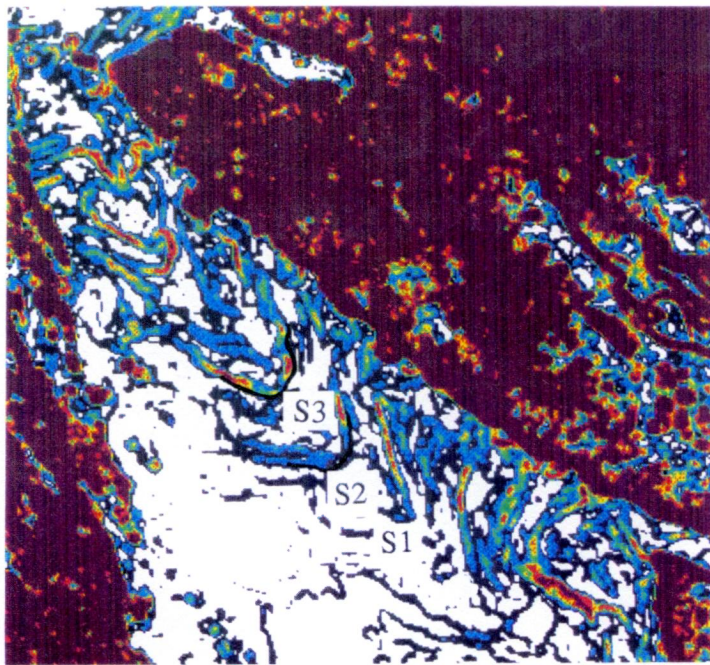
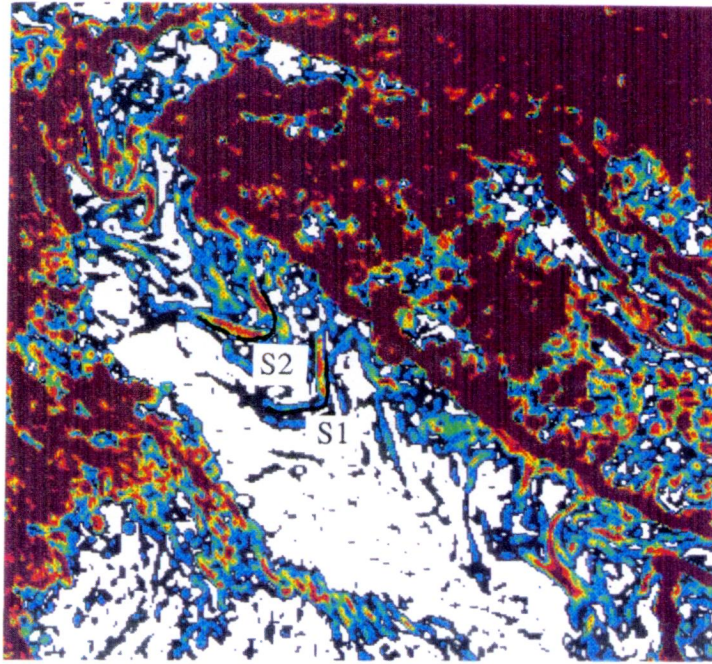


Figure 5.19. Sobel edge maps. a) July 16 (day 198). Edge S1 (12° isotherm) and edge S2 (11° isotherm). b) July 17 (day 199). Edge S1, edge S2 and edge S3 (10° isotherm). In (a), there is no evidence of edge S3 (10° isotherm), and in (b), the equatorward extend of edge S1 (12° isotherm) is difficult to identify.

The results of the long-shore velocity estimates are shown in Table 5.2. The imaged-derived velocities were calculated between July 14 (day 196) and July 18 (day 200) using sequential, afternoon AVHRR images (the July 15 velocity is the average from July 14 to July 15, etc.); these dates correspond to stages 2 and 3, and occur during the time when the upwelling favourable winds are increasing in strength. A time-independent barotropic model was also used to estimate the long-shore velocity in the vicinity of the shelf break; using (5.5), the wind speed was varied, and speeds of 5 m/s, 7.5 m/s, 10 m/s, and 12.5 m/s, which roughly corresponds to the daily-averaged long-shore wind at Estevan Point (see Figure 5.3b) for July 15, July 16, July 17, and July 18 were used. In addition, the long-shore, daily-averaged current from the E2 mooring (from Figure 5.16a) is also shown in Table 5.2.

Date	avhrr			$\bar{v}(x)$	E2
	S1	S2	S3		
July 15	10	—	—	10	20
16	60	—	—	30	30
17	75	80	—	60	30
18	—	35	30	100	30

Table 5.2. Long-shore velocity estimates (cm/s) using AVHRR measurements of edges S1, S2, and S3, time-independent barotropic model, and measurements from the E2 current mooring. The blank (—) entries under AVHRR indicate when the edges S1, S2, or S3 were not readily discernible. Errors in the AVHRR velocity estimates are around 15 cm/s.

The errors in the AVHRR estimates of the velocity are mainly due to image navigation and calculating the spatial displacement of the edge. Simpson (1990) indicates that in a reasonably noise-free image, the Sobel operator performs well in detecting edges, so that the edges detected are from SST gradients and not noise-generated. Emery et al. (1989) give image navigation errors on order of 2 km, and the error associated with the spatial displacement of the edge (pixel to pixel comparison) is estimated to be about 10 km. Using a conservative navigation error of 4 km, and combined with the spatial displacement error of 10 km, yield an AVHRR velocity error-estimate of around 15 cm/s.

The image-derived velocities and the velocities derived from the time-independent barotropic model are typically larger than the results from the moored current meter, but all of the measurements show that the long-shore velocity increases as the winds increase in strength. Using (4.11c) with the previously calculated long-shore wind stress value of 0.16 kg/m^3 (10 m/s wind speed), $\rho = 1025 \text{ kg/m}^3$, $H_1 = 150$, and $y = 0$, indicates that the long-shore current should increase by about 0.1 (m/s)/day, which is consistent with the velocity increase at the E2 current mooring, but considerable less than the increase calculated by the other methods. Since the barotropic model lacks stratification and friction, it is not surprising that it shows larger increases in the velocity. However, the image-derived and barotropic-model velocity estimates, and current meter velocities are all in reasonable agreement.

In the case of the image-derived velocity estimates, there is a sharp increase in the velocity between July 15 and July 16, as measured by the displacement of S1 edge. From July 16 to July 17, the S1 edge velocity increases slightly and is comparable to the S2 edge velocity. Between July 17 and July 18, the image-derived velocities decrease and are comparable to the velocity measurements obtained from the E2 current mooring. Johnson and Nurser (1984) suggest that during the build up of coastal upwelling, there is secondary

upwelling along the shelf break, but when the coastal upwelling reaches a quasi-steady state, the upwelling along the shelf break starts to decay. The relatively large velocities estimated from the AVHRR imagery (July 16 to July 17) could be evidence of shelf break upwelling: the temperature decrease along the shelf break (as indicated by the AVHRR velocities) is greater than the rate that the temperature decrease could be advected along the shelf break (as indicated by the E2 current mooring). However, as the coastal upwelling reaches a quasi-steady state and shelf break upwelling starts to decay, the AVHRR velocities are similar to the velocity measurements from the E2 current mooring.

Further corroboration that the image-derived velocities are indicating that shelf break upwelling is occurring can be seen in the longshore averaged SST structure (see Figure 5.14). After July 15 (day 197), each of the longshore averaged SST transects decrease at about the same rate. Around July 17 (day 199), the rate of temperature decrease along the shelf break (200 m isobath) begins to slow down, but the rate of temperature decrease along the shelf (100 m isobath) increases. Presumably, the slow down of the rate of temperature decrease along the shelf break indicates that the coastal upwelling is approaching a quasi-steady state, and the upwelling along the shelf break is starting to decay (see Johnson and Nurser, 1984). If the coastal upwelling is approaching a quasi-steady state, the steady state probably occurs around July 20 (day 202) when the shelf and shelf break temperatures are essentially the same.

In addition to the AVHRR-derived surface velocity and the longshore averaged SST arguments that shelf break upwelling is occurring, additional evidence, that was discussed previously, also indicates that shelf break upwelling is occurring. When shelf break upwelling occurs, the upwelled water is confined to the shelf break region, with the horizontal width scale given by the internal Rossby radius of deformation; the SST fronts, that were shown in Figure 5.17, have a cross-shore scale that is consistent with the internal

Rossby radius, thus suggesting that there is shelf break upwelling. Additional evidence can be seen in the Estevan Point cross-shore temperature contours (see Figure 5.15a). Although the Estevan Point temperature structure was calculated from data obtained at the end of the July upwelling event, the apparent signature of shelf break upwelling can be seen in the isotherms that dome upwards over the shelf break, with minimum surface temperatures slightly seaward of the shelf break.

CHAPTER 6

SUMMARY AND CONCLUSIONS

6.1 Summary of Results

AVHRR satellite imagery of the west coast of Vancouver Island was obtained from July 1984. The imagery spanned a period of time when there was a dramatic increase of upwelling favourable winds and permitted observations of the spatial and temporal variations of the SST structure during the upwelling event. In conjunction with the satellite data, coastal wind data along Vancouver Island were obtained from climatological stations at Cape Scott and Estevan Point. Lightstations at Kains Island, south of Cape Scott, and Amphitrite Point, south of Estevan Point, provided surface measurements of the ocean temperature. Near the end of the satellite coverage, an oceanographic cruise took place and hydrographic measurements within the water column were taken, and in addition, subsurface measurements of the current velocity and temperature were also available from current meter moorings. Large-scale estimates of the wind in the form of the Bakun Upwelling Index were obtained from two locations that were northward and southward of Vancouver Island.

The SST that the AVHRR instrument measures is based on the temperature in the top 0.01 mm of the ocean surface, the so called skin temperature. Therefore, care must be taken to insure that appearance of temperature gradients in the SST image are related to dynamical processes within the ocean, and not due to variations in the skin temperatures or an apparent SST decrease caused by cloud contamination. The imagery was cloud-

screened using subjective and multi-channel comparative techniques, and a comparison between in situ measurements of the sea surface temperature and AVHRR measurements was well correlated in the top 3 to 4 meters of the water column, but decreased significantly with increasing depth. The correlation was consistent with the observations that the skin temperature measurement made by the AVHRR is representative of the temperature in the upper few meters of the water column, the so called bulk sea surface temperature.

Coastal wind data and proxy wind data in the form of the Bakun Upwelling Index both indicated a dramatic increase in the upwelling favourable winds, and sea surface temperature data from coastal lightstations showed a decrease in the ocean temperature that was related to the increasing wind. Simultaneously with the increase in the strength of the wind, and the temperature decrease at the lightstations, AVHRR imagery revealed the presence of cold water, that initially appeared in the vicinity of Cape Scott and at the tip of Brooks Peninsula, and subsequently migrated equatorward from both locations. The cold water was due to upwelling, and the agreement between the increase in the strength of the wind, and the appearance of cooler temperatures in the satellite imagery indicated that the AVHRR measurements of the SST were tracking the surface manifestation of the ensuing upwelling event.

The AVHRR observations of the upwelling event were divided into four stages that primarily concentrated in the area to the south of Brooks Peninsula. Stage 1 is concerned with the initial appearance of cold water in the vicinity of Cape Scott and Brooks Peninsula, and usually indicates the pending start of the upwelling event. Due to the topographic variations around Brooks Peninsula, the initial appearance of the cold water is probably due to enhanced upwelling. Stage 2 deals with the equatorward migration of the cold water as the winds increase in strength. Satellite imagery shows that a plume of cold water extends equatorward from Brooks Peninsula and takes on a jet-like structure (shelf-break jet); the

central axis of the shelf-break jet, which also coincides with the minimum SST, is centered slightly seaward along the shelf-break. During stage 2, there is also evidence of isolated patches of cold water along the coastline which are presumably related to coastal upwelling or tidal mixing. However, most of the cold water stretches along the shelf break indicating that shelf break upwelling is pumping cold water into the surface Ekman layer, and the cold water is acting as a thermal tracer that delineates the intensifying shelf break current.

Stage 3 occurs when the winds are at their maximum strength, and there is evidence of cold, upwelled water over the entire shelf, and shelf break regions. The weakening winds mark the onset of stage 4; during this relaxation period, satellite imagery shows that there is intense warming of the relatively shallow shelf-waters to the south of Brooks Peninsula. In addition, there is also warming in the offshore waters, but between the warm offshore and shelf waters, a band of cold water persists along the shelf break that is probably relic upwelled water that has remained along the shelf break in spite of the weakening winds. The persistence of band of cold water along the shelf break during the upwelling event was explained in terms of the conservation of potential vorticity by evoking a simple barotropic model that was tied to the sharp change in the cross-shore topography at the shelf break. Although shelf break upwelling is the likely cause of the cold water along the shelf break, it is possible that the water was advected from regions further north. After a few days of relatively weak winds, the strong thermal gradients observed along the shelf break were no longer present in the AVHRR imagery.

Analysis of the SST imagery using an edge detector indicated the presence of strong thermal fronts on the inshore and offshore side of the shelf break, and a front in the offshore waters. The shelf break fronts were most pronounced at Tatchu Point, just south of Brooks Peninsula; to the south of Tatchu Point, only the shoreward shelf break front

was consistently observed. The cross-shore scale of the shelf-break front at Tatchu Point was about 20 km, which is roughly equal to the internal Rossby radius of deformation, but moving to the south, the cross-shore scale of the shelf-break fronts increased, and the offshore shelf-break front appeared to merge with the offshore front. The merging of the fronts to the south was probably due to the increasing width of the continental shelf and the decreasing gradient of the shelf slope, so that the cross-shore scales were modified by the topography. The persistence of the inshore shelf-break front may be due to the shallow shelf-waters that show greater variability due to solar heating. In addition, the inshore shelf-break front may be related to the cross-shore shear between the equatorward flowing shelf break current and the poleward flowing Vancouver Island Coastal Current. The offshore front roughly coincided with the 2000 m bathymetry contour, and presumably represented the offshore extent of the seasonal shelf break current; whereas, the shelf-break fronts represent the surface signature of the cold-core of the shelf break current that intensified during the upwelling event.

Comparison of hydrographic data to AVHRR imagery showed a good qualitative agreement. Upper layer cross-shore temperature contours at Estevan Point calculated from CTD casts were similar to structure to the SST imagery: warmer water over the shelf and offshore regions, and isotherms that dome upward over the shelf break with minimum temperature just seaward of the shelf break. Similarly, continuous measurements of the temperature taken from subsurface moorings at depths of 5 m and 30 m were also consistent with the AVHRR SST structure. The longshore surface velocity was estimated using an AVHRR feature tracking technique and a simple time-independent barotropic model that was governed by the conservation of potential vorticity. The feature tracking and the barotropic model velocities agreed within an order of magnitude to velocity measurements recorded by a subsurface current mooring; both velocity estimates were larger in magnitude than the current meter results, but the current meter measurements and

the velocity estimates indicated a velocity increase as the upwelling favourable winds increased in strength. However, the AVHRR-derived velocities on July 18 (day 200) were essentially the same as velocities measured by the E2 current mooring on the same date; the good agreement was related to the decay of upwelling along the shelf break as the coastal upwelling approached a quasi-steady state. Overall, the *in situ* observations agreed favourable with the AVHRR thermal imagery.

6.2 Conclusion

At the beginning of this thesis, five major objectives were outlined, and for the most part, these objectives have been answered. The first objective was concerned with the spatial and temporal scales of the upwelling event. The cross-shore spatial scales are dominated by the presence of thermal fronts on the inshore and offshore side of the shelf break, and a front in the offshore waters. The shelf break front cross-shore scales are typically 20 km, which is consistent with the internal Rossby radius of deformation. The offshore front cross-shore scale is around 70 km and probably represents the offshore extent of the shelf break current. In the long-shore direction, the spatial scales presumably depend on the strength and duration of the winds. The temporal scale of the upwelling event was order 10 days and is probably tied to the length of time that a high-pressure atmospheric system, strong enough to cause an upwelling event, would sustain itself.

The second objective dealt with the relationship between the satellite-sensed thermal structure and dynamical processes within the ocean. Under the right conditions, when an ocean-interior dynamical process manifests itself as a surface thermal feature, vis-a-vis the upwelling event, then AVHRR observations are representative of interior processes;

however, intense solar heating, combined with low winds can presumably mask interior processes. In addition, the temporal and spatial scales of an upwelling event are readily observed using AVHRR imagery; whereas, smaller-scale dynamical processes are not as amenable to AVHRR observations due to the spatial resolution of the satellite imagery, and depending on the period of the dynamical process, satellite observations may be limited by orbital constraints.

The issue of shelf break upwelling versus advection was the subject of the third objective. It was not clear which of these two processes were dominant in producing the band of cold water that persisted along the shelf break, but the cross-shore spatial scales measured from the AVHRR imagery, the longshore averaged SST structure, the cross-shore temperature structure at Estevan Point, and the variability of the AVHRR-derived surface velocities all indicate that shelf break upwelling is probably occurring; however, since the cross-shore scales that characterize the shelf break upwelling and the shelf break jet are essentially the same, it may be difficult to separate both processes. Other studies have shown that the effect of a blunt headland jutting into the mean flow (Brooks Peninsula), and the effects of longshore and cross-shore variations in the topography may also enhance the upwelling process, and thus account for some of the observed SST structure. The dynamical process that forces the cold water to remain centered along the shelf break as the water migrates equatorward from Brooks Peninsula was the main issue of the fourth objective. The dynamics can be partly explained in terms of the conservation of potential vorticity that is tied to the variation of the cross-shore topography at the shelf break, but upwelling is a complicated event, and there is no doubt that other dynamical processes are playing a role.

The uniqueness of the upwelling event was addressed by the fifth objective, and it appears that the July, 1984 upwelling event is indicative of the spatial and temporal

variation of the SST that can occur during the summer months; qualitative investigations of AVHRR imagery from other summers confirms the similarity to the 1984 observations, but interannual variability frequently occurs that is typified by the formation of eddies, and in the offshore migration of plumes of cold, upwelled water. The interannual variability presumably has a significant effect on the transport of nutrients into the La Perouse Bank fishing grounds. As was the case during July, 1984, the equatorward extent of the upwelled water was significant (see Figure 5.12a), and there was probably a considerable transport of nutrients in the long-shore direction; however, at other times, offshore plumes form, and the nutrients that are transported to the surface during the upwelling process are advected offshore (see Figure 1.2b) and do not reach the region in the vicinity of La Perouse Bank. One of the unanswered questions from this study dealt with the issue of shelf-break upwelling versus long-shore advection, and the resolution of this question may yield some estimate as to whether or not nutrients are upwelled at specific locations along Vancouver Island and transported by long-shore advection, or if nutrients are upwelled continuously along the shelf break.

The results of this study may also act as a starting point to develop a comprehensive picture of the interannual variability of the shelf break current. A reasonably long time series of AVHRR data are difficult to obtain, but a time series of coastal wind data and Bakun Upwelling Index data are readily available. By the combining the temporal and spatial scales obtained from the July, 1984 AVHRR data set with wind data from other years, it may be possible to interpolate the SST structure when satellite imagery is not available.

CHAPTER 7

BIBLIOGRAPHY

- Abbot, M.R., and D. B. Chelton, Advances in passive remote sensing of the ocean, in U.S. National Report 1987-90, International Union of Geodesy and Geophysics, American Geophysical Union, 571-587, 1991.
- Allen, J.S., Upwelling and coastal jets in a stratified ocean, *J. of Phys. Oceanography*, 3, 245-257, 1973.
- Allen, J.S., Models of wind-driven currents on continental shelves, *Annu. Rev. Fluid Mech.*, 12, 389-433, 1980.
- Apel, J.R., Principles of Ocean Physics, Academic Press, London, 634 pp., 1987.
- Bakun, A., Daily and weekly upwelling indices, west coast of North America, 1946-71, NOAA Tech. Rep. 16, NMFS-SSRF-671, 96 pp., U.S. Dept. of Commerce, 1973.
- Bang N.D. and W.R.H. Andrews, Direct current measurements of a shelf-edge frontal jet in the southern Benguela system, *J. Mar. Res.*, 32, 407-419, 1974.
- Barton, E.D., A. Huyer, and R.L. Smith, Temporal variation observed in the hydrographic regime near Cape Coveiro in the northwest African upwelling region, February to April 1974, *Deep Sea Res.*, 24, 7-23, 1977.
- Bowden, K.H., Summing-up, *Philos. Trans. R. Soc. London*, Ser A, 302, 683-689, 1981.
- Charney, J.G., The generation of ocean currents by wind, *J. Mar. Res.*, 14, 477-498, 1955.

- Crepon, M., C. Richez, and M. Chartier, Effects of coastline geometry on upwelling, *J. Phys. Oceanography*, 14, 1365-1382, 1984.
- Csanady, G.T., Circulation in the Coastal Ocean, Reidel, Holland, 278 pp., 1982.
- Dickson, R.R., P.A. Gurbutt, and V.N. Pillai, Satellite evidence of enhanced upwelling along the European continental slope, *J. Phys. Oceanography*, 10, 823-819, 1980.
- Denman, K., R. Forbes, A. Gargett, D. Mackas, R. Thomson, and S. Calvert, Processes controlling vertical and horizontal exchanges of carbon along the Canadian Pacific continental margin, JGOFS News, in *Canadian Met. Ocy. Society Annual Review* 1992, 26 pp., 1992.
- Dodimead, A.J., F. Favorite, and T. Hirano, Salmon of the North Pacific Ocean-Part II: Review of the oceanography of the subarctic Pacific region, Int. North Pac. Fish. Comm., Bull. 13, 195 pp., 1963.
- Emery, W.J., M. Ikeda, A comparison of geometric correction methods for AVHRR imagery, *Canadian J. of Remote Sensing*, 10, 46-56, 1984.
- Emery, W.J., W.G. Lee, and L.Magaard, Geographic and seasonal distributions of Brunt-Vaisala frequency and Rossby radii in the North Pacific and North Atlantic, *J. Phys. Oceanography*, 14,294-317, 1984.
- Emery, W.J., A. Thomas, M. Collins, W. Crawford, and D. Mackas, An objective method for computing advective surface velocities from sequential infrared satellite images, *J. Geophysical Res.*, 91, 12,865-12,878, 1986.
- Emery, W.J., J. Brown, and Z. Nowak, AVHRR image navigation: Summary and review, *Photogrammetric Eng. Remote Sensing*, 55, 1175-1183, 1989.
- Emery, W.J., P. Schluessel, Global differences between skin and bulk sea surface temperatures, *Eos*, 70(14), 211-213, 1989.

- Favorite, F., A.J. Dodimead, and K. Nasu, Oceanography of the subarctic Pacific region, 1960-72, Int. North Pacific Salmon Comm., Bull 33, 187 pp., 1976.
- Fang, W., W.W. Hsieh, Summer upwelling off Vancouver Island from satellite SST data, submitted to *J. Geophysical Res. (Oceans)*, July 1992.
- Freeland, H.J., K.L. Denman, A topographically controlled upwelling centre off southern Vancouver Island, *J. Mar. Res.*, 40, 1069-1093, 1982.
- Freeland, H.J., W.R. Crawford, and R.E. Thomson, Currents along the Pacific coast of Canada, *Atmosphere-Ocean*, 22, 151-172, 1984.
- Freeland, H.J., The flow of a coastal current past a blunt headland, *Atmosphere-Ocean*, 28, 288-302, 1990.
- Gill, A.E., Atmosphere-Ocean Dynamics, Academic Press, London, 662 pp., 1982.
- Griffin, D.A., P.H. LeBlond, Estuary/ocean exchange controlled by spring-neap tidal mixing, *Estuarine, Coastal, and Shelf Science*, 30, 275-297, 1990.
- Hickey, B.M., R.E. Thomson, H. Yin, and P.H. LeBlond, Velocity and temperature fluctuations in a buoyancy-driven current off Vancouver island, *J. Geophysical Res.*, 96, 10,507-10,538, 1991.
- Hill, R.B., J.A. Johnson, A theory of upwelling over the shelf break, *J. Phys. Oceanography*, 4, 12-24, 1974.
- Holland, J.A., X.H. Yan, Ocean thermal feature recognition, discrimination, and tracking using infrared satellite imagery, *IEEE Trans. Geosci. Rem. Sensing*, 30, 1046-1053, 1992.

- Huyer, A., Coastal upwelling in the California current system, *Prog. Oceanography*, 12, 259-284, 1983.
- Ikeda, M., L.A. Mysak, and W.J. Emery, Seasonal variability in meanders of the California current system off Vancouver Island, *J. Geophysical Res.*, 89, 3487-3505, 1984.
- Ikeda, M., L.A. Mysak, and W.J. Emery, Observation and modeling of satellite-sensed meanders and eddies off Vancouver Island, *J. Phys. Oceanography*, 14, 3-21, 1984a.
- Ikeda, M., W.J. Emery, A continental shelf upwelling event off Vancouver Island as revealed by satellite infrared imagery, *J. Mar. Res.*, 42, 303-317, 1984.
- Janowitz, G.S., L.J. Pietrafesa, The effects of alongshore variation in bottom topography on a boundary current (topographically induced upwelling), *Cont. Shelf Res.*, 1, 123-141, 1982.
- Jardine, I., Upwelling off Vancouver Island, M.Sc. Thesis, University of British Columbia, 87 pp., 1991.
- Johnson, A.J., A.J. Nurser, A model of secondary upwelling over the shelf break. II, *Geophys. Astrophys. Fluid Dynamics*, 28, 161-170, 1984.
- Jensen, J.R., Introductory Digital Image Processing-A Remote Sensing Perspective, Prentice Hall, New Jersey, 385 pp., 1986.
- Kaufman, Y.J., B.N. Holben, Calibration of the AVHRR visible and near-IR bands by atmospheric scattering, ocean glint, and desert reflection, *Inter. J. of Rem. Sensing*, 14(1), 21-52, 1993.
- Kelley, K.A., P.T. Strub, Comparison of velocity estimates from advanced very high resolution radiometer in the coastal transition zone, *J. Geophysical Res.*, 97, 9653-9668, 1992.

- Kundu, P.K., Fluid Mechanics, Academic Press, San Diego, 638 pp., 1990.
- Legeckis, R., A survey of worldwide sea surface temperature fronts detected by environmental satellites, *J. Geophysical Res.*, 83, 4501-4522, 1978.
- LeBlond, P.H., L.A. Mysak, Waves In the Ocean, Elsevier, Amsterdam, 602 pp., 1977.
- LeBlond, P.H., B.M. Hickey, and R.E. Thomson, Runoff driven coastal flow off British Columbia, In S. Skrerslet (ed.) The role of freshwater outflow in coastal marine ecosystems, NATO ASI Series, G7, 309-317, 1986.
- Mackas, D.L., L. Washburn, and S.L. Smith, Zooplankton community patterns associated with a California current cold filament, *J. Geophysical Res.*, 96, 14,781-14,797, 1991.
- Mason, J.E., A. Bakun, Upwelling index update, U.S. west coast, 33N-48N latitude, NOAA-TM-NMFS-SWFC-67, U.S. Comm. Dept., 21 pp., 1986.
- Mooers, C.N.K., C.A. Collins, and R.L. Smith, The dynamic structure of the frontal zone in the coastal upwelling region off Oregon, *J. Phys. Oceanography*, 6, 3-21, 1976.
- Ninnis, R.M, W.J. Emery, and M.J. Collins, Automated extraction of pack ice motion from advanced very high resolution radiometer imagery, *J. Geophysical Res.*, 91, C9, 10,725-10,734, 1986.
- O'Brien, J.J., H.E. Hurlburt, A numerical model of coastal upwelling, *J. Phys. Oceanography*, 2, 14-26, 1972.
- Pedlosky, J., On coastal jets and upwelling in a bounded basin, *J. Phys. Oceanography*, 4, 3-18, 1974.

- Pedlosky, J., Geophysical Fluid Dynamics, Springer-Verlag, New York, 710 pp., 1987.
- Petrie, B.D., Current response at the shelf break to transient wind forcing, *J. Geophysical Res.*, 88, 9567-9578, 1983.
- Peffley, M.B., J.J. O'Brien, A three-dimensional simulation of coastal upwelling off Oregon, *J. Phys. Oceanography*, 6, 164-179, 1976.
- Pond, S., G. Pickard, Introductory Dynamical Oceanography, Pergamon Press, Oxford, 319 pp., 1983.
- Pratt, W.K., Digital Image Processing, 2 ed., John Wiley & Sons, New York, 578 pp., 1991.
- Ramp, S.R., P. Jessen, K. Brink, P. Niiler, F. Daggett, and J. Best, The physical structure of cold filaments near Point Arena, California, during June 1987, *J. Geophysical Res.*, 96, 14,859-14,883, 1991.
- Robinson, I.S., Satellite Oceanography: An introduction for oceanographers and remote-sensing scientists, Ellis Horwood, England, 455 pp., 1985.
- Ryther, J.H., Photosynthesis and fish production in the sea, Science, 166, 72-76, 1969.
- Saunders, R.W., and D.P. Edwards, Atmospheric transmittances for the AVHRR channels, *Applied Optics*, 28, 19, 4154-4160, 1989.
- Schlüssel, P., W. Emery, H. Grassl, and T. Mammen, On the bulk-skin difference and its impact on satellite remote sensing of sea surface temperature, *J. Geophysical Res.*, 95, 13,341-13,356, 1990.
- Siebold, E., W.H. Berger, The Sea Floor: An Introduction to Marine Geology, Springer-Verlag, New York, 1982.

Simpson, J.J., On the accurate detection and enhancement of oceanic features observed in satellite data, *Remote Sensing Environment*, 33, 17-33, 1990.

Smith, S.D., Wind stress and heat flux over the ocean in gale force winds, *J. Phys. Oceanography*, 10, 709-726, 1980.

Smith, R.L., A comparison of the structure and variability of the flow fields in three coastal upwelling regions: Oregon, Northwest Africa, and Peru, in Coastal Upwelling, Coastal Estuarine Science Series, vol. 1, edited by F.A. Richards, 107-118, AGU, Washington, D.C., 1981.

Stewart, R.H., Methods of Satellite Oceanography, University of California Press, Berkeley, 360 pp., 1985.

Tabata, S., On the accuracy of satellite-observed sea surface temperatures, in Oceanography From Space, edited by J.F.R. Gower, 145-157, Plenum Publishing, New York, 1981.

Thomas, A.C., Relationships between near-surface plankton distributions, hydrography, and satellite measured sea surface thermal patterns, Ph.D. Thesis, University of British Columbia, 147 pp., 1987.

Thomson, R.E., Oceanography of the British Columbia Coast, Can. Spec. Publ. Fish. Aquat. Sci., 291 pp., 1981.

Thomson, R.E., A comparison between computed and measured oceanic winds near the British Columbia coast, *J. Geophysical Res.*, 88, 2675-2683, 1983.

Thomson, R.E., A cyclonic eddy over the continental margin of Vancouver Island, *J. Geophysical Res.*, 88, 2675-2683, 1984.

Thomson, R.E., J.F.R. Gower, A wind-induced mesoscale eddy over the Vancouver Island continental slope, *J. Geophysical Res.*, 90, 8981-8993, 1986.

- Thomson, R.E., B.M. Hickey, and P.H. LeBlond, Water property observations from the Vancouver Island Coastal Current experiment: June, July, and October, 1984, Can. Data Rep. Hydrogr. Ocean Sci., 46, 505 pp., 1986.
- Thomson, R.E., W.R. Crawford, H.J. Freeland, and W.S. Hugget, Low-pass filtered current meter records for the west coast of Vancouver Island: Coastal Ocean Dynamics Experiment, 1979-81. Can. Data Rep. Hydrogr. Ocean Sci. 40: 102 pp., 1986a.
- Thomson, R.E., B.M. Hickey, and P.H. LeBlond, The Vancouver Island coastal current: Fisheries barrier and conduit, in Effects of Ocean Variability on Recruitment and an Evaluation of Parameters Used in Stock Assessment Models, edited by R.J. Beamish and G.A. McFarlane, Can. Spec. Publ. Fish. Aquat. Sci., 108, 265-296, 1990.
- Walton, C.C., E.P. McClain, and J.F. Sapper, Recent changes in satellite-based multi-channel sea surface temperature algorithms, MTS '90, Marine Technology Society Meeting, Washington, D.C., 7 pp. September 1990
- Wang, D.C., A.H. Vagnucci, and C.C. Lin, Digital Image Enhancement: A Survey, *Computer Vision, Graphics, and Image Processing*, 24, 363-381, 1983.
- Ware, D., R.E. Thomson, La Perouse project: First annual report, 1985, Dep. Fish. Oceans Canada, 25 pp., 1986.
- Ware, D., R.E. Thomson, La Perouse project: Third annual report, 1987, Dep. Fish. Oceans Canada, 64 pp., 1988.
- Wick, G., W.J. Emery, A comprehensive comparison between satellite-measured skin and multichannel sea surface temperature, *J. Geophysical Res.*, 97, 5569-5595, 1992.